OPTICAL PROPERTIES OF IMPURITY IONS IN FLUORIDE MATERIALS

By

MICHAEL DAVID SHINN

Bachelor of Science
Oklahoma State University
Stillwater, Oklahoma
1978

Master of Science
Oklahoma State University
Stillwater, Oklahoma
1980

Submitted to the Faculty of the
Graduate College of the
Oklahoma State University
in partial fulfillment of
the requirements for
the Degree of
DOCTOR OF PHILOSOPHY
December, 1983

OPTICAL PROPERTIES OF IMPURITY

IONS IN FLUORIDE MATERIALS

Thesis Approved:

W. A. Sibley
Thesis Adviser

Larry E. Halliburton

E. E. Kohnke

J. Paul Devlin

Richard C. Powell

Norman N. Durham
Dean of the Graduate College

ACKNOWLEDGMENTS

This dissertation is the result of a very fruitful period of study under Bill Sibley's guidance. To him go my special thanks, for being both a good friend and facilitator. I would also like to thank the other members on my committee, Paul Devlin, Larry Halliburton, Elton Kohnke, and Dick Powell, for their assistance. Financial support, in the form of a Research Assistantship through the Radiation Safety Program, and the National Science Foundation, is greatly appreciated.

During my studies at Oklahoma State I have made many friends whose companionship has been most rewarding. In particular, I would like to thank Robert Love for his encouragement that I attend graduate school.

My special thanks to my family for their years of love and support. For my dear wife, Helen-Mary, I reserve my deepest appreciation, for her love and encouragement that I do well, even when it meant more nights at "the lab". I dedicate this dissertation to her.

TABLE OF CONTENTS

LIST OF TABLES

LIST OF FIGURES

Figure Page

CHAPTER I

INTRODUCTION

The optical properties of solids, that is, the study of the interaction of light with matter, has been the subject of many investigations in condensed matter physics. In particular, the study of the optical properties of impurity ions in otherwise pure solids has been rewarding, both for the new physics it has required to explain the observed phenomena, and for the technological benefits reaped by taking advantage of these properties. For example, ruby, which is Cr^{3+} in Al_2O_3, was used as the lasing medium in the first laser.

Phosphors, used for fluorescent lamps and television screens, are also based on impurity-doped materials. With the advent of ultra low-loss optical fibers, and solid state light sources and detectors, our society will continue to advance technologically through the exploitation of the optical properties of these and other materials.

Of the many interesting materials available for study those with fluorine anions have some useful properties in common:

1) Their melting points are generally less than oxide materials, making them less costly to grow.

2) The resulting materials can be grown to a high degree of purity.

3) The range of high transparency extends from the uv (<250 nm) to the far infrared (>5000 nm), a greater range than is accessable for most oxide materials.

4) The nonlinear refractive indices and damage thresholds are higher for fluoride materials in general, which is advantageous if the material is to be used as a laser medium.

5) The phonon energies of fluoride hosts are lower, in general, than are found in oxide materials. It will be shown later that the lower the phonon energy, the less effective nonradiative processes are in quenching fluorescence. This is usually advantageous in optical devices. With these properties it is understandable that fluoride materials are being seriously considered as hosts for high-power solid state lasers (1).

This brings us to the purpose of this study: to investigate the optical properties of impurities in two fluoride hosts; crystalline $RbMgF_3$ and fluorozirconate glass. The impurities are Er^{3+}, Eu^{2+}, and Mn^{2+} in $RbMgF_3$, and Er^{3+} in the fluoride glass.

Crystals of $RbMgF_3$ do not occur naturally. It was first synthesized by Remy and Seeman in 1940 (2), and reported independently by Dergunov and Bergman in 1948 (3). The crystal structure was first reported as being monoclinic (4), and later confirmed that it deviated from cubic (5). Shafer and McGuire (6) reported that $RbMgF_3$ had the hexagonal barium titanate structure through the compositional range $0<x<0.68$ of $RbMg_{1-x}\ Co_xF_3$. The lattice constants were reported as being $a_o=5.83\text{Å}$ and $C_o=14.27\text{Å}$. It has been determined through x-ray crystallography that our crystals are hexagonal $BaTiO_3$ in structure with lattice constants of $a_o=5.84\text{Å}$ and $C_o=14.24\text{Å}$ (7).

Figure 1 illustrates the crystal structure of $RbMgF_3$. The structure is further elucidated by Fig. 2, a photograph of a model $RbMgF_3$ lattice. It can be seen that all Mg^{2+} ions have six F^- nearest neighbor ions, with C_{3v} symmetry. One third of the Mg^{2+} ions are in sites with equidistant ligands. These sites are labelled "site 1". The other two thirds of the Mg^{2+} ions are in sites with nonequidistant ligands. They are labelled "site 2". The Rb^+ ion sites, which are 12-fold coordinated, have C_{3v} and D_{3h} site symmetries and are analogous to the Mg sites. Thus the $RbMgF_3$ lattice can be a host lattice to many impurities which may substitute for the monovalent or divalent cations.

It was mentioned earlier that $RbMgF_3$ was initially used to "dilute" $RbCoF_3$. Almost all of the work on $RbMgF_3$

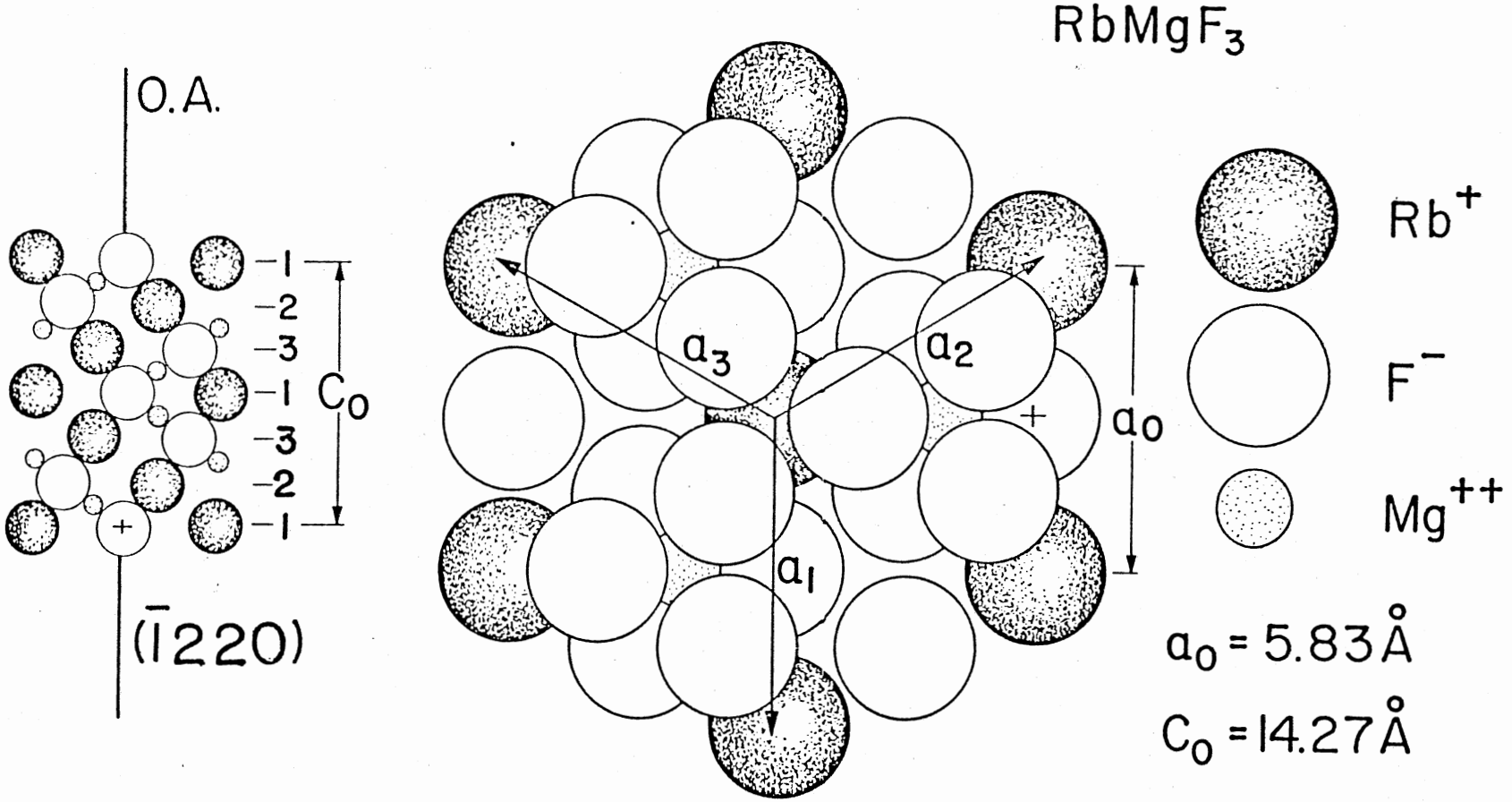

Figure 1. $RbMgF_3$ Model. Shown are the Basal Plane and the Close-Packed Sequence of Ions Along the Optic Axis Which Lie in the $(\bar{1}220)$ Plane. (Taken from Ref. 8)

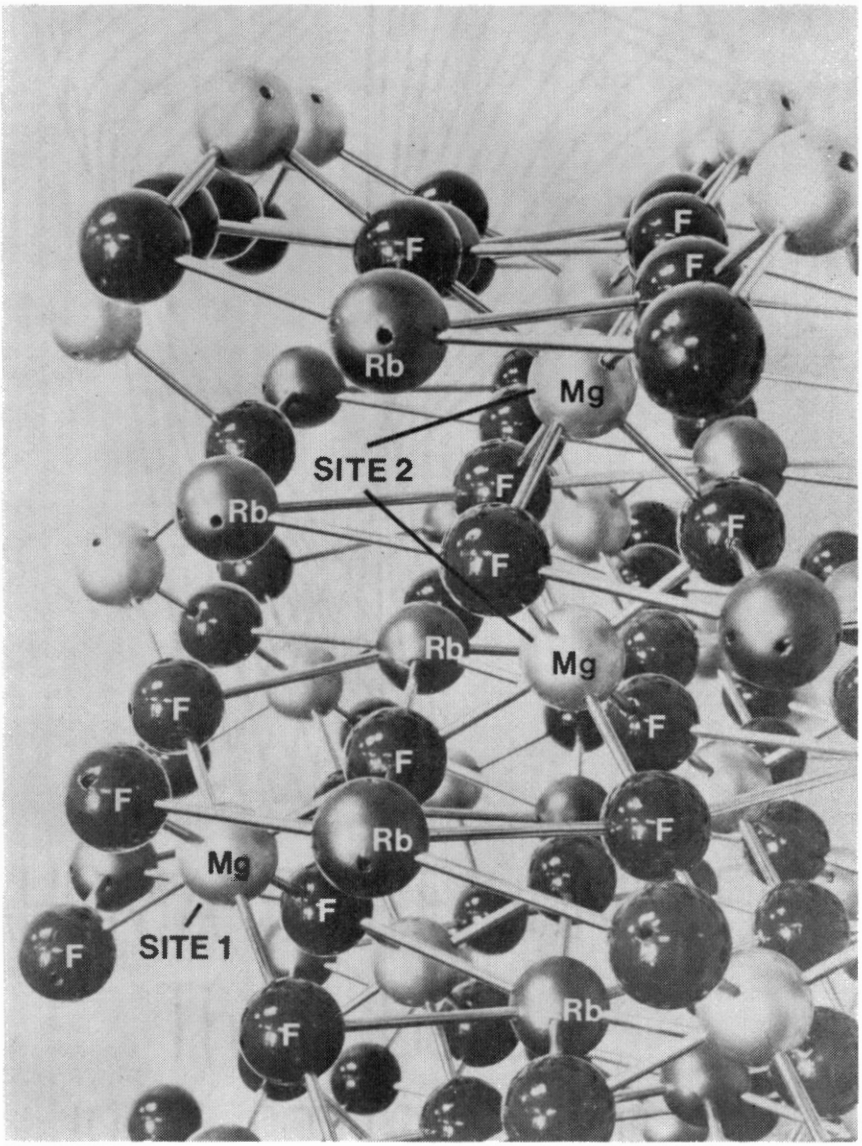

Figure 2. Model of $RbMgF_3$ Lattice. Labeled "site 1" and "site 2" are the two Mn^{2+} sites in $RbMgF_3$

has been conducted by W.A. Sibley and co-workers at Oklahoma State University (8-17). The initial studies identified the radiation-induced-defects in $RbMgF_3$, and showed that in contrast to most materials, the defects created during room temperature irradiation were immobile (8-12). Concurrent with this work was an investigation on the optical properties of unirradiated and irradiated $RbMg_{1-x}Mn_xF_3$ (9-11). The next phase in this research effort is the first subject of this study: to investigate the optical properties of rare earth ions in $RbMgF_3$ (13). The optical properties of $RbMgF_3$ double-doped with rare earth ions and Mn^{2+} ions are also studied (13,17).

Prior to 1975, most known glasses were based on the oxides of compounds. In that year, M. Poulain, under the supervision of J. Lucas at Rennes, France attempted to grow crystals of $ZrBaNaF_7$. To their suprise, and initial disappointment, they found that a glass had been formed instead (18). Fortunately, they realized that this was an entirely new type of glass, based on heavy-metal fluorides, and began to study the compositional regimes of glass formation as well as new compositions of glass (19,20). This was followed by investigations on the properties of the two most common types of fluoride glass; the fluorohafnates and fluorozirconates, based primarily on HfF_4 and ZrF_4, respectively. The compositions and properties of some heavy-metal fluoride glasses are shown in Table 1. The glasses have been shown to have a wide range of transpar-

TABLE I

COMPOSITIONS AND PROPERTIES OF SOME HEAVY METAL FLUORIDE GLASSES (COMPOSITION IN MOL%)

GLASS	ZrF_4	HfF_4	BaF_2	LaF_3	ThF_4	AlF_3	ErF_3	T_g (°C)	T_x (°C)	DENSITY (g/cm^3)
ZBT*	58		33		9			315	394	4.86
ZBL**	60		35	5						
HBT*		58	33		9			319	396	6.19
HBL*		58	33	9				332	415	5.56
ZBLA:Er	57		35.5	3		4	0.5	310	390	4.61
ZBLA:Er	57		34	3		4	2	310	390	4.61

Source: * Ref. 21 ** Ref. 103

ency, extending from 300 nm to about 7000 nm, much further into the IR than conventional oxide glasses. This leads to the possibility that they may be used for very long repeaterless (>50 km) optical fibers (21). Their resistance to moisture and acids is also very good.

Only recently have the possibilities of using these glasses as laser hosts been explored. These glasses will easily accept up to 5 mol.% trivalent rare earth ions. The first study was on Nd^{3+} in ZBL glass (The convention is to label the glass by the first letters of the cations - see Table 1.) (22). It was found that the Nd^{3+} ion substituted only for the Zr^{4+} or La^{3+} ion and was thus surrounded by a polyhedron (coordination numbers are believed to range from 6 to 8) of fluorine ions. Due to this structure and the ionic nature of the bonding, the rare earth ion is in a site symmetry whose local environment is almost invariant. This causes the inhomogeneous linewidths of the absorptions and emissions to be narrower than seen in oxide glasses. The decay of the luminescence was almost single exponential, also indicating that the site-to-site variation of the Nd^{3+} ions was small. It was found that the nonlinear refractive index of this glass was as low as the best fluorophosphate glasses (1) and the stimulated emission cross-sections were comparable to the best silicate glasses, leading the authors to conclude that this material was a good candidate for a laser host (22).

Subsequent measurements on the optical properties of

Eu^{3+} in ZBLA glass (23) and Er^{3+} in PZGL glass (24) also showed that the bandwidths of the absorption and emission lines were all narrower than observed in oxide glasses. More emission lines, corresponding to transitions from higher-lying states to lower excited states were observed for the Eu^{3+}-doped glass, implying reduced nonradiative rates in this host (23). This low nonradiative rate was addressed in a following study (24) and ascribed as being due to the low phonon energies in fluoride glasses. However, to date, no systematic determination of the nonradiative rates in the fluoride glasses have been made. For example, all the lifetime and most of the emission measurements have been made at room temperature.

This is the second subject of this study: to report on a recent investigation of the optical properties of Er^{3+} in ZBLA glass (25). Extensive absorption- ,emission-, and excitation-spectra measurements, as well as lifetime data taken in the temperature range 6-520K are presented. Through these measurements, determination of the radiative and nonradiative rates will be made.

CHAPTER II

THEORY

Energy Levels of Impurity Ions in Crystals

The ability to calculate the energy levels of an ion, either in free space, or when incorporated into a host, is one of the great achievements of quantum mechanics. Shortly after the establishment of modern quantum mechanics by Schrodinger and others, Slater published his work on the application of quantum mechanics to complex spectra (26). This has been expanded considerably, and excellently described by Condon and Shortly (27) and Slater (28). Parallel to the development of the calculation of the energy levels of the free ion is the development of crystal field or ligand field theory, which describes the effect of neighboring ions on the energy levels of a particular ion. This was developed by Bethe (29), Van Vleck (30,31), and Schlapp and Penney (32,33). A detailed discussion of these topics is beyond the scope of this study; for more information the references cited above and other, excellent reviews are available (34-36). A summary of some of the relevant aspects of the above topics is essential however in understanding the effects

of the host medium on the optical properties of a particular ion.

In the formalism of quantum mechanics the calculation of the energy levels of an ion in a solid (assumed for now to be crystalline) is an eigenvalue problem. To solve this problem, the eigenstates of the ion and the Hamiltonian must be determined. The Hamiltonian may be broken into two parts

$$H = H_{\text{free-ion}} + H_{\text{crystal-field}} \tag{1}$$

or

$$H = \frac{-\hbar^2}{2m} \sum_i \nabla_i^2 - \sum_i \frac{Ze^2}{r_i} + \frac{1}{2} \sum_{i \neq j} \frac{e^2}{r_{ij}} + \sum_i \xi_i (\vec{l}_i \cdot \vec{s}_i) + H_{cf} \tag{2}$$

where the summations are over all the optically active electrons. The first two terms represent the kinetic and potential energies of the individual electrons, while the third term is the electrostatic repulsion between pairs of electrons. The fourth term is due to spin-orbit coupling, and the last term is due to the crystal field. The crystal field is treated approximately as an electrostatic field at the ion site due to the charges of the nearest neighbors.

The advantage of a Hamiltonian in the form of Eq.(2) is that only one- and two-electron integrals must be solved to calculate the eigenvalues. The choice of

eigenstates is where the problem, by necessity, becomes more approximate. The wavefunctions are usually assumed to be hydrogenic in form (27,28,37-39). Even though the wavefunctions have been shown to deviate from hydrogenic, this approximation has been shown to work quite well, with appropriate modifying corrective terms, to accurately indicate level assignments and give reasonably correct values for the energy levels.

We now consider two cases for solving Eq.(2). In the weak field case, H_{cf} is much less in magnitude compared to the first four terms in Eq.(2) and is treated as a perturbation. In the strong field case H_{cf} is comparable to the third term in Eq.(2). Good examples of the weak field scheme are the trivalent rare earth ions. Such ions have completely filled inner orbitals in the xenon configuration, incompletely filled 4f orbitals and filled 5s and 5p states. These latter states for the most part are at a greater distance from the nucleus than the 4f states, providing shielding from the effects of the host (35). As a result the energy levels of the 4f states are approximately the same as the free-ion energy levels, no matter what the host medium, precisely the condition required for the weak field scheme.

Starting with the free-ion terms of Eq.(2) we consider the effects of each term on a rare earth ion. The first two terms describe the interaction of each optically active electron with the ion core. This yields the 4f

atomic electron orbitals which form the $4f^N$ electron configuration. The Coulomb repulsion term splits this configuration into states with different energies which are characterized by values of $\vec{L}$ and $\vec{S}$, the total orbital and spin angular momenta, respectively. It is possible that different states may have the same $\vec{L}$ and $\vec{S}$ values, so an additional label α is used. The Coulomb repulsion term can also mix states of different energy, but the same L,S values. The spin-orbit term can commute with the total angular momentum $\vec{J}$ so the eigenstates are labelled by J,M_J. In the Russell-Saunders approximation, mixing of different LS terms is assumed to be negligible and the eigenstates are labelled $^{2S+1}L_J$. These states are called J-multiplets and are 2J+1 degenerate. The separation between them should be in terms of the Lande' interval rule

$$E_J - E_{J-1} = \lambda J \qquad (3)$$

where λ is approximately proportional to $(Z)^{1/4}$. In reality the Russell-Saunders approximation breaks down for the rare earths. This is partly due to the magnitudes of the Coulomb term, which places the various LS terms close enough in energy that the spin-orbit term can mix states of the same $\vec{J}$ from different αLS terms. Thus $\vec{L}$ and $\vec{S}$ cease to be good quantum numbers. The states are thus considered to be intermediately-coupled. They are still labelled

$^{2J+1}L_J$, although in many cases only the ground state can be considered a nearly pure Russell-Saunders state.

The effect of the crystal field is to remove the degeneracy of the various states. The crystal field for a site can be expressed in terms of spherical harmonics (35,40)

$$H_{cf} = \sum_{kq} B^k_q \sum_i (C_i)^k_q \qquad (4)$$

where the C^k_q are tensor operators normalized like associated Legendre functions and the B^k_q are parameters composed of integrals of the radial wavefunctions and normalization of the spherical harmonics. The number of parameters needed to characterize the crystal field may be obtained from group theory. Because the radial wavefunctions are not at present calculable from first principles, the values of these parameters are determined by comparing calculated and observed splittings of the J-multiplets.

The transition metal ions are examples of the strong field scheme. Here the 3d electrons are optically active. These wavefunctions are more extended than the 4f electron wavefunctions, and are unshielded, making them more sensitive to the effects of their environment. Thus the crystal field term in Eq.(2) is comparable to the interelectron repulsion term, while the spin-orbit term may be considered to be a perturbation. Considering our Hamiltonian (Eq.(2)) again, the first two terms establish

the $3d^N$ configuration, made up of independent one-electron 3d states. We now consider the effect of H_{cf} on this configuration. It is customary to consider the ion to be in a site of octahedral or tetragonal symmetry. It can be shown (32,34,41) that the crystal field splits the d orbitals, which are five-fold degenerate (since l=2) into a two-fold degenerate state (labelled e_g) and a three-fold degenerate state (labelled t_{2g}). The energy separation between the e_g and t_{2g} states is denoted 10Dq, where Dq is a measure of the strength of the crystal field (34,41).

With these states to work with, one can now add the effect of the interelectron repulsion term. This is characterized by the three Racah parameters A,B, and C (42). This creates new eigenstates labelled by the values of S and Γ, where Γ is the group theoretical symbol indicating the irreducible representation of the group to which the eigenstate belongs.

Finally the spin-orbit interaction must be accounted for. Since this term is small compared to the others, it is treated through perturbation theory. Its effect is to break the $S\Gamma$ terms into multiplets, similar to the J-multiplets of the rare earth ions.

The energy separation between the $S\Gamma$-multiplets is dependent on the values of Dq and B. Following Tanabe and Sugano (42), this separation (in units of B) is plotted as a function of crystal field strength (in units of Dq/B).

An example of such a plot, referred to as a Tanabe-Sugano diagram, is shown in Fig. 3 for Mn^{2+} for $B=960cm^{-1}$. On the left side of the figure the levels are labelled assuming octahedral symmetry.

Absorption and Emission of Light by Impurity Ions

We now consider the interaction of photons with ions embedded in an optically inert host medium. This interaction is treated quantum mechanically by utilizing time-dependent perturbation theory (43,44). The probability per unit time that a transition occurs between a state i and a state f is given by Fermi's "Golden Rule"

$$P_k(t) = \frac{2\pi}{\hbar} |M_k|^2 g(\omega_k) \tag{5}$$

where

$$M_k = \langle f|H'|i\rangle \tag{6}$$

and $g(\omega_k)$ is the density of final states. H' is the perturbation

$$H' = -\sum_j (e/mc)\vec{A}_j \cdot \vec{p}_j \tag{7}$$

The summation runs over all j optically active electrons, $\vec{A}$ is the vector potential of the photons, and $\vec{p}$ is the

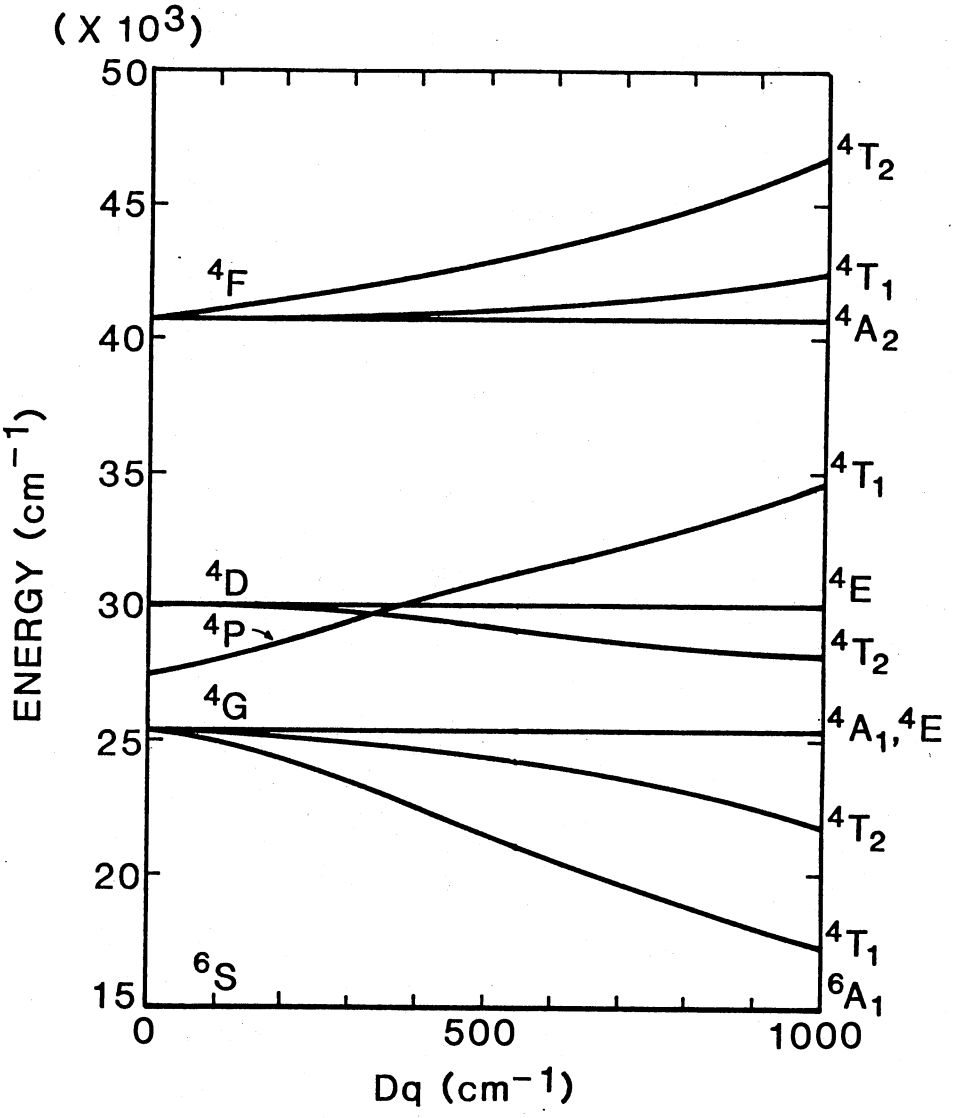

Figure 3. Tanabe-Sugano Diagram for Mn^{2+}

electron's momenta, which have mass m and charge e. This perturbation can be expanded in terms of the electric dipole moment operator $\vec{d} = \sum_j e\vec{r}$ and the magnetic dipole moment operator $\vec{m} = \sum_j (e/2m)(\vec{l}_j + 2\vec{s}_j)$. There is also an electric quadrupole moment operator, plus higher moment operators, but they will be neglected here. Letting $\vec{D}$ represent these operators, the line strength of the transition is defined as

$$S_{if} = \sum_{if} (\langle f|\vec{D}|i\rangle)^2 \qquad (8)$$

where the summation runs over the two manifolds of states i and f. If the frequency of the photons absorbed (or emitted) during the transition is ν then the line strength may be defined in terms of a dimensionless quantity called the oscillator strength, f

$$f(i,f) = \frac{8\pi^2 m\nu\chi}{3he^2 g} S_{if} \qquad (9)$$

where χ is a correction factor for the effective electric field at the ion site, and g is the degeneracy of the level from which the transition originates. For an allowed electric dipole transition $f \simeq 1$, while for an allowed magnetic dipole transition $f \simeq 10^{-6}$. The selection rules for these two types of transitions are

Electric dipole: $L = \pm 1$ $S = 0$ $J = \pm 1, 0$

Magnetic dipole: $L = 0$ $S = 0$ $J = \pm 1, 0$ $0 \not\leftrightarrow 0$

As shown earlier, due to spin-orbit coupling, states of different spin can be admixed and thus the spin selection rule is not as rigorous as the orbital angular momentum rule. Nevertheless, spin-allowed transitions are observed to be stronger than spin-forbidden transitions.

The value of the oscillator strength may be determined experimentally through the relation

$$f(i,f) = \frac{mc}{N\pi e^2}\int \alpha(\nu)d\nu \qquad (10)$$

where N is the concentration of optically active ions and α is the absorption coefficient

$$\alpha(\nu) = \frac{\ln\{I_o(\nu)/I(\nu)\}}{t} \qquad (11)$$

where I_o is the intensity of a beam of light as it enters the sample and I is the intensity as it leaves the sample, having traversed the sample's thickness t. Measurements of the oscillator strengths of the absorptions of an ion in a host medium are useful, as they can be used to calculate other quantities of interest, and because the type of transition, electric- or magnetic-dipole, can be used to determine the identity of the excited state. Group theory can be used to determine if a particular type of transition is allowed or forbidden (34,45).

For transition metal ions it would be expected that radiative transitions between pure $3d^N$ states would occur

only by magnetic dipole processes, since $\Delta L=0$. Experimentally, the oscillator strengths can be much higher than expected (10^{-3} to 10^{-1}). This can be explained by admixing of the higher energy $3d^{N-1}4p$ and $3d^{N-1}4f$ odd-parity configurations into the $3d^N$ configuration, permitting electric dipole transitions to occur. Such an admixing can occur by having the ions in sites lacking inversion symmetry, or through lattice vibrations which temporarily cause deviations in inversion symmetry.

A similar situation occurs for the trivalent rare earth ions. Once again electric dipole transitions should be parity forbidden. However, the oscillator strengths and polarized emission data indicated that the emissions were primarily "forced" electric dipole in nature. This was suggested as the dominate type of transition by Van Vleck in 1937 (46). Once again, the mechanism proposed for permitting electric dipole transitions to occur, albeit weakly, is the admixing of opposite parity $4f^{N-1}5d$ configurations with the $4f^N$ configuration by the odd order terms in the crystal field (Eq.(4)).

A theory to predict the intensity of the absorption lines of a specific rare earth was developed independently by Judd (47) and Ofelt (48). To accomplish this, the line strength (Eq.(8)) must be calculated. Using intermediately-coupled wavefunctions for the $4f^N$ configurations, the initial and final states may be written, using first order perturbation theory

$$\langle a| = \langle f^N[\alpha SL]J| - \sum_{\phi} \frac{\langle f^N[\alpha SL]J|V_{cf}^{odd}|\phi\rangle\langle\phi|}{E_a - E_\phi} \qquad (12)$$

$$|b\rangle = |f^N[\alpha'S'L']J'\rangle - \sum_{\phi} \frac{|\phi\rangle\langle\phi|V_{cf}^{odd}|f^N[\alpha'S'L']J'\rangle}{E_\phi - E_b} \qquad (13)$$

where V_{cf}^{odd} are the odd-order terms of the crystal field and ϕ represents the eigenstates of the opposite parity configuration, which is at some energy E_ϕ above the ground state. Judd and Ofelt both use two assumptions to make the following calculations tractable. First, it is assumed the $4f^{N-1}5d$ configuration is so removed in energy from the $4f^N$ configuration that the energy denominators in Eqs.(12) and (13) may be replaced by some average value E. Then it is assumed that the $4f^{N-1}5d$ state is essentially degenerate, i.e. the splittings within this configuration are negligible compared to the energy of the entire configuration. With these assumptions, and the methods introduced by Racah to express the operators (49-52) the line strength may be expressed

$$S(aJ;bJ') = e^2 \sum_{t=2,4,6} \Omega_t |\langle f^N[\alpha SL]J||U^{(t)}||f^N[\alpha'S'L']J'\rangle|^2 \qquad (14)$$

where the average energy value E, the crystal field parameters, the radial integrals, and any contribution due to vibronic transitions are incorporated into the parameters Ω_t. The doubly reduced matrix elements have

been tabulated for the $4f^N$ configurations (53).

To calculate the matrix elements of Eq.(14) one must have the appropriate eigenfunctions $|f^N[\alpha SL]J\rangle$, these are found by taking the free ion eigenfunctions for the $4f^N$ configuration, given by $|f^N\alpha SLJ\rangle$ and transforming to the intermediate-coupling scheme

$$|f^N[\alpha SL]J\rangle = \sum_{\alpha,S,L} C_{\alpha,S,L}|f^N\alpha SLJ\rangle \qquad (15)$$

The eigenfunctions are then found by diagonalizing the combined electrostatic and spin-orbit matrices to obtain the energy eigenvalues. Through the use of an iterative program, the set of coupling coefficients which give the best least squares fit of the calculated energy levels to the observed energy levels may be found. Since the energy levels of the trivalent rare earth ions change negligibly with host, the squared term in Eq.(14) changes negligibly. References for the matrix elements of most of the rare earths are cited in the excellent review article by Riseberg and Weber (54).

As mentioned earlier, the parameters Ω_t contain quantities which are difficult to calculate. To circumvent this difficulty the Ω_t values have been treated as parameters to be obtained from experiment. This is achieved by using the expression for the line strength (Eq.(14)) in the equation for the oscillator strength

(Eq.(9)). After experimentally determining the oscillator strengths (Eq.10)) an iterative approach may be used to find the Ω_t parameters which give the best-fitted oscillator strengths. It has been found that the fitted and measured oscillator strengths usually agree within 25% or better in crystals, glasses, and solutions (22,24,25,54-59).

By using free-ion eigenstates, equal population in the Stark levels of the initial J state are assumed, a condition which is only approximately fulfilled at room temperature. It has been found that the addition of transitions to many different terminal states tends to average the effects of unequal level population.

There are limitations to application of the Judd-Ofelt theory, as it is now called. Obviously, the value of the concentration, N, must be known in order to calculate the oscillator strengths. There are limits on the accuracy of these quantities. There are several ions in which the Judd-Ofelt theory does not apply, due to violations of its assumptions. These ions are Pr^{3+},Sm^{3+},Eu^{3+}, and Tb^{3+}. For Pr^{3+} and Sm^{3+} it has been observed that the calculated oscillator strengths of the higher energy levels do not agree with the experimentally observed values. This is indicative of a breakdown of the closure approximation made in the theory, due to the proximity of the $4f^{N-1}5d$ configuration with the higher energy levels of the $4f^N$ configuration (58).

For Eu^{3+} in the oxysulfides this failure is believed due to charge transfer states occurring at energies lower than those of the $4f^{N-1}5d$ states, which could result in a higher degree of interconfigurational mixing (61). For Eu^{3+} and Tb^{3+}, many of the matrix elements are very small and thus can be more sensitive to the choice of eigenstates. The effects of J-mixing can also have greater effects in this situation (58).

While good agreement between the fitted and measured values of the oscillator strengths is necessary for the validity of the theory, it alone is not sufficient. After all, fitting six or more equations with three unknowns constitutes an overdetermined situation. However, the line strength is also necessary to calculate the spontaneous emission probability from one level to another.This is defined as

$$A(aJ;bJ') = \frac{64\pi^4\nu^3}{3(2J+1)hc^3} S(aJ;bJ') \qquad (16)$$

which is related to the radiative lifetime τ of an excited state i by

$$\frac{1}{\tau} = \sum_j A(i,j) \qquad (17)$$

where the summation is over electric and magnetic dipole transitions to all terminal states j. The fluorescence branching ratio is given by

$$\beta_{ij} = \sum_{j} \frac{A(i,j)}{A(i,j)} = \tau_i A(i,j) \qquad (18)$$

These last two quantities are measurable. It has been found that for those excited states where the decay is purely radiative (as opposed to having additional, nonradiative transitions) the calculated lifetime is within 10-20% of the measured lifetime, an error comparable to the average error in fitting the oscillator strengths (25,56-60). For branching ratios the errors can be higher, since the branching ratio is between a pair of J-multiplets, however, the observed and calculated branching ratios are usually within 30% of each other (59,62).

In conclusion, it can be seen that the Judd-Ofelt theory accounts reasonably well for the measured absorption intensities and radiative lifetimes of most of the ions in the rare earth series. This can be of great use, as some other techniques for calculating radiative lifetimes require equipment which has been carefully calibrated for accurate intensity measurements, which is a tedious procedure. Also, as will be seen in the next section, radiative lifetime values are necessary to determine the nonradiative rate for a specific level of an ion-host combination, a quantity which is also of importance.

Nonradiative Transitions

Multiphonon Emission

So far we have concerned ourselves with the absorption and emission of photons between the levels of an impurity ion in a host. The effect of the static lattice on the energy levels has also been briefly discussed. However, the lattice is never static, so the crystal field at the ion site undergoes an oscillatory behavior due to the motions of the lattice. The lattice vibrational quanta are phonons, which have symmetry properties determined by the symmetry of the host, and energies determined by the masses of the constituent ions and their binding forces. The interaction between the photons and the ion can have profound effects on the optical properties. These effects include line broadening and vibrational sidebands in the optical spectra. This interaction is also responsible for nonradiative transitions, where a transition between adjacent levels occurs with the emission of the number of phonons necessary to conserve energy. Such a process is called multiphonon emission. There are two methods which have been successful in predicting the effect of temperature, and other factors, on the multiphonon emission. Common to both methods is the assumption that the total wavefunction of the ion is separable into a purely electronic part and a purely nuclear part. This is the basis of the Born-

Oppenheimer approximation; that the electrons respond instantly to changes in the lattice potential, while the lattice responds only to the average positions of the electrons. As originally formulated by Kiel (63,64) this calculation involves the use of time-dependent perturbation theory, starting with a Taylor series expansion of the crystal-field Hamiltonian H_{cf} about the equilibrium ion positions

$$H_{cf} = V_{cf} + \sum_i V_i \phi_i + \frac{1}{2} \sum_{i,j} V_{i,j} \phi_i \phi_j + \ldots \qquad (19)$$

where Q_i is the i-th normal mode coordinate, V_{cf} is the static crystal field (Eq.(4)), and V_{ij} are partial derivatives of the crystal field. For a nonradiative transition between two states involving the emission of p phonons, Kiel used the first-order term of Eq.(19) in p-th order time-dependent perturbation theory. Alternatively, the p-th order term could be used in first-order perturbation theory (65). While the expression for such a process can be written out, evaluating it is a problem, as it involves explicit knowledge of the crystal field tensor operators, and the frequency, polarization, and propagation of the vibrations (54). Consequently, this theory has only produced order-of-magnitude estimates of the nonradiative rates. However, it is possible, starting with Kiel's equation, to develop an expression based on experimentally derived parameters which explains the temperature

dependence of the multiphonon emission rate (54,65,66). This expression is

$$W_{NR}(T) = W_{NR}(0)\{n_i + 1\}^{p_i} \tag{20}$$

where $W_{NR}(0)$ is the nonradiative rate at 0 K and n_i is the Bose-Einstein occupation number of the i-th phonon mode.

$$n_i = \{\exp(\hbar\omega_i/kT) - 1\}^{-1} \tag{21}$$

The number of phonons p_i of equal energy $\hbar\omega_i$ required to make the transition across an energy gap ΔE to the next-lower level is given by

$$p_i\hbar\omega_i = \Delta E \tag{22}$$

Combining Eqs.(20) and (21), we have

$$W_{NR}(T) = W_{NR}(0)\left\{\frac{\exp(\hbar\omega_i/kT}{\exp(\hbar\omega_i/kT) - 1}\right\}^{p_i} \tag{23}$$

Experimentally, the multiphonon emission rate of an excited state i to an adjacent, lower-lying state, in the absence of competing nonradiative processes, is

$$W_{NR} = \frac{1}{\tau_{obs}} - \frac{1}{\tau_i} \tag{24}$$

where τ_{obs} is the observed lifetime of the state i and τ_i is the radiative lifetime (Eq.(17)). It has been observed for many ion-host combinations that when W_{NR} is determined over a range of temperatures, Eq.(23) may be applied successfully (25,56,60,62,65,66). In each case it has been found that the phonon energy $h\omega$ always corresponds to the highest-energy optical-branch phonons, i.e. the transition occurs in the lowest order of p possible, so long as energy is conserved. The only exceptions to this rule occur when the highest-energy phonons are very weak compared to the rest of the phonon spectrum. In this case the more dominant, lower-energy phonon modes appear to be responsible for the multiphonon emission (60).

In these same investigations it has been noted that, if the nonradiative rates for a number of rare earth ions in a particular host are plotted semilogarithmically versus the energy gap, ΔE, a linear trend is followed. This has been interpreted in terms of the Kiel model in the following way:

The ratio of the multiphonon emission rate of a p phonon process, W_p, to the rate for a (p-1) phonon process is

$$W_p/W_{p-1} = \varepsilon \tag{25}$$

where ε is a constant ($<<1$) whose magnitude determines the rapidity of the convergence of the perturbation expansion.

The rate for the p phonon process can thus be written

$$W_p = C\varepsilon^p = C\exp([\ln(\varepsilon)/\hbar\omega]\Delta E) \tag{26}$$

where use of Eq.(22) has been made. Letting $-\ln(\varepsilon)/\hbar\omega = \alpha$ Eq.(26) becomes

$$W_p = C\exp(-\alpha\Delta E) \tag{27}$$

where C and α are positive constants characteristic of the host. Equation (27) has been shown to be valid (to within a factor of about two) for a number of hosts, both crystalline and glassy (25,54,60,65,66). Only in the case where strong selection rules apply does it become invalid (54,60,64). Extrapolation to gaps which may be bridged by one or two phonons must be regarded with some scepticism, as the statistical averaging of the individual features of the phonon modes and electronic states begins to break down (54).

The second approach for determining multiphonon emission rates is based on the configuration coordinate model (36,43,61,68,69). This model explains the shape of many broadband transitions as well. Instead of attempting to take into account the effect of all possible lattice modes, this model assumes that the only mode of importance is a "breathing" mode, where the surrounding ions move in

and out symmetrically about the optically active ion. It also assumes that a harmonic oscillator model can describe the ground and excited states of the system (through use of the Born-Oppenheimer approximation). A single variable, the distance between the optically active ion and its neighbors, describes the energy of these states. This variable is called the configuration coordinate Q. Assuming that only a single phonon frequency $\hbar\omega$ is of importance, the ground state parabola is described by the expression

$$U_g = \frac{1}{2} M_g \omega^2 Q_o^2 \tag{28}$$

where M_g is the effective mass of the ground state of the system (usually taken as the reduced mass of the system). The ion-lattice state is described by $|\psi\chi_n>$, where ψ is the electronic state of the ion, χ_n is the vibrational state of the lattice, and n is the occupancy of the vibrational mode. The excited state parabola is described by

$$U_e = U_g + \frac{1}{2} M_e \omega^2 (Q - Q_o)^2 \tag{29}$$

where Q is the average value of the configuration coordinate while the ion is in the excited state. The vibrational states of this parabola are labelled χ_m. This change in the configuration coordinate is termed the Franck-Condon offset, and is a measure of the difference

in sensitivity of the two electronic levels to changes in the environment. A measure of this difference in sensitivity is determined by a dimensionless quantity called the Huang-Rhys parameter, S_o, defined by

$$S_o h\omega = \frac{1}{2} M\omega(Q - Q_o)^2 \tag{30}$$

The probability that an absorption from the ground state $|g,\chi_n\rangle$ to an excited state $|e, \chi_m\rangle$ will occur is proportional to the square of the matrix element $\langle e,\chi_m |\vec{D}| g,\chi_n\rangle$, where $\vec{D}$ is again the appropriate multipole operator. To proceed further in the evaluation of this matrix element the assumption is made that the transition occurs so quickly that the surrounding ions appear "frozen", i.e. no change in the configuration coordinate. This is known as the Franck-Condon approximation. This approximation allows us to separate the electronic and vibrational parts of the wavefunction so the matrix element becomes $\langle e|\vec{D}| g\rangle\langle\chi_m| \chi_n\rangle$. For a large range of values of n and m, particularly as S_o becomes larger, the overlap integral $\langle\chi_m| \chi_n\rangle$ is nonzero. Thus a transition can be accompanied by the creation or annihilation of phonons. It is precisely these overlap integrals that we wish to evaluate to calculate the multiphonon emission rate (creation of phonons).

Several methods for doing this have been developed. One model, by Huang and Rhys (67) assumes that the force

constants of the ground and excited states, i.e. the values of M and ω, are equal. Treating the lattice as a dielectric continuum and assuming that the impurity (in their model, an F center) can be treated as a static charge distibution when calculating the lattice vibrations, their expression for a nonradiative transition involving the emission of p phonons may be written

$$W_{NR} = N\exp(-S_o \frac{1+r}{1-r}) \sum_{j=0}^{\infty} (S_o \frac{r}{1-r})^j (S_o \frac{1}{1-r})^{p+j} / j!(p+j)! \qquad (31)$$

where $r=\exp(-\hbar\omega/kT)$ and N is a constant incorporating the electronic matrix elements and having a value on the order of $10^{13} s^{-1}$. This formulation is somewhat different from the final form given by Huang and Rhys (67), and is used here because it's easier to do numerical computations.

Another model for calculating the overlap integral has been developed by Struck and Fonger (61,70). In their model, the restrictions on the equality of force constants and phonon energies for the ground and excited states are relaxed. The resulting expressions are not exact and must be solved numerically. However, good results may be achieved in systems where considerable interaction with the lattice (radiation defects or transitions to p or d states) occurs (71,72). Struck and Fonger have also shown that their expression reduces exactly to the Huang-Rhys formula (Eq.(31)) in the limit of equal force constants and phonon energies (61).

While the configuration coordinate model provides a

clearer picture of the physics behind ion-lattice interactions, one should not lose sight of its inherent restrictions. Due to the assumption of interaction with a symmetric lattice mode, effects due to the odd-parity components of the lattice modes are neglected. This can make the contribution of vibronically-allowed transitions larger than predicted. Also, the configuration coordinate model is harmonic in nature, and it is possible that anharmonic modes can make a significant contribution to the ion-lattice interactions (73,74).

Energy Transfer

Our discussion has so far been limited to processes which occur independently among optically active ions assumed to be isolated from one another. As the concentration of these ions increases the possibility that clustering of ions will occur, or that an interaction will occur between ions which are not nearest neighbors. Experimentally, it is found that as the concentration of a fluorescent ion is increased, the fluorescence will increase. This continues, until at some concentration the intensity begins to decrease. This phenomena, known as concentration quenching, is indicative that the excitation energy is being transferred nonradiatively out of the system of luminescent ions.

It has also been observed that it is possible to have one type of ion absorb light and then transfer this

energy nonradiatively to a second set of ions, which in turn emit. This is known as sensitized luminescence and is a process which has been actively exploited commercially. It is the understanding of the physics of this process that will be of importance here.

In the simplest case sensitized luminescence is a single-step process which occurs when the emission of the initially-excited ions (sensitizers) is in resonance with the absorption of the other type of ions (activators). If the sensitizers are not constituents of the host, this process is known as impurity-sensitized luminescence. Much of our theoretical understanding of the energy transfer process has its basis in the work of Förster (75-77) on energy transfer through the electric dipole interaction. This interaction was also treated and extended to other, higher multipolar interactions and the exchange interaction by Dexter (78). Because of the sucessfullness of their approach, the single-step resonant energy transfer process is often referred to as Förster-Dexter energy transfer. There are more complicated energy transfer processes than the ones mentioned, for more information there are excellent review articles by Riseberg and Weber (54), Reisfeld (79) Powell and Blasse (80) and Wright (81).

The energy transfer rate for Förster-Dexter energy transfer may be treated by time-dependent perturbation theory (c.f. Eq.(5)). The Hamiltonian for the energy transfer is the electromagnetic interaction, which can be

expressed as a multipolar expansion about the sensitizer-activator distance R_{sa}. Because the transition energies have finite widths the wavefunctions and density of states can be treated as functions of energy. To properly treat this, the wavefunctions can be normalized with respect to energy, and the density of states factor can be absorbed into the normalization parameters. The expression for the energy transfer rate for an electric dipole-dipole interaction, P_{dd} is

$$P_{dd} = \frac{3\hbar^4 c^4}{4\pi n^4 \tau_s} \left(\frac{1}{R_{sa}} \right)^6 Q_A \int \frac{f_s(E)\, F_A(E)\, dE}{E} \qquad (32)$$

where τ_s is the radiative lifetime of the sensitizer. $Q_A = \sigma_A(E)dE$, where $\sigma_A(E)$ is the absorption cross section, found by dividing the absorption coefficient at energy E by the concentration of activator ions. The normalized lineshape functions for the sensitizer and activator are given by $f_s(E)$ and $F_A(E)$, respectively, so that

$$f_s(E)dE = 1 \qquad (33)$$

$$F_A(E)dE = 1 \qquad (34)$$

where $F_A = \sigma_A / Q_A$. The integral in Eq(32) is thus a measure of the degree of spectral overlap between the sensitizer's emission and the activator's absorption. It is often

convenient to compare the value of R_{sa} to a critical interaction distance R_o, where the energy transfer rate is equal to the sensitizer's radiative rate. By collecting terms in Eq.(32) and defining them as R_o, this equation may be expressed as

$$P_{dd} = \frac{1}{\tau_s} \left(\frac{R_o}{R_{sa}} \right)^6 \tag{35}$$

Formulas similar to Eq.(32) may be developed for higher multipole interactions such as electric dipole-quadrupole or electric quadrupole-quadrupole (78). Usually it is easier to calculate the energy transfer rate P_{dd} and use the following expressions for the other interactions (80)

$$P_{dq} = \left(\frac{\lambda}{R_{sa}} \right)^2 \left(\frac{f_q}{f_d} \right) P_{dd} \tag{36}$$

$$P_{qq} = \left(\frac{\lambda}{R_{sa}} \right)^4 \left(\frac{f_q}{f_d} \right)^2 P_{dd} \tag{37}$$

where λ is the wavelength of the transition and f_d,f_q are the oscillator strengths of the dipole and quadrupole transitions, respectively.

From the exponent of R_{sa} in Eqs.(35-37) it can be seen that the electric dipole-dipole interaction has the longest range, while the electric quadrupole-quadrupole interaction is of much shorter range.

For energy transfer by the exchange interaction, the matrix element in Eq(5) may be interpreted as the

Coulombic interaction between the charge distributions of the sensitizer and activator. Since each wavefunction decreases exponentially with distance from the nuclei, the transfer probability varies exponentially with the sensitizer-activator separation. Consequently, the exchange interaction is not an effective means of energy transfer for ions located much more than over-next-neighbors away, making this interaction comparable in range with the electric quadrupole-quadrupole interaction (78,82).

CHAPTER III

EXPERIMENTAL PROCEDURES

The crystals used in this study were grown at the Oklahoma State University Crystal Growth Facility. The starting material, consisting of crystal chips of MgF_2, zone-refined RbF, and the particular dopant were placed in a vitreous carbon crucible and grown under an argon atmosphere by the Bridgeman method. Ammonium bifluoride (NH_4HF_2) or Teflon chips were also placed in the crucible as an oxygen getter.

The erbium-doped fluorozirconate glass was provided by M. Drexhage and R. Brown of the Rome Air Development Center, Hanscom AFB. The batch compositions were (in mol.%) $57ZrF_4$, $34BaF_2$, $3LaF_3$, $4AlF_3$, $2ErF_3$, and $57ZrF_4$, $35.5BaF_2$, $3LaF_3$, $4AlF_3$, $0.5ErF_3$. The starting materials were combined with NH_4HF_2 and heated at 850°C in vitreous carbon crucibles under an atmosphere of CCL_4 and argon. The glasses were cast into cylindrical boron nitride molds and annealed for about 12 hrs. at 300°C before being slowly cooled to room temperature.

Samples were cut with a diamond saw and polished by hand lapping on successively finer sheets of abrasive obtained from Buehler, Ltd.

For low temperature measurements, a Sulfrian helium cryostat, or a CTI Cryodyne Cryocooler Model 21SC were utilized. The cryogenerator was equipped with a resistance heater which allowed temperature control within ±1K over the range 14-300K. The temperature was monitored with a gold-iron vs chromel thermocouple mounted on the cold finger just above the sample. Above room temperature the sample was enclosed in a copper holder with windows for the excitation and fluorescence. A copper-constantan thermocouple was mounted directly on the sample for temperature measurement. Temperature control was within ±5K with a resistance heater.

Optical absorption measurements were made using a Cary 14 spectrophotometer with either (0-0.1)- or (0-1.0)-OD (optical density) slidewires, or a Perkin-Elmer 330 spectrophotometer. The optical density is defined as the common logarithm of the ratio of incident to transmitted light. The optical density is related to the absorption coefficient α , a more useful quantity, through the relation

$$\alpha = \frac{(\ln 10)\ OD}{t} \tag{38}$$

where t is the sample thickness in cm.

Emission- and excitation-spectra measurements were made by exciting the samples with light from an Illumination Industries 75-W xenon-arc lamp which had been

passed through a 0.22 m Spex Minimate monochrometer. Two gratings could be used in the Minimate. One grating has specifications of 1200 gr/mm with a reciprocal dispersion of 4 nm/mm, and was blazed at 300 nm. The other grating was a 600 gr/mm grating blazed at 750 nm with a reciprocal dispersion of 8 nm/mm. The 1200 gr/mm grating can be used over the range 250-800 nm, while the 600 gr/mm grating can be used over the range 350-1600 nm. The exciting light was focussed using quartz lenses onto the edge of the sample (for samples of about 2 mm thickness) and the fluorescence was collected at right angles. For thin samples the sample was turned about 30^{o} so the sample area illuminated and the area detected are at the same point. This minimized stray light. The fluorescence was focussed with calcium fluoride lenses into a 0.8 m Spex 1702 monochromator which has a 600 gr/mm grating blazed at 1600 nm with a reciprocal dispersion of 2 nm/mm. The emerging light was routed to the appropriate detector, this being either a cooled PbS cell (Optoelectronics OTC-22-53TXX) or a photomultiplier tube (PMT) (RCA 7102 or RCA C31034) cooled with a Pacific Photometrics Model 33 thermoelectric cooler. The signal from the PbS cell was preamplified by a Keithley Model 103A nanovolt amplifier and passed to a Keithley Model 840 lock-in amplifier. The signal from the PMT was preamplified by a Keithley Model 427 current amplifier and passed to the lock-in amplifier. The reference signal was provided by a phototransistor placed in the edge of the

exciting light, which was modulated by a variable speed, single hole chopper. The output of the lock-in amplifier may be displayed on a Houston Instruments 2000 X-Y recorder, or routed to a Hewlett-Packard model 3455A digital voltmeter which was interfaced to a Hewlett-Packard Model 85 microcomputer. This allows excitation or emission spectra to be recorded on disc for further processing.

Lifetime measurements were made utilizing a Biomation Model 610B transient recorder and a Nicholet Model 1070 signal averager. The reference signal from the phototransistor was used to trigger these units to take data as the chopper extinguished the exciting light. This could be repeated many times until an acceptable signal was accumulated. The stored signal is displayed on an oscilloscope, and may be output via a RS232C interface to the HP-85 for storage and analysis, or sent to the X-Y recorder, where it can be plotted in linear or semilogarithmic form. With this apparatus, lifetimes in the visible and ultraviolet portions of the spectrum as short as 10 μs can be measured. This limit is imposed by the speed of the preamplifier. In the infrared region, the lifetime measurements are limited to about 300 μs when the detector is uncooled, and 1.5 ms when cooled.

Some fluorescence risetime measurements were also performed by using the filtered light of a General Radio Model 1538A Strobotac xenon flashlamp. This lamp provides pulses of 20 μs duration.

To correct the emission spectra a General Electric QL-157 quartz-iodine standard lamp, whose characteristics are traceable to the National Bureau of Standards was used. To correct the excitation spectra, a Photo Research Model 310 photometer-radiometer was placed at the sample position. This gives intensity readings, on a calibrated scale, from 430 nm to 920 nm. For shorter wavelengths, a 0.5 mg/ml solution of Rhodamine B in ethylene glycol, obtained from Perkin-Elmer, was used. This allowed excitation spectra to be corrected from 250 nm to 600 nm. Below 250 nm the intensity of the xenon lamp is too weak to be useful.

When necessary, sharp cut-off filters purchased from Hoya Optics or Melles Griot were used in the excitation or emission beam path to minimize stray light.

CHAPTER IV

EXPERIMENTAL RESULTS

$RbMgF_3$:Er and $RbMgF_3$:Er,Mn

Several types of $RbMgF_3$ crystals, containing different amounts of ErF_3 and MnF_2 were prepared. Three crystals, having premelt doping levels of 1wt.%, 1at.%, and 0.5at.% Er^{3+} were grown. One crystal with 1at.% Er^{3+} and 1at.% Mn^{2+} added to the starting materials was also prepared. The concentration of Er^{3+} in the resulting crystals was much less than the starting concentration and was not uniformly distributed through the crystal. The concentration of Er^{3+} in the 1wt.% -doped crystal varied from 9000ppm to 400ppm as measured by mass spectroscopy. In addition to the above crystals, several specimens of a $KMgF_3$ crystal which was grown with 0.1at.% Er^{3+} in the melt were obtained for comparison with the $RbMgF_3$ samples.

Crystals of $RbMgF_3$ have six Mg^{2+} ions per unit cell. Figure 2 shows that all Mg^{2+} sites, where it is expected the Er^{3+} ions will substitute, have C_{3v} symmetry. Two of the Mg^{2+} sites have equidistantly placed F^- ions, making the local symmetry closer to O_h, while four of the Mg^{2+} ions are in constricted sites with F^- ions at nonequi-

distant points. The necessary charge composition for Er^{3+} ions could be by fluorine interstitials, as in CaF_2, by Rb^+ vacancies, or by alkali ions in Mg^{2+} sites (84). Since the samples were not intentionally doped with alkali ions, this last possibility seems remote. In any case the 4f electrons of Er^{3+} are shielded by the outer 5s and 5p electrons and are not easily perturbed by the ligands. Evidence that this is the case is shown in Fig. 4. This figure indicates that the energy levels for Er^{3+} are essentially those of the free ion, as expected from the discussion in the Theory section, regardless of whether charge compensation is or is not needed. The energy levels in Fig. 4 were determined from the low-temperature emission and excitation data shown in Figs. 5 and 6. In Fig. 5 the emission peak marked with a star is the transition $^4S_{3/2} \rightarrow {}^4I_{13/2}$ and the double-peaked emission near 5000 cm^{-1} is due to Ho^{3+} present as an impurity in the 1wt.% Er^{3+}-doped sample. The excitation spectrum shown in Fig. 6 was taken using the Er^{3+} $^4I_{11/2} \rightarrow {}^4I_{15/2}$ and the Ho^{3+} $^5I_7 \rightarrow {}^5I_8$ emissions. The excitation spectrum for the Ho^{3+} emission contained many bands due to Er^{3+} and allowed the accurate determination of the $^4I_{13/2}$ level. In the low-resolution case, the excitation spectra showed no difference between the $RbMgF_3$:Er and the $RbMgF_3$:Er,Mn samples. However, when the $^2H_{11/2}$ level is excited the emission from a sample of $RbMgF_3$:Er differs from the emission of a sample of $RbMgF_3$:Er,Mn as shown in Figs. 7(a) and 7(b),

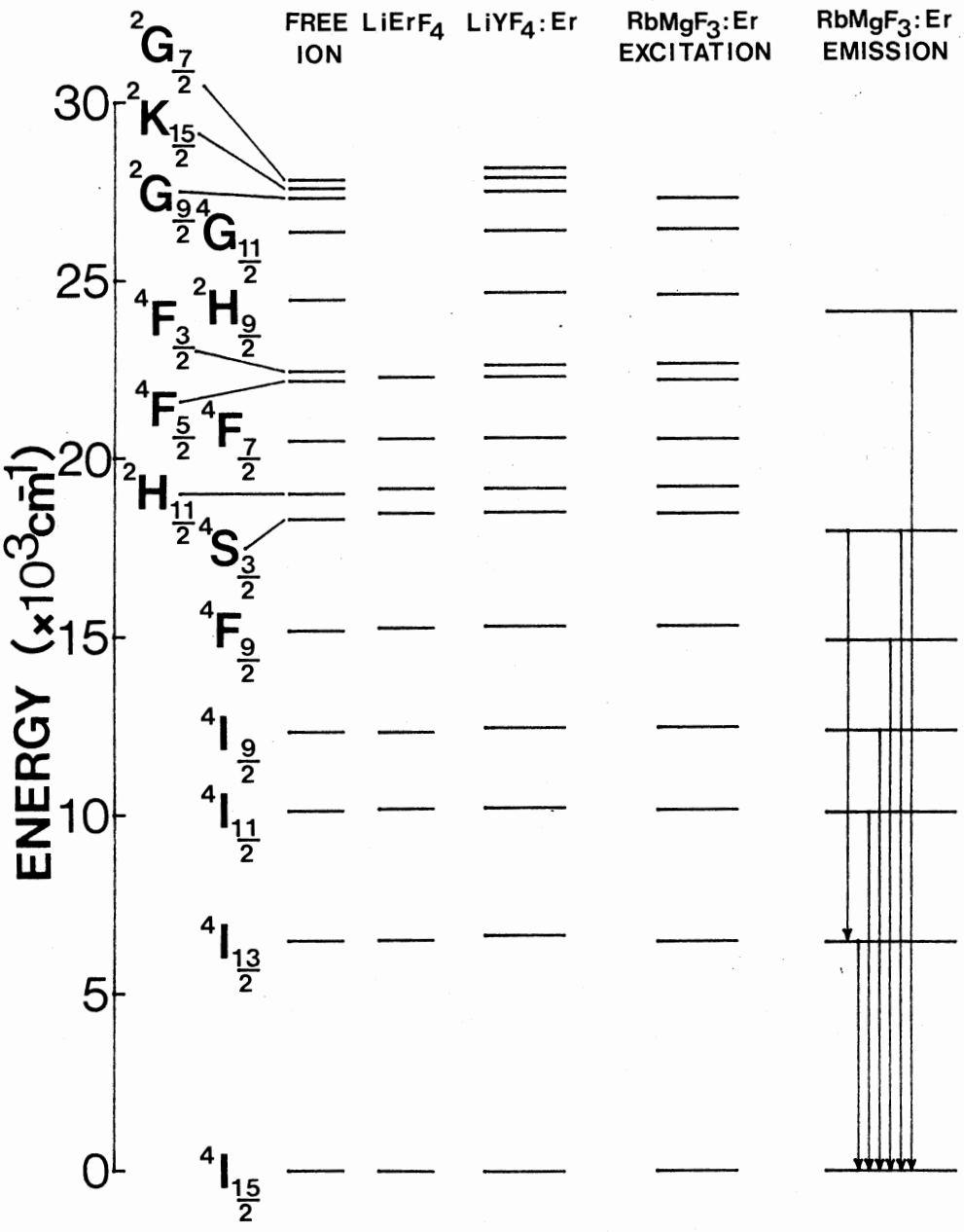

Figure 4. Energy-Level Diagram of Er^{3+} as a Free Ion (Ref. 35), in $LiErF_4$ (40), in $LiYF_4$ (85), and for the Present Work

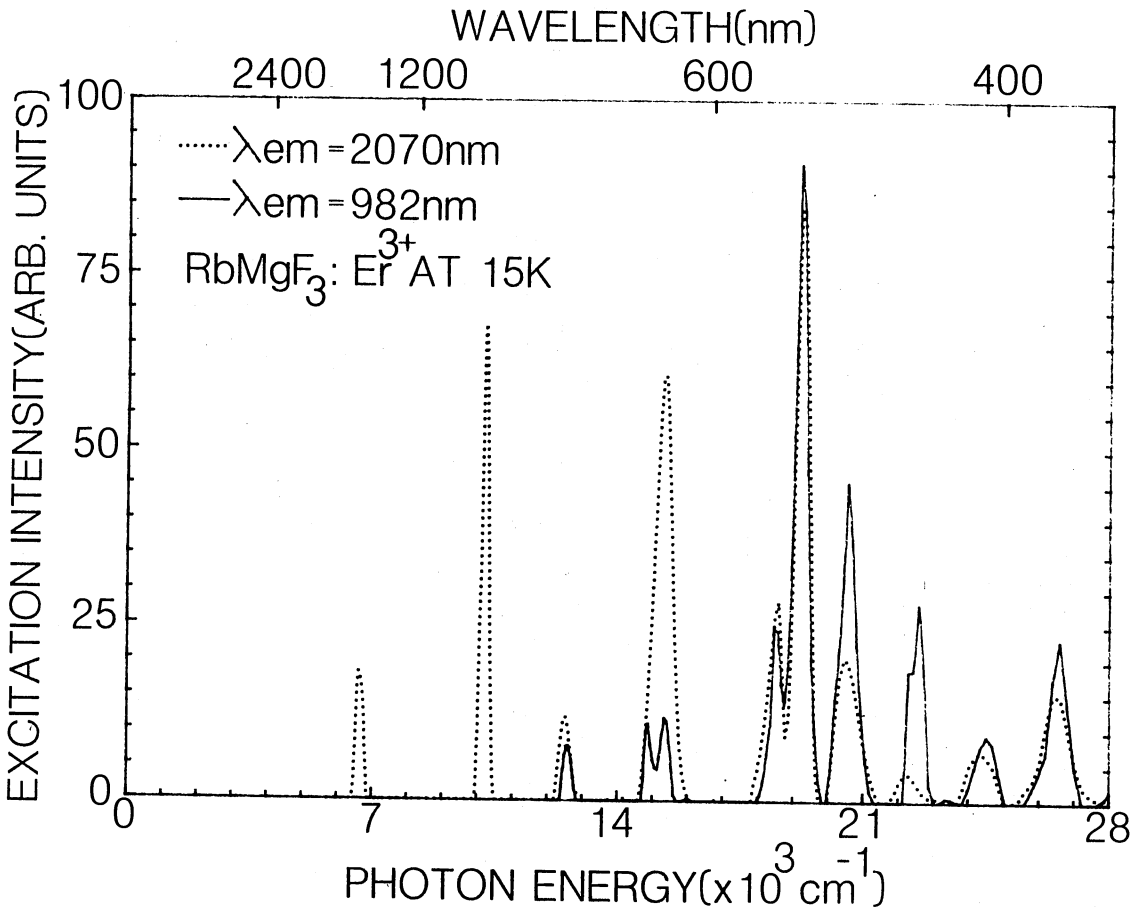

Figure 5. Excitation Spectrum of $RbMgF_3$:Er,Mn. Transitions Monitored Were the Er^{3+} $^4I_{11/2} \rightarrow {}^4I_{15/2}$ (982 nm) and the Ho^{3+} $^5I_7 \rightarrow {}^5I_8$ (2070 nm)

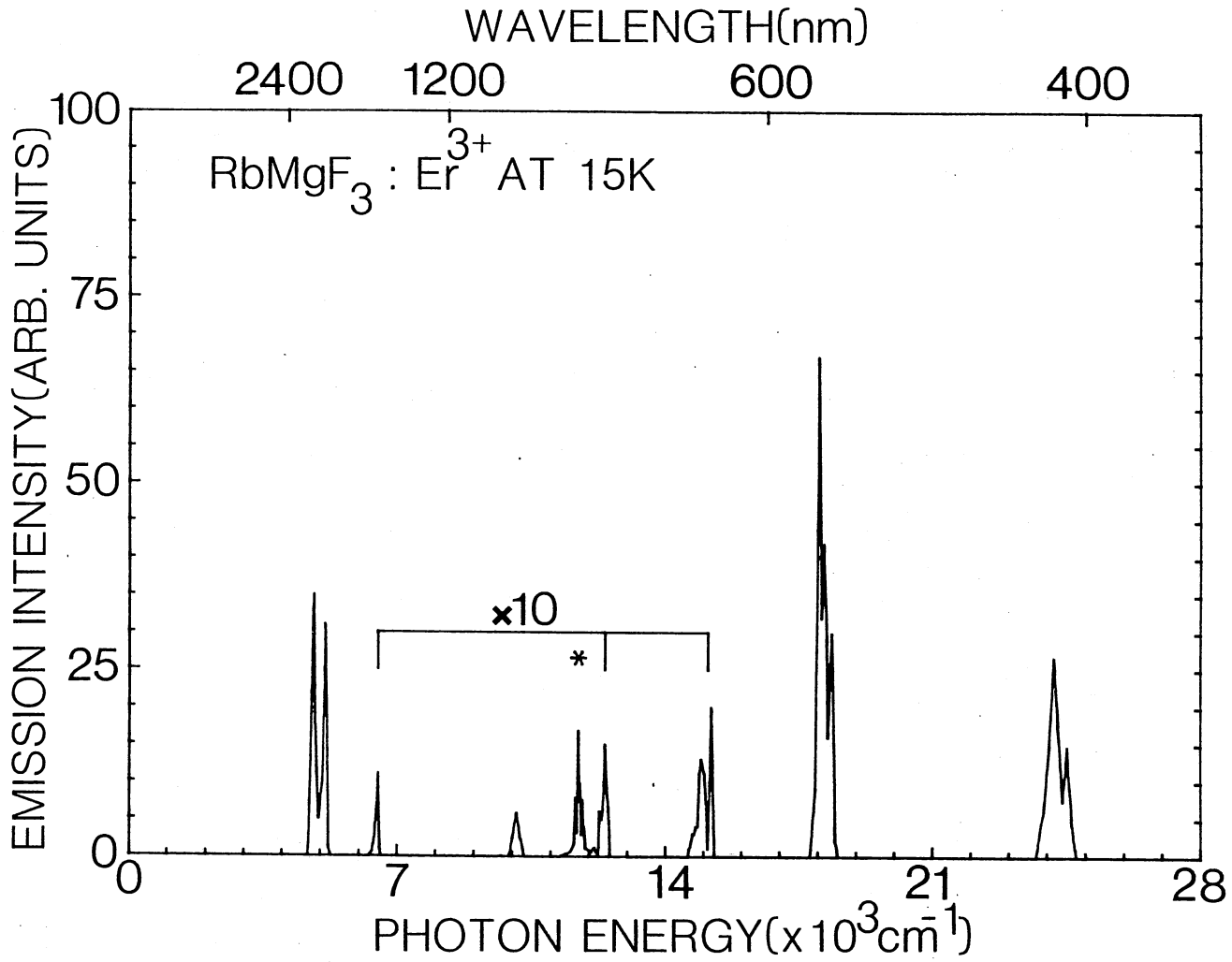

Figure 6. Emission Spectrum of $RbMgF_3$:Er. The Band Marked * Corresponds to the $^4S_{3/2} \rightarrow {}^4I_{13/2}$ Transition. The Intensities of the Bands Marked x10 Were Increased by this Amount

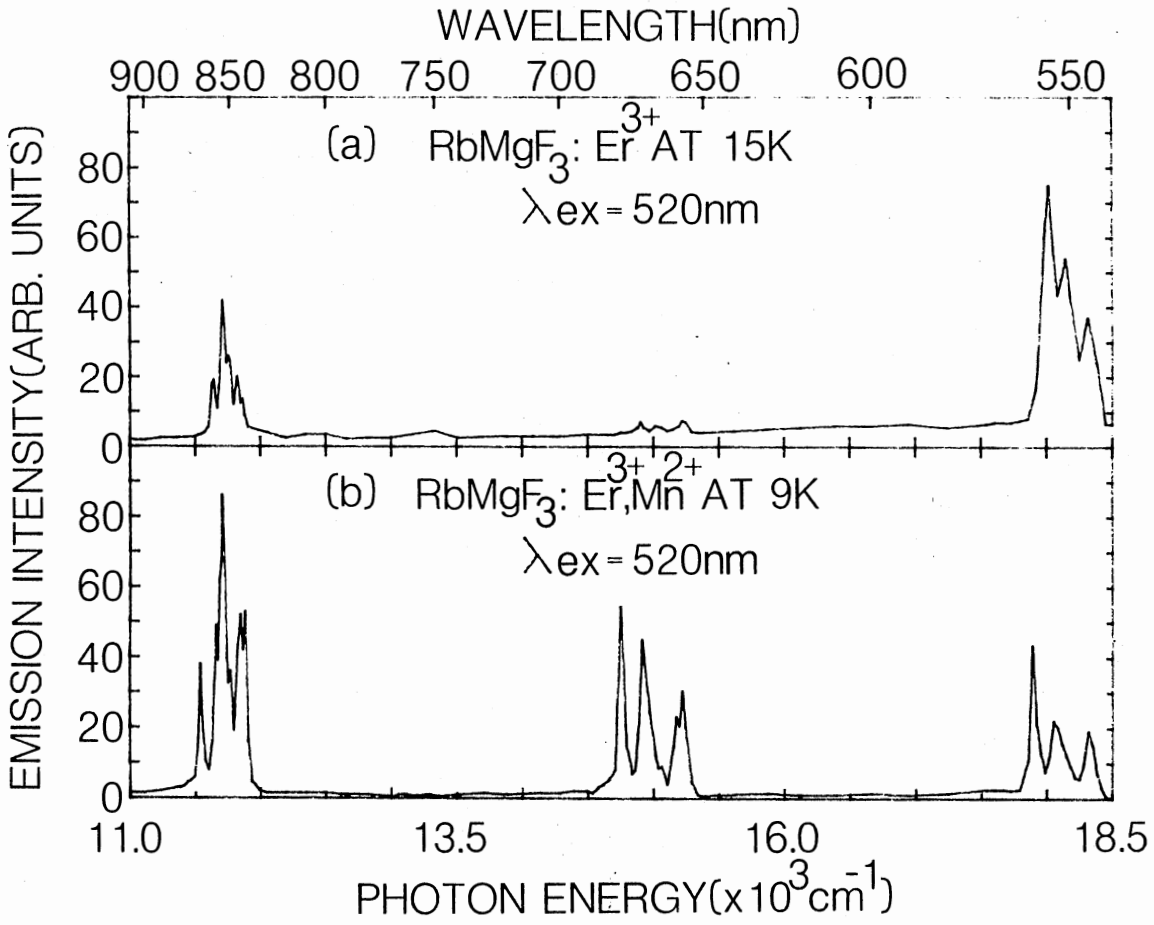

Figure 7. Emission of Er^{3+} in (a) $RbMgF_3$ and (b) $RbMgF_3$:Mn in the visible and near-infrared region of the spectrum. Resolution in both cases is 2 nm

respectively. Note that the $^4F_{9/2} \rightarrow {}^4I_{15/2}$ emission is larger in proportion to the $^4S_{3/2} \rightarrow {}^4I_{15/2}$ emission in the $RbMgF_3$:Er,Mn samples. Also the $^4S_{3/2} \rightarrow {}^4I_{15/2}$ emission intensities are different for the two types of samples.

In order to determine the crystal-field splitting of the $^4I_{15/2}$ ground state of Er^{3+} in this host, low-temperature high-resolution emission spectra were obtained for the $^4S_{3/2} \rightarrow {}^4I_{15/2}$ and $^4F_{9/2} \rightarrow {}^4I_{15/2}$ transitions in both Er- and Er,Mn-doped samples. For a site of C_{3v} symmetry the $^4I_{15/2}$ multiplet is split into eight levels by the noncubic crystal field (35,43). This splitting should be evident in the emission spectra. Figure 8(a) is the emission spectrum for the $^4S_{3/2} \rightarrow {}^4I_{15/2}$ transition in $RbMgF_3$:Er. Figures 8(b) and 8(c) show the emission spectra for the same transition in $RbMgF_3$:Er,Mn at 7K and 78K, respectively. Comparison of Fig. 8(a) with Fig. 8(b) immediately shows that a series of lines denoted "b" appears in the $^4S_{3/2} \rightarrow {}^4I_{15/2}$ emission in $RbMgF_3$:Er,Mn that is not in the emission from $RbMgF_3$:Er. The arrows in Fig. 8(c) indicate a set of emissions which appear as the sample is warmed. This set of emissions is separated from the "b" series of emissions by 62 cm^{-1}. Figure 9(a) is the emission spectrum for the $^4F_{9/2} \rightarrow {}^4I_{15/2}$ transition in $RbMgF_3$:Er. Figure 9(b) is the emission spectrum for the same transition in $RbMgF_3$:Er,Mn.

The intense transition from the $^4S_{3/2}$ level to the $^4I_{13/2}$ level in the low-temperature emission spectrum was

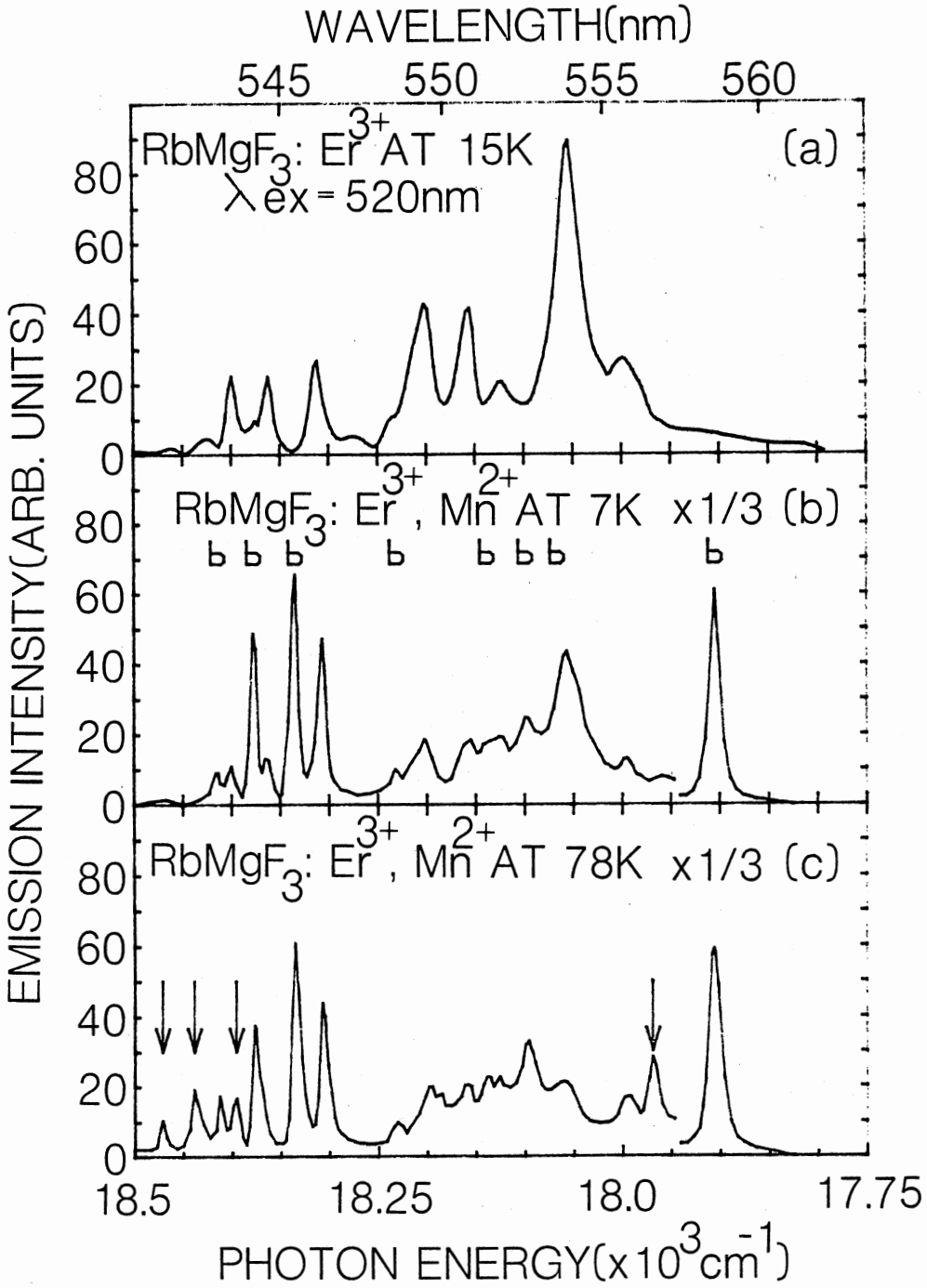

Figure 8. $^4S_{3/2} \rightarrow {}^4I_{15/2}$ Emission of Er^{3+} in (a) $RbMgF_3$ and (b),(c) $RbMgF_3$:Mn

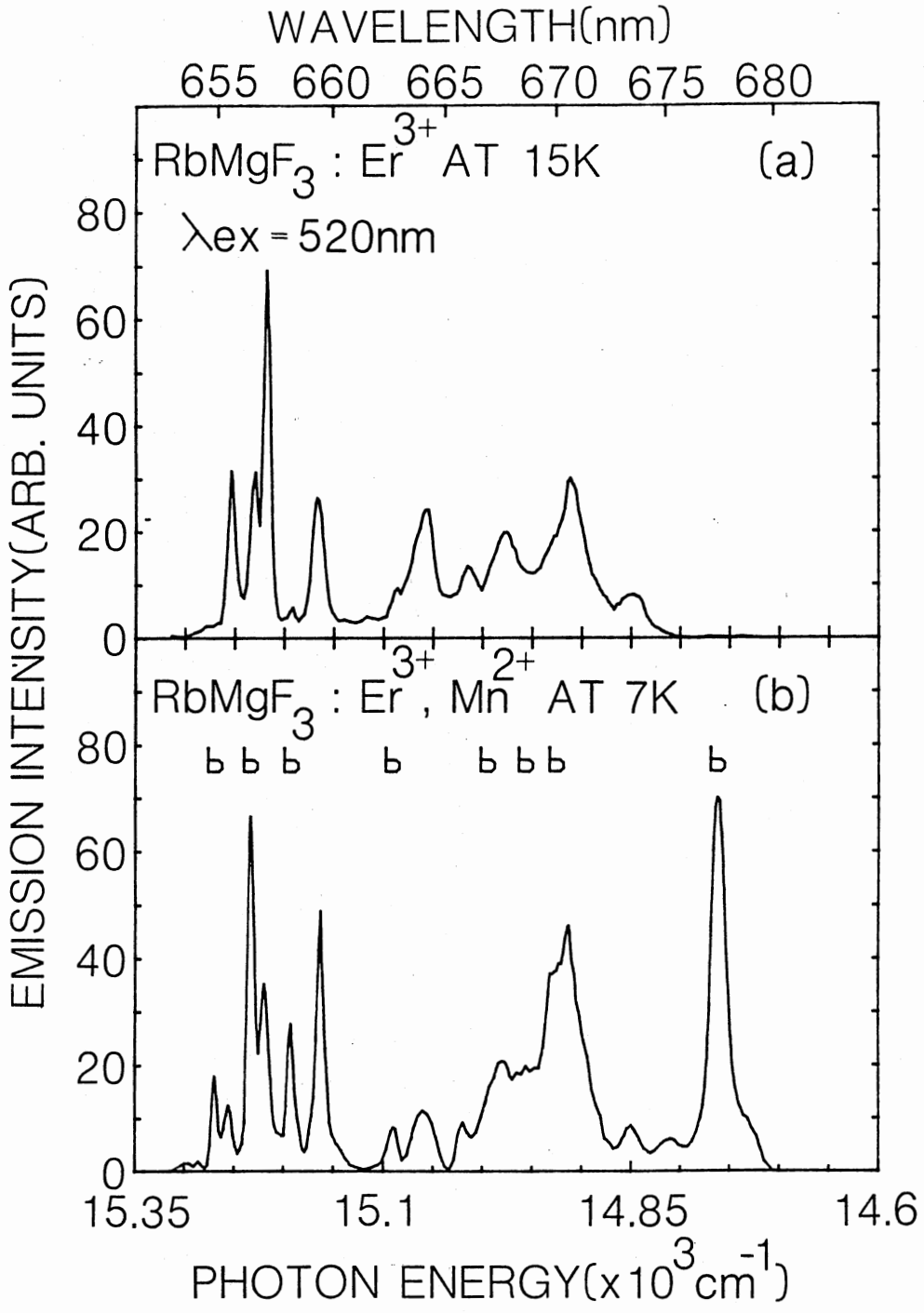

Figure 9. $^4F_{9/2} \rightarrow {}^4I_{15/2}$ Emission of Er^{3+} in (a) $RbMgF_3$ and (b) $RbMgF_3$:Mn

measured for both types of samples to evaluate the crystal-field splitting. The $^4I_{13/2}$ multiplet is split into seven levels in a noncubic crystal field (35). The spectra obtained are shown in Figs. 10(a)-(c). Figure 10(c) shows that as the temperature increases once again a set of emissions, marked by arrows, appears 62 cm^{-1} to higher energy from the lowest-temperature "b" emissions in Fig. 10(b).

In principle the low-temperature absorption spectra of Er^{3+} can be used to determine how many sites are occupied by the Er^{3+} ion. This assumes the absorption bands do not greatly overlap, and the Er^{3+} concentration for each of the site symmetries is sufficient for detection. The $^4S_{3/2}$ multiplet is the simplest excited state of Er^{3+}, since it is split into only two levels in a noncubic crystalline field. The absorption spectrum of the $^4I_{15/2} \rightarrow {}^4S_{3/2}$ transition in $RbMgF_3$:Er,Mn at three different temperatures is shown in Fig. 11. At 8K the absorption spectrum (solid line) consists of four bands. At this temperature only the lowest level of the $^4I_{15/2}$ multiplet is populated, so only two absorption bands for the $^4I_{15/2} \rightarrow {}^4S_{3/2}$ transition are possible for each Er^{3+} site. Since two sets of two lines are found, it appears Er^{3+} in $RbMgF_3$ occupies at least two sites. In order to assign the observed lines to ions in a particular site the temperature dependence of the spectrum was measured. As the temperature was raised, new absorption bands appear at

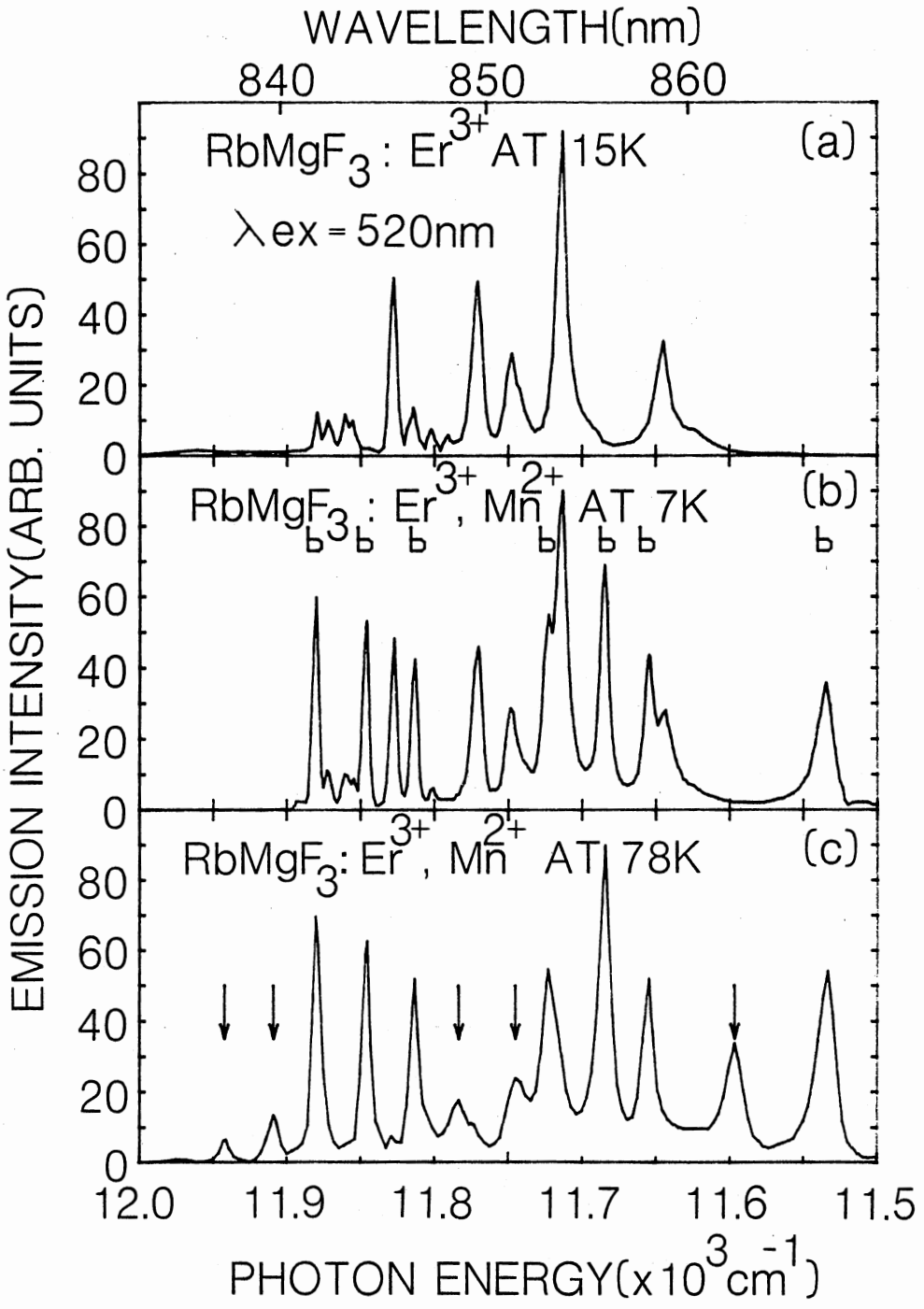

Figure 10. $^4S_{3/2} \rightarrow {}^4I_{13/2}$ Emission of Er^{3+} in (a) $RbMgF_3$ and (b), (c) $RbMgF_3$:Mn

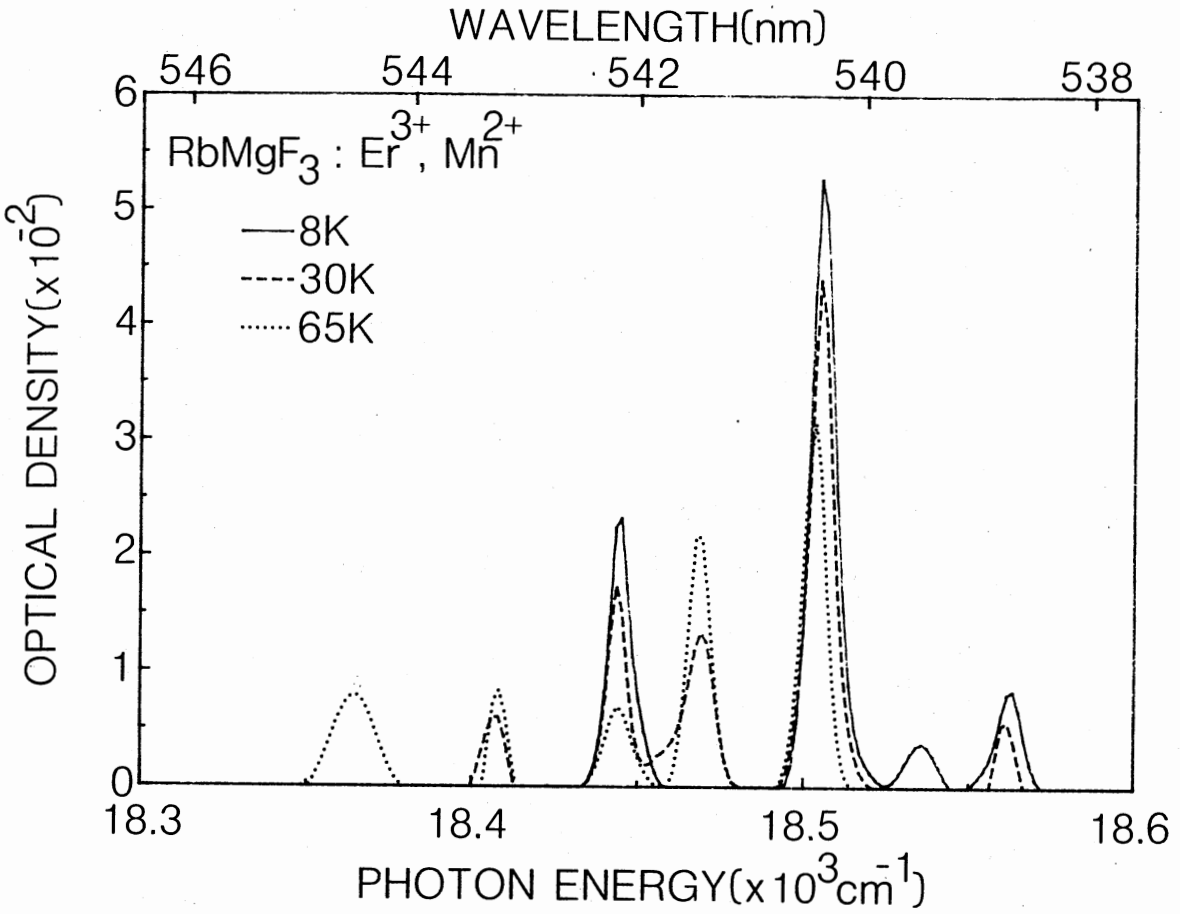

Figure 11. Absorption Spectrum of the $^4S_{3/2}$ Level in $RbMgF_3$:Mn. The Sample Thickness was Approximately 2 mm

35 and 78 cm^{-1} on the low-energy side of the absorption bands at 18504 cm^{-1} (540.42 nm) and 18444 cm^{-1} (542.19 nm) as portrayed in Fig. 11. These new bands are the result of the Boltzmann population of the next two highest levels in the $^4I_{15/2}$ ground state multiplet for the Er^{3+} ions in one of these sites. The energy separation of the bands at 18504 and 18444 cm^{-1} is 60 cm^{-1}. This agrees, within experimental error, with the observed energy separation between the emission bands marked with arrows and the "b" bands in Figs. 8(c) and 10(c). Note that in Fig. 8(b) the difference in energy between the first three "b" bands, at 18418, 18382, and 18340 cm^{-1} is 36 and 78 cm^{-1}. This matches the energy splittings of the first three levels of the $^4I_{15/2}$ multiplet, for Er^{3+} in one of the two sites, which were derived from the absorption data in Fig. 11. The corresponding transitions for the $^4F_{9/2} \rightarrow {}^4I_{15/2}$ emission, shown in Fig. 9(b), have splittings of 36 and 77cm^{-1} which are again in excellent agreement with the absorption data. From these observations it is clear that the absorption bands at 18504 and 18444 cm^{-1} characterize the $^4S_{3/2}$ excited state for one site, with the "b" emissions in Fig.8(b) arising from transitions to the ground state for Er^{3+} in that site. Similarly, the remaining absorption and emission bands, shown in Figs. 11 and 8(b), respectively, are due to Er^{3+} in the other site.

The absorption spectrum of a $RbMgF_3$:Er sample at 30K is depicted in Fig. 12. Comparison with Fig. 11 shows that

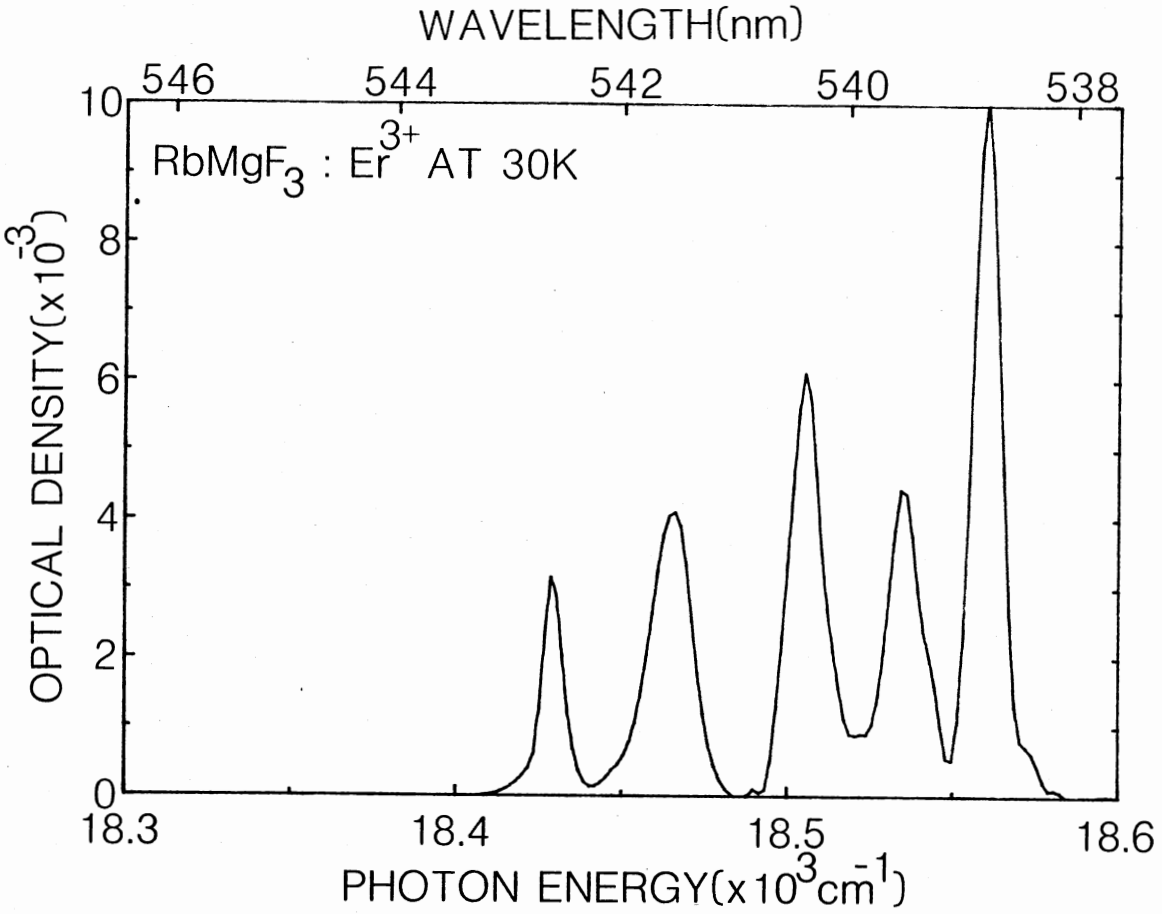

Figure 12. Absorption Spectrum of the $^4S_{3/2}$ Level at 30K in $RbMgF_3$:Er. The Sample Thickness was 7 mm

absorption occurs at the same energies, although the relative intensities of the absorption bands are different. Also the bands at 18407 and 18444 cm^{-1} are unmeasurable due to the lower erbium concentration in the sample. Nevertheless, Er^{3+} clearly occupies the same sites in $RbMgF_3$ as it does in $RbMgF_3$:Mn, although emission is from one site. For convenience, the site from which the Er^{3+} ion luminesces in $RbMgF_3$ shall be referred to as site 1. The other Er^{3+} site shall be referred to as site 2. From these data the energy splittings of the $^4I_{15/2}$ ground state and the $^4S_{3/2}$ excited state of Er^{3+} in both sites were calculated. This information is shown in Fig. 13.

From the data illustrated in Fig. 10 for the $^4S_{3/2} \rightarrow {}^4I_{13/2}$ emission, the $^4I_{13/2}$ energy levels can be determined. The Er^{3+} ions in site 2 have levels split by 0, 34, 67, 158, 195, 225, and 346 cm^{-1}. The site 1 ion levels are more difficult to obtain, but five of these are at 11827, 11770, 11748, 11713, and 11643 cm^{-1}. The absorption and emission lines for $RbMgF_3$:Er,Mn are shown in Tables 2 and 3, respectively.

Lifetime measurements provide useful information about an ion and its surroundings. Weber (56) showed that in LaF_3:Er a relationship exists for the magnitude of the energy gap between adjacent levels and the lifetime. This is an empirical observation of the energy-gap relation discussed in the Theory section. Weber showed that as the energy gap decreased so did the lifetime. For energy gaps

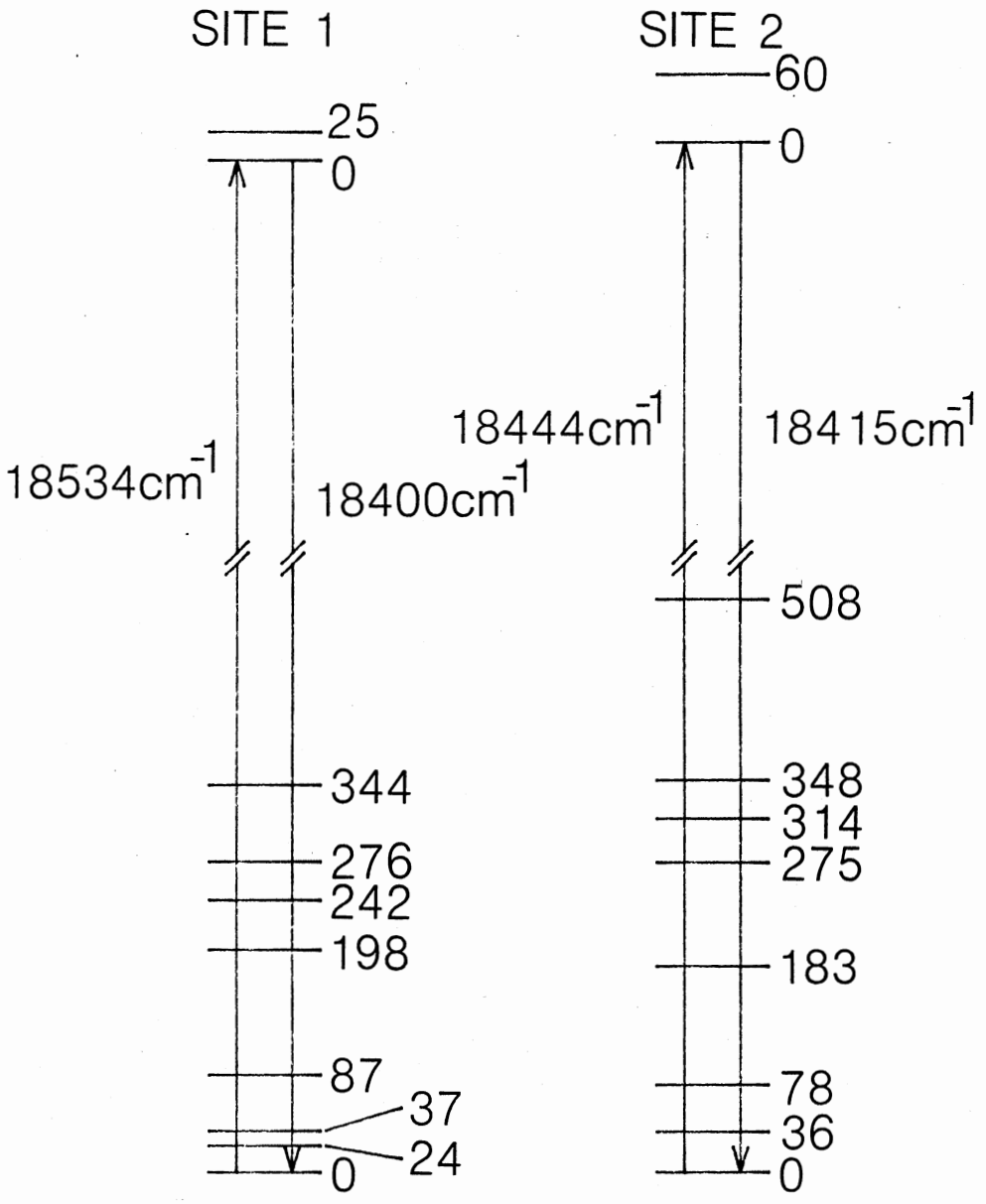

Figure 13. Energy Splittings of the $^4S_{3/2}$ and $^4I_{15/2}$ Multiplets for Er^{3+} in Site 1 and Site 2 in $RbMgF_3$

TABLE II

ABSORPTION OF Er^{3+} IN $RbMgF_3$:Mn AT 9K. IF KNOWN, THE SPECIFIC Er^{3+} SITE IS LISTED

TRANSITION	ENERGY (cm^{-1})	SITE	TRANSITION	ENERGY (cm^{-1})	SITE
	20735			15534	
	20680			15469	
	20659		$^4F_{9/2}$	15406	
$^4F_{7/2}$	20625			15343	
	20588			15296	
	20560				
	20494			6762	
				6730	2
	19414			6695	2
	19391			6656	2
	19369		$^4I_{13/2}$	6623	
	19332			6606	
$^2H_{11/2}$	19318			6568	2
	19254			6535	2
	19233			6500	2
	19187				
	19147				
	18563	1			
$^4S_{3/2}$	18536	1			
	18505	2			
	18443	2			

TABLE III

EMISSION OF Er^{3+} IN $RbMgF_3$:Mn AT 9K

TRANSITION	ENERGY (cm^{-1})	SITE	TRANSITION	ENERGY (cm^{-1})	SITE
$^2H_{9/2} \rightarrow {}^4I_{15/2}$	24510		$^4I_{9/2} \rightarrow {}^4I_{15/2}$	12407	
	24155				
				11882	2
	18415	2		11874	
	18400	1		11862	
	18379	2		11856	
	18376	1		11847	2
	18363	1		11829	1
	18337	2		11812	2
	18313	1	$^4S_{3/2} \rightarrow {}^4I_{13/2}$	11802	
	18232	2		11772	1
$^4S_{3/2} \rightarrow {}^4I_{15/2}$	18202	1		11750	1
	18158	1		11724	2
	18140	2		11714	1
	18124	1		11683	2
	18101	2		11656	2
	18067	2		11645	1
	18056	1		11536	2
	17995				
	17907	2	$^4I_{11/2} \rightarrow {}^4I_{15/2}$	10101	
	15270	2	$^4I_{13/2} \rightarrow {}^4I_{15/2}$	6494	
	15256	1			
	15233	2			
	15231	1			
	15220	1			
	15193	2			
	15163	1			
	15090	2			
$^4F_{9/2} \rightarrow {}^4I_{15/2}$	15060	1			
	15020	1			
	14995	2			
	14980	1			
	14957	2			
	14926	2			
	14913	1			
	14848				
	14762	2			

which must be spanned by 10 or more phonons the emission is essentially totally radiative, giving temperature-independent lifetimes, while for energy gaps spanned by approximately three or less phonons, nonradiative decay is so dominant that fluorescence is totally quenched. For energy gaps intermediate in magnitude between the two extremes, multiphonon emission causes the lifetime to be temperature dependent. A careful series of lifetime measurements were made on the more intense emission lines from $RbMgF_3$:Er and $RbMgF_3$:Er,Mn. The lifetimes of the $^4S_{3/2} \rightarrow {}^4I_{15/2}$, $^4S_{3/2} \rightarrow {}^4I_{13/2}$, and $^4F_{9/2} \rightarrow {}^4I_{15/2}$ emissions of Er^{3+} in $RbMgF_3$, where only site 1 luminesces, were measured to compare with the lifetime values obtained for that site in $RbMgF_3$:Er,Mn. The lifetimes measured at 15K are listed in Table 4. Estimated errors for single exponential lifetimes are about 5%. For double exponential lifetimes the errors for the longer lifetimes are about 5% and about 20% for the shorter lifetimes. For all lifetime measurements the $^2H_{11/2}$ level was excited. Note that the $^4S_{3/2}$ lifetimes for site 1 in $RbMgF_3$, and the same site in $RbMgF_3$:Mn, have essentially the same single exponential lifetime, while the site 2 lifetimes in $RbMgF_3$:Mn have double lifetimes. Within experimental error, the $^4F_{9/2}$ luminescence decay was single exponential and had the same value for both sites. However, the initial decay of the site 1 luminescence deviated from a single exponential behavior. No such behavior was observed for the site 2

TABLE IV

LIFETIMES OF Er^{3+} IN $RbMgF_3$ AND OTHER FLUORIDE HOSTS (In ms)

MATERIAL	$^4S_{3/2}$	$^4F_{9/2}$	$^4I_{11/2}$	$^4I_{13/2}$
LaF_3 (Ref. 56) T=77K	1.0	0.75	11	13
$LiYF_4$ (Ref. 85) T=4.2K	0.65	0.65	7	14.6
MnF_2 (Ref. 89) T=4.2K	---	0.27	10	22
$RbMnF_3$ (Ref. 87) T=4.2K	---	0.042	9	28
$RbMgF_3$ T=15K	0.174	0.34	---	13
$RbMgF_3$:Mn T=15K SITE 1	0.16	0.34	---	---
SITE 2	0.08,0.32	0.34	---	---

luminescence decay. In addition to these measurements the lifetime of the $^4I_{13/2}$ transition in $RbMgF_3$:Er was measured.

The temperature dependence of the $^4S_{3/2}$ lifetime is displayed in Fig. 14. Note that the site 1 lifetimes in $RbMgF_3$ and $RbMgF_3$:Mn have the same values and temperature dependence. The lifetimes decrease above 60K. The integrated intensities of the emission bands for both sites show similar behavior. At room temperature, luminescence is not observed from either site, whereas in LaF_3, CaF_2, or CdF_2, $^4S_{3/2}$ luminescence is observed above room temperature (56,83,86). The $^4I_{13/2}$ luminescence is temperature independent from 15 to 300K. This is consistent with earlier studies (56,85,87).

Preliminary studies were made on a sample of $KMgF_3$:Er. This crystal also contained 10-50ppm of inadvertently added Mn^{2+}, as did all our samples not intentionally doped with Mn^{2+}. If Er^{3+} substitutes for Mg^{2+}, charge compensation is required. If the charge compensation is not local the Er^{3+} ion will be in a site of O_h symmetry. For Er^{3+} in a site of cubic symmetry, the crystal field splits both the $^4I_{13/2}$ and $^4I_{15/2}$ multiplets into five levels (35). The high resolution emission spectra of the $^4S_{3/2} \rightarrow {}^4I_{15/2}$ and $^4S_{3/2} \rightarrow {}^4I_{13/2}$ transitions of Er^{3+} in $KMgF_3$ are shown in Figs. 15 and 16, respectively. Both spectra have no more than five bands, indicating that the Er^{3+} ion is in a site of cubic site

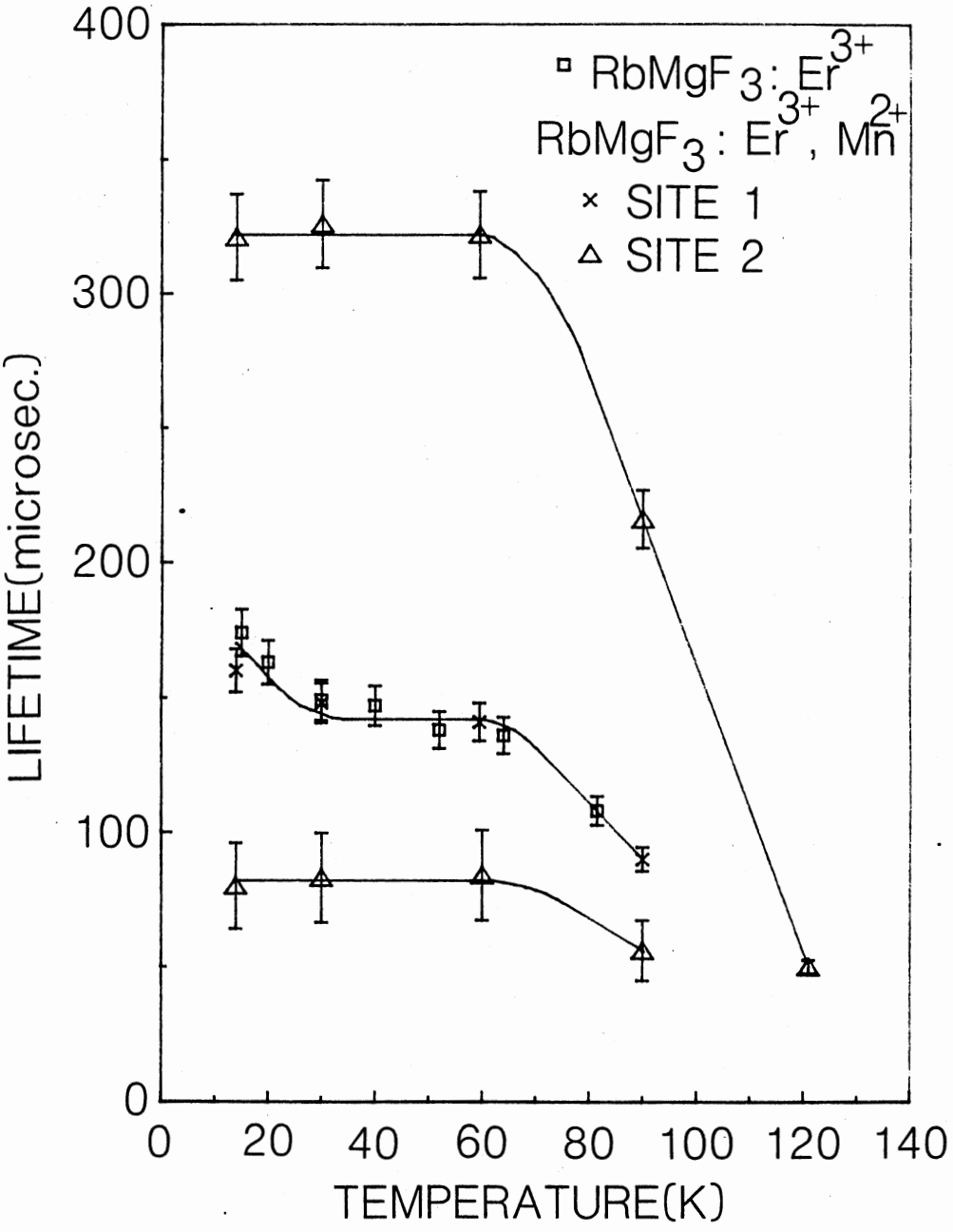

Figure 14. Temperature Dependence of the Er^{3+} $^4S_{3/2}$ Lifetime in $RbMgF_3$ and $RbMgF_3$:Mn

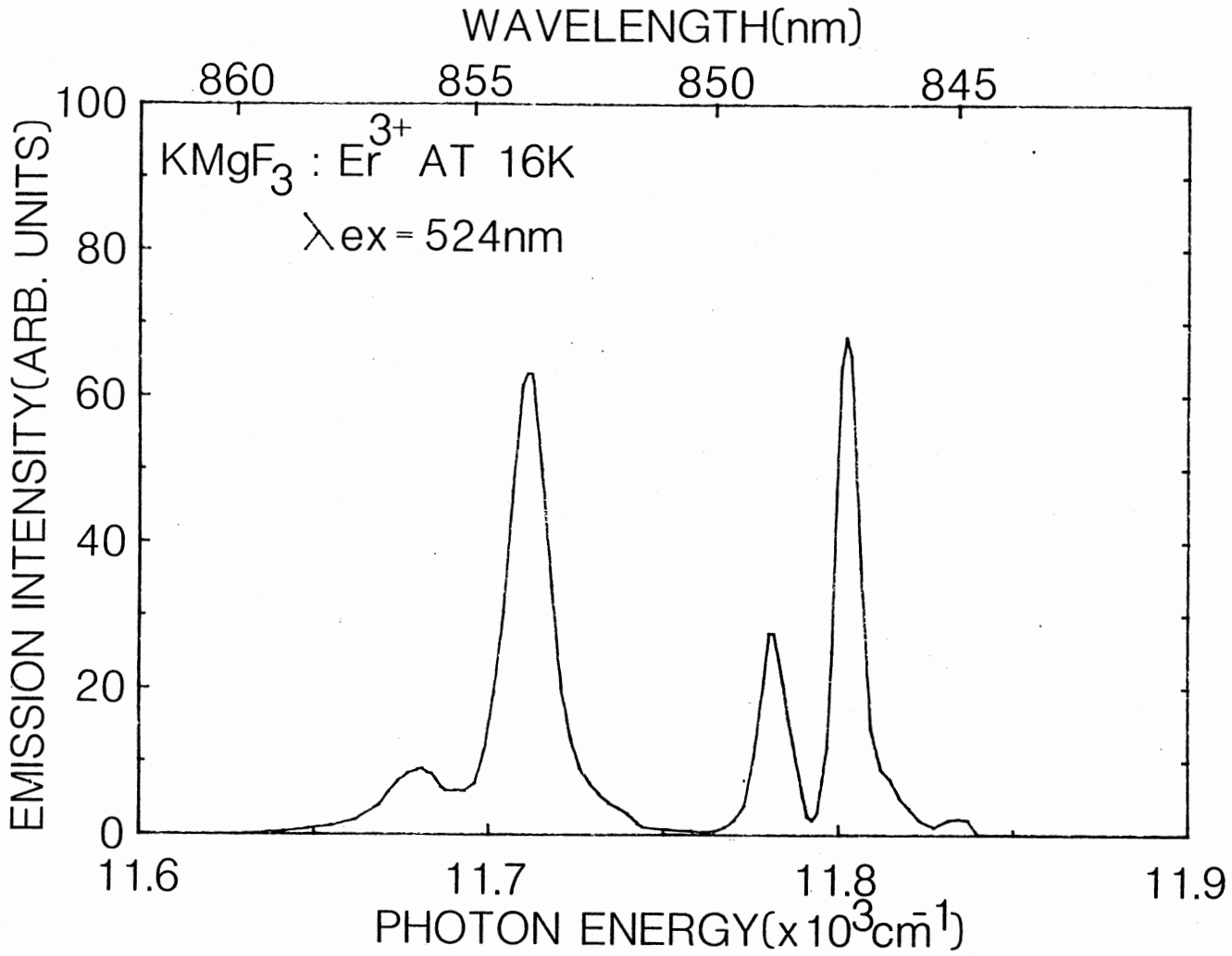

Figure 15. $^4S_{3/2} \rightarrow {}^4I_{15/2}$ Emission of Er^{3+} in $KMgF_3$

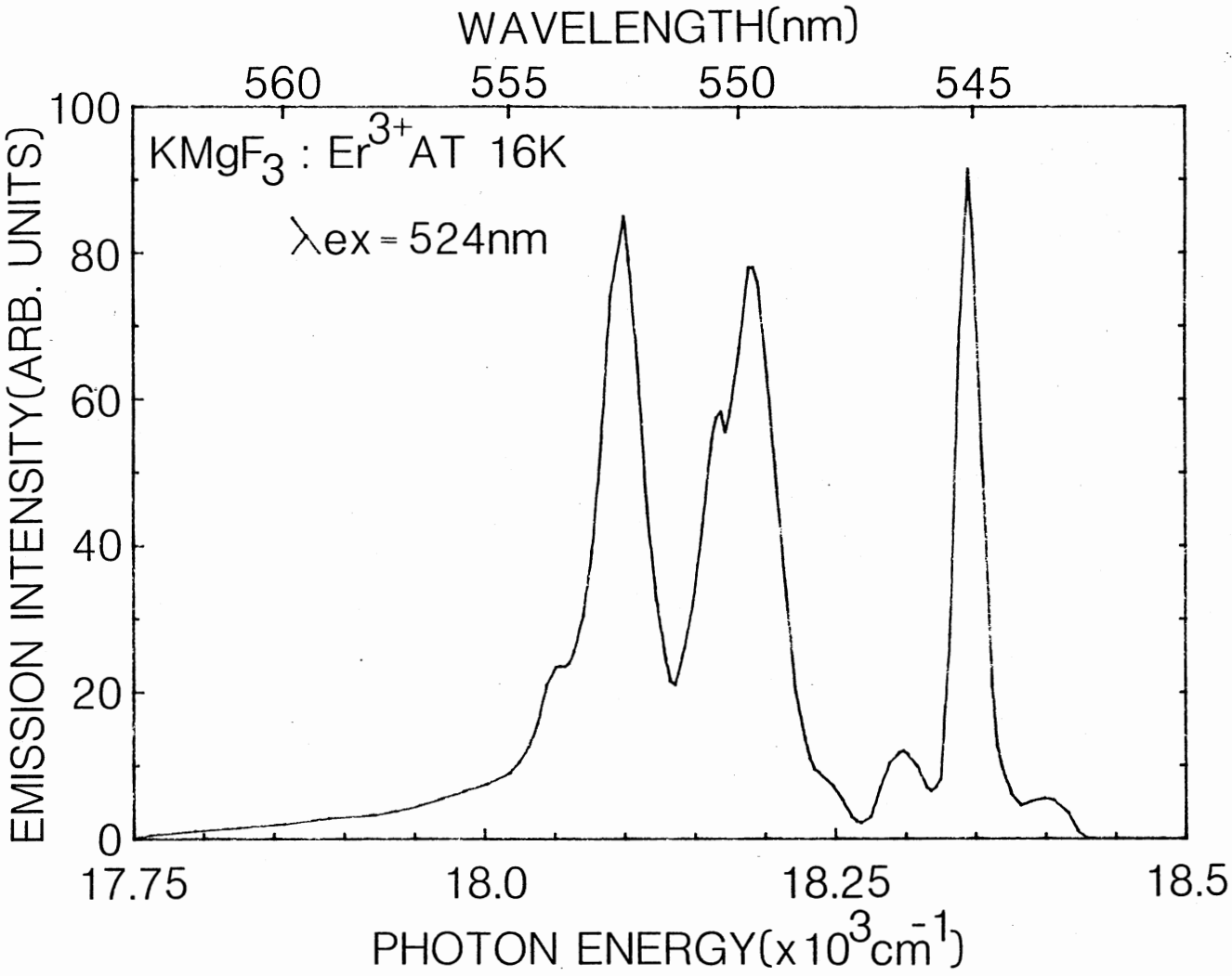

Figure 16. $^4S_{3/2} \rightarrow {}^4I_{13/2}$ Emission of Er^{3+} in $KMgF_3$

symmetry.

The $^4F_{9/2} \rightarrow {}^4I_{15/2}$ transition was measured and also found to consist of five bands. This suggests that the charge compensation is predominantly nonlocal. This conclusion is supported by the investigations of Abraham et. al. on the electron paramagnetic resonance of Er^{3+} in $KMgF_3$ (88).

Several other measurements on $KMgF_3$:Er were also made. When the $^2H_{11/2}$ level was excited, the emission spectrum in the visible region looked much like that shown in Fig. 7(b), with the $^4F_{9/2} \rightarrow {}^4I_{15/2}$ emission easily detected. When the $^2H_{11/2}$ level was excited, the lifetime of the $^4S_{3/2}$ emission was 71 μs, and the lifetime of the $^4F_{9/2}$ emission was 161 μs. No lifetime temperature-dependence measurements were made; however, it should be noted that luminescence from either the $^4S_{3/2}$ or $^4F_{9/2}$ level was not detected at room temperature.

$RbMgF_3$:Eu,Mn

The magnitude of the lifetimes of the visible Er^{3+} emissions, and the reduction of these values above 60K is not characteristic of this ion in many fluoride hosts. Inspection of the information in Table 4 shows that only for those hosts which have Mn^{2+} as one of their constituents are the lifetimes of the $^4F_{9/2}$ emission comparable. In these hosts the $^4S_{3/2}$ emission is entirely quenched, due to energy transfer to Mn^{2+} ions (87,89,90).

In an effort to further clarify the nature of this interaction, crystals of $RbMgF_3$:Eu,Mn were grown. The optical properties of $RbMgF_3$:Eu had been studied previously (15), providing the data base necessary to detect any changes in these properties when Mn^{2+} is added. Under UV excitation $RbMgF_3$:Eu emits a deep blue fluorescence, while $RbMgF_3$:Eu,Mn fluoresces pink to bright orange, depending on the concentration of Mn^{2+}. This Mn^{2+} emission, which is much more intense than seen in $RbMgF_3$:Mn, is suggestive of sensitized luminescence.

Two crystals were prepared for this study, one with initial melt concentrations $RbMg_{0.98}Mn_{0.01}F_3:Eu_{0.01}$, the other with initial melt concentrations $RbMg_{0.84}Mn_{0.15}F_3:Eu_{0.01}$. The impurities were added in the form of MnF_2 and $EuCl_3$.

The normalized room temperature absorption spectra of samples of $RbMgF_3$:Eu and $RbMgF_3$:Eu,Mn are shown in Fig. 17. The broad, intense absorption with maxima near 250nm is due to transitions from the $4f^7$ ground state configuration ($^8S_{7/2}$) to the $4f^65d^1$ excited state configurations (15) of Eu^{2+} and is characteristic of all samples. Previously, this band was reported as having a "flat-topped" maximum (15). It was found that this was an artifact of the instrumation "clipping" the absorption due to the attenuation of the transmitted beam reaching the point that it became comparable to the intensity of the stray light. To achieve correct results the sample thick-

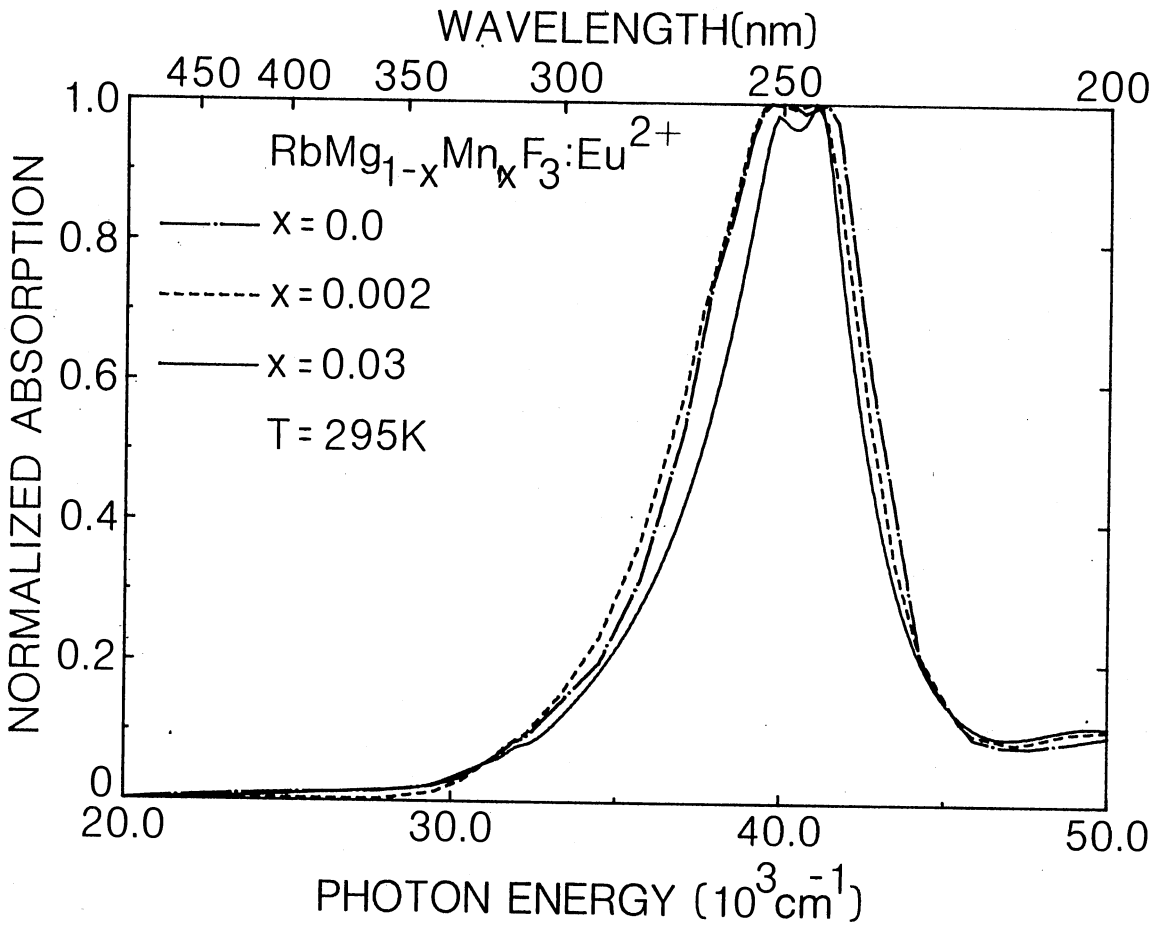

Figure 17. Normalized Absorption Spectrum of $RbMgF_3$:Eu, (dot-dashed line), $RbMgF_3$:Eu,$Mn_{0.002}$ (dashed line), and $RbMgF_3$:Eu,$Mn_{0.03}$ (solid line)

ness had to be reduced below 0.5mm. This is a result of the high oscillator strength ($f \simeq 0.01$) of the f-d transition (91). The maximum absorption coefficient of this band varied from sample to sample and was in the range 150-300 cm^{-1}. This corresponds to an estimated Eu^{2+} concentration of 0.15 to 0.3at.% (91). The weak absorption line at 31955 cm^{-1} (312.9nm) present in all samples, including those with no Mn^{2+} has not been reported previously. This may be one of the transitions $^4f^7(^8S_{7/2}) \rightarrow {}^4f^6(^7F_J)5d^1$ (J=0-6) which has often been reported earlier for other types of Eu^{2+}-doped crystals, and gives the lower-energy band a characteristic "staircase structure" (92). Weak bands due to absorption from the Mn^{2+} $^6A_{1g}$ ground state to excited states up to the $^4T_{2g}{}^2$ level (the Mn^{2+} ion resides in sites of C_{3v} symmetry, but for simplicity O_h symmetry assignments of the Mn^{2+} levels will be used) were also detected in the absorption spectrum of the $RbMg_{0.84}Mn_{0.15}F_3$:Eu samples. The assignments of these bands have been made previously (10). The oscillator strength of the $^4T_{1g}$ band at about 19050 cm^{-1} (525nm) is almost constant in similar hosts (93,94). Using the appropriate form of Smakula's equation (95)

$$fN = 7.23 \times 10^{15} \alpha_m W \qquad (39)$$

with α_m=0.1 cm^{-1}, W=0.186eV, and $f=3.5\times10^{-7}$, the Mn^{2+} concentration was determined to be 3.8×10^{20} cm^{-3}

(3.1at.%). This crystal will be designated the $Mn_{0.03}$ specimen. The Mn^{2+} concentration of the $RbMg_{0.98}Mn_{0.01}F_3$:$Eu_{0.01}$ samples was too low to be determined from absorption measurements. Instead, the ratio of the excitation peak intensity of the $^4T_{1g}$ band for the $RbMg_{0.98}Mn_{0.01}F_3$:Eu and $Mn_{0.03}$ samples, was used to determine that the $RbMg_{0.98}Mn_{0.01}F_3$:Eu specimens contained approximately $2.8x10^{19}$ cm^{-3} (0.2at.%) Mn^{2+}. This value is consistent with previous mass spectrographic analyses of $RbMgF_3$:Mn crystals with the same starting concentration of Mn^{2+}. It is also consistent with the concentration found from statistically-produced F-center-Mn^{2+} pairs, which implies that the Mn^{2+} ions are randomly distributed in the samples (8,14,96). This crystal will be referred to as the $Mn_{0.002}$ crystal.

The emission spectra of the $Mn_{0.002}$ and $Mn_{0.03}$ samples at room temperature are portrayed in Figs. 18(a) and 18(b). The line emission at approximately 27780 cm^{-1} (360 nm) and the band emission peaking at 24690 cm^{-1} (405 nm) are due to Eu^{2+} f-f and d-f transitions, respectively. The previously reported band emission at 19050 cm^{-1} (525 nm) is also present for excitation wavelengths between 330 and 400 nm (15). The broad emission band around 600 nm arises from the Mn^{2+} transition $^4T_{1g} \rightarrow {}^6A_{1g}$. The Mn^{2+} emission band peaks at 17095 cm^{-1} (585 nm) and 16450 cm^{-1} (608 nm) for the $Mn_{0.002}$ and $Mn_{0.03}$ crystals, respectively. The emission is present

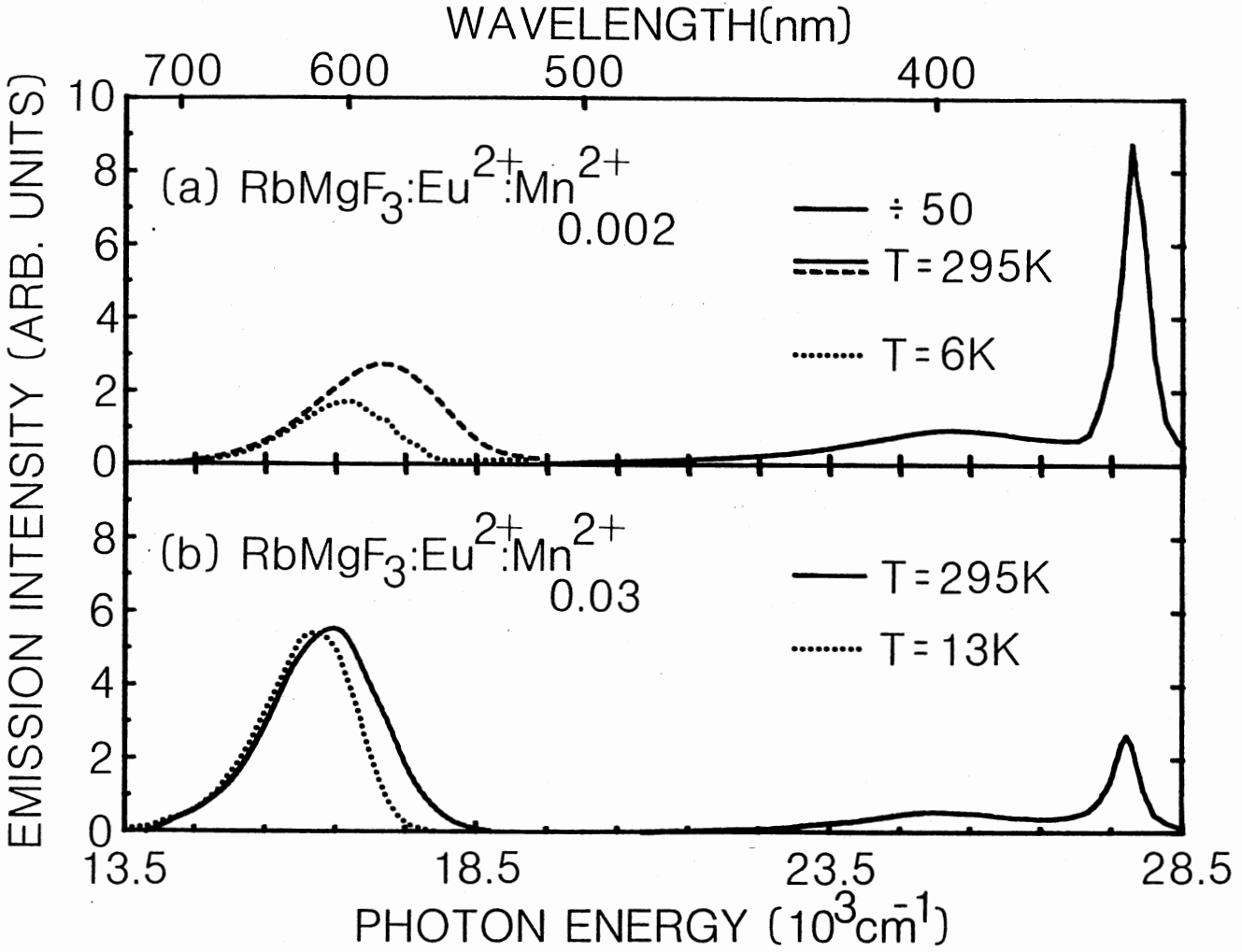

Figure 18. Emission Spectrum of (a) $RbMgF_3:Eu,Mn_{0.002}$ and (b) $RbMgF_3:Eu,Mn_{0.03}$

from 7K to 500K, but the peak position and width are temperature dependent, as is also shown in Fig. 18. The room temperature high resolution emission spectra of the Eu^{2+} f-f transitions for the two types of samples are similar to those reported earlier (15). There are lines around 28289 cm^{-1} (353.5 nm) which are present in all samples. The intensity of these lines is much weaker than the intensity of the ~359 nm line emissions, and decreases as the temperature decreases. The peak energy and behavior of these emissions are consistent with the previously observed Eu^{2+} transitions $^6P_{5/2} \rightarrow {}^8S_{7/2}$, which have been thermally populated by the $^6P_{7/2}$ level (97).

The low-temperature, high-resolution emission specra for the f-f transitions of $RbMgF_3$:Eu, and the $Mn_{0.002}$ and $Mn_{0.03}$ samples are presented in Figs. 19(a)-(c), respectively. The similarity between the $RbMgF_3$:Eu and $Mn_{0.002}$ sample's spectra should be noted. In contrast the $Mn_{0.03}$ sample's spectrum has a weaker line at 27682 cm^{-1} (361.25 nm) and a stronger line at 27793 cm^{-1} (359.8 nm). As was previously noted (15), the relative intensities of these lines change slightly for different samples, although the line at 27847 cm^{-1} (359.1 nm) is always one of the most intense lines.

Because of the small splitting (<0.2 cm^{-1}) of the ground state (15,99,100) each $^6P_{7/2} \rightarrow {}^8S_{7/2}$ transition of an Eu^{2+} ion in a noncubic site can give rise to no more than four emission lines (35,97,101). At 15K ($kT \simeq 10$ cm^{-1})

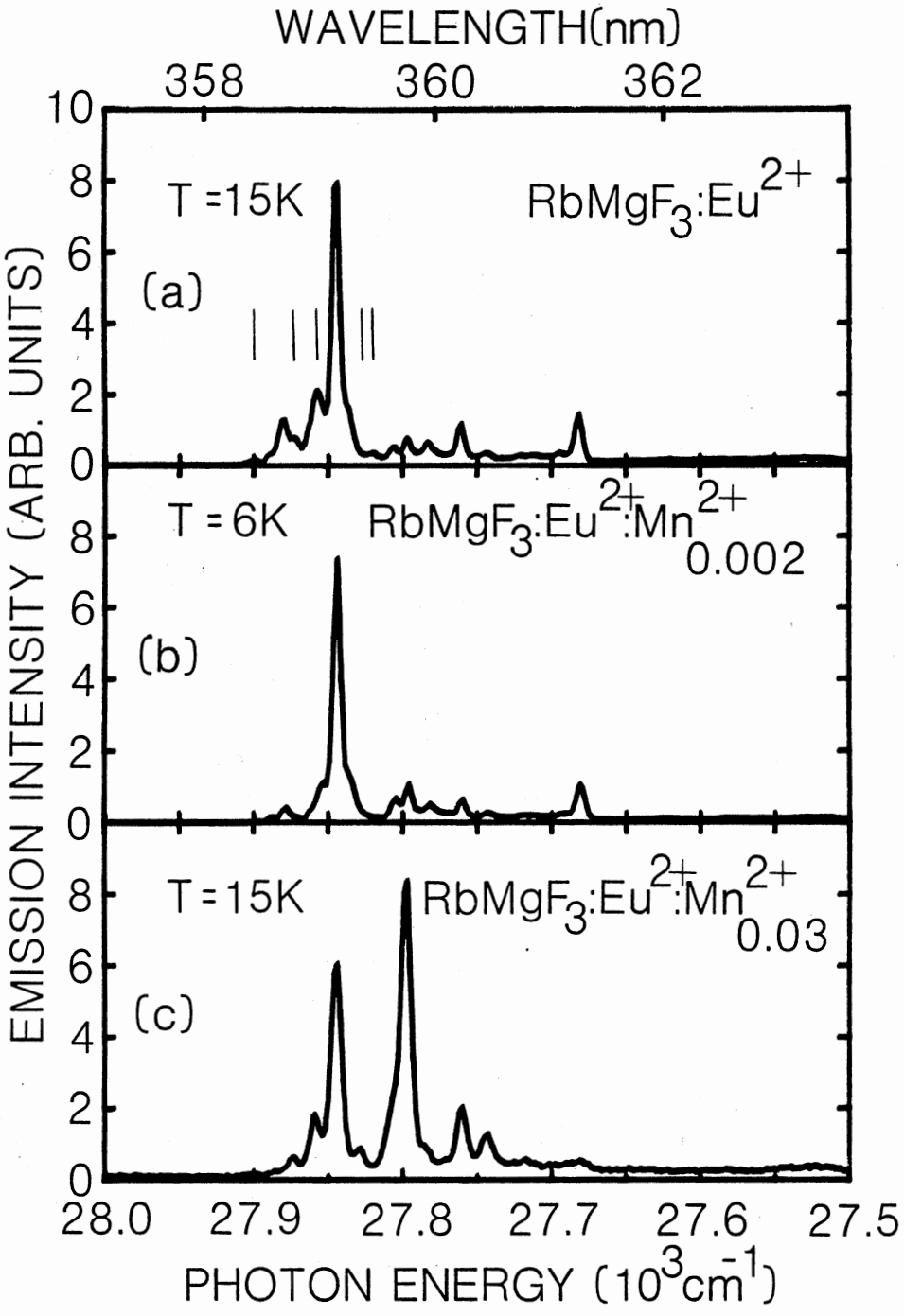

Figure 19. Low-Temperature Eu^{2+} Emission Spectrum of (a) $RbMgF_3$:Eu (b) $RbMgF_3$:Eu,$Mn_{0.002}$ and (c) $RbMgF_3$:Eu,$Mn_{0.03}$

appreciable thermalization of all four levels is not likely. Nevertheless, inspection of Figs. 19(a) and 19(b) reveals at least 12 lines. The temperature dependence of the lines can help determine how many of these lines arise from ions in different sites. As the temperature is increased, five emission lines, whose positions are indicated in Fig. 19(a) by vertical lines, increase in intensity. The change in intensity of these lines at 15, 20, 30, and 40K was fitted by the Boltzmann equation

$$n = n_o \exp(-\Delta E/kT) \tag{40}$$

This analysis suggests that the three highest energy lines are due to thermalization of the 27847 cm^{-1} (359.1 nm) line. This analysis yields multiplet splittings of 14, 28, and 59 cm^{-1}. The other two lines, at 27828 cm^{-1} (359.36 nm) and 27813 cm^{-1} (359.55 nm) are due to thermalization of the levels at 27781 cm^{-1} (359.96 nm) and 27759 cm^{-1} (360.25 nm), respectively. The splittings are 47 cm^{-1} and 54 cm^{-1}. The lower-lying sublevels in these multiplets are obscured by the other transitions. These other emissions decrease at varying rates as the temperature is raised and the 361.25 nm emission is totally quenched by 40K.

Since the excitation spectra of all emissions from a given submultiplet will be identical, the spectra of the more resolved lines in Fig. 19 were measured. The spectra for these lines all differed and in general tended to peak at lower energies as the emission energy decreases. This

was particularly noticaable for the transitions at 360.5 nm and 361.25 nm.

The luminescence decays of the lines portrated in Fig. 19 are listed in Table 5. At this temperature most of the decay curves were not single exponential. The values listed are the first e^{-1} times. The error in these measurements is about 10%. the deviation from single exponential behavior becomes larger as the energy of the transition decreases.

The temperature dependence of the 359.1 nm transition lifetimes for all three crystals is depicted in Fig. 20. The lifetime of the Eu^{2+} band emission at 405 nm was measured at 78K with the assistance of G.E. Venikouas. The lifetime of this transition in the $Mn_{0.002}$ samples was found to be approximately 1.6 μs, comparable to the room temperature value (15). The e^{-1} time of the band in the $Mn_{0.03}$ samples was found to be approximately 0.75 μs. The decay was highly nonexponential with a third e^{-1} time of 1.3 μs.

The 295K excitation spectra of the Mn^{2+} emission at 600nm for both Mn^{2+}-doped samples are illustrated in Figs. 21(a) and 21(b), respectively. The highest energy band is due to the Eu^{2+} f-d transition, while the lower energy bands arise from Mn^{2+} transitions (10).

The response of the Mn^{2+} luminescence after excitation differs for the $Mn_{0.002}$ and $Mn_{0.03}$ samples. The temperature dependence of the decay times is shown in

TABLE V

LIFETIMES OF Eu^{2+} TRANSITIONS IN $RbMgF_3$ AND $RbMgF_3$:Mn AT 14K (IN ms)

WAVELENGTH (nm)	ENERGY (cm^{-1})	$RbMgF_3$	$RbMgF_3$:Eu,Mn ($Mn_{0.002}$)	$RbMgF_3$:Eu,Mn ($Mn_{0.03}$)
358.4	27902		3.10	
358.9	27863	2.41	2.44	
359.1	27847	1.84	1.88	1.23
359.8	27793	2.18	1.84	1.43
360.25	27759	1.18	1.16	1.05
360.5	27739	0.048	0.05	
360.9	27709		1.02	
361.25	27682	0.123	0.075	

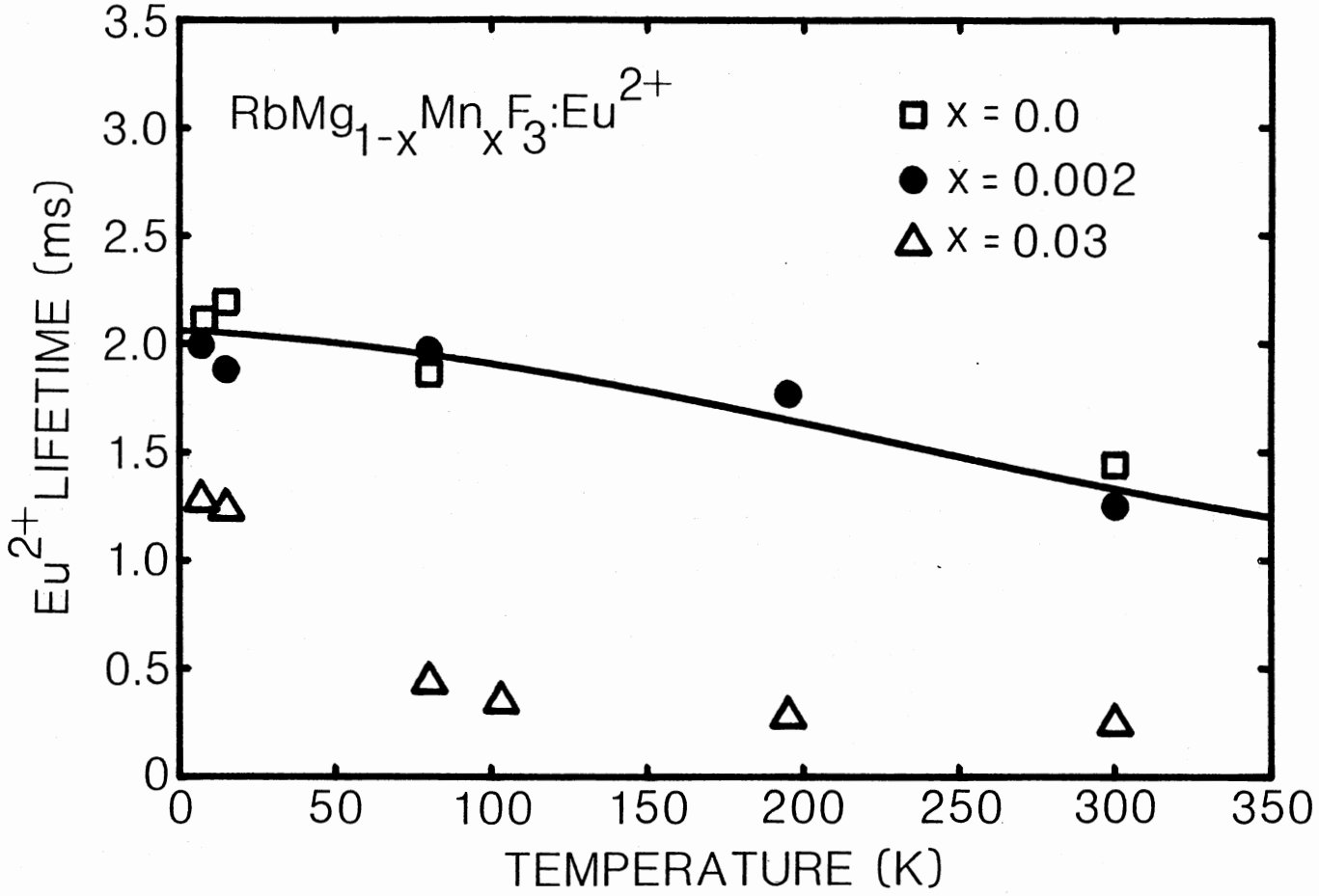

Figure 20. Temperature Dependence of the 359.1 nm Eu^{2+} Emission Lifetime in $RbMgF_3$:Eu (squares), $RbMgF_3$:Eu,$Mn_{0.002}$ (circles) and $RbMgF_3$:Eu,$Mn_{0.03}$ (triangles)

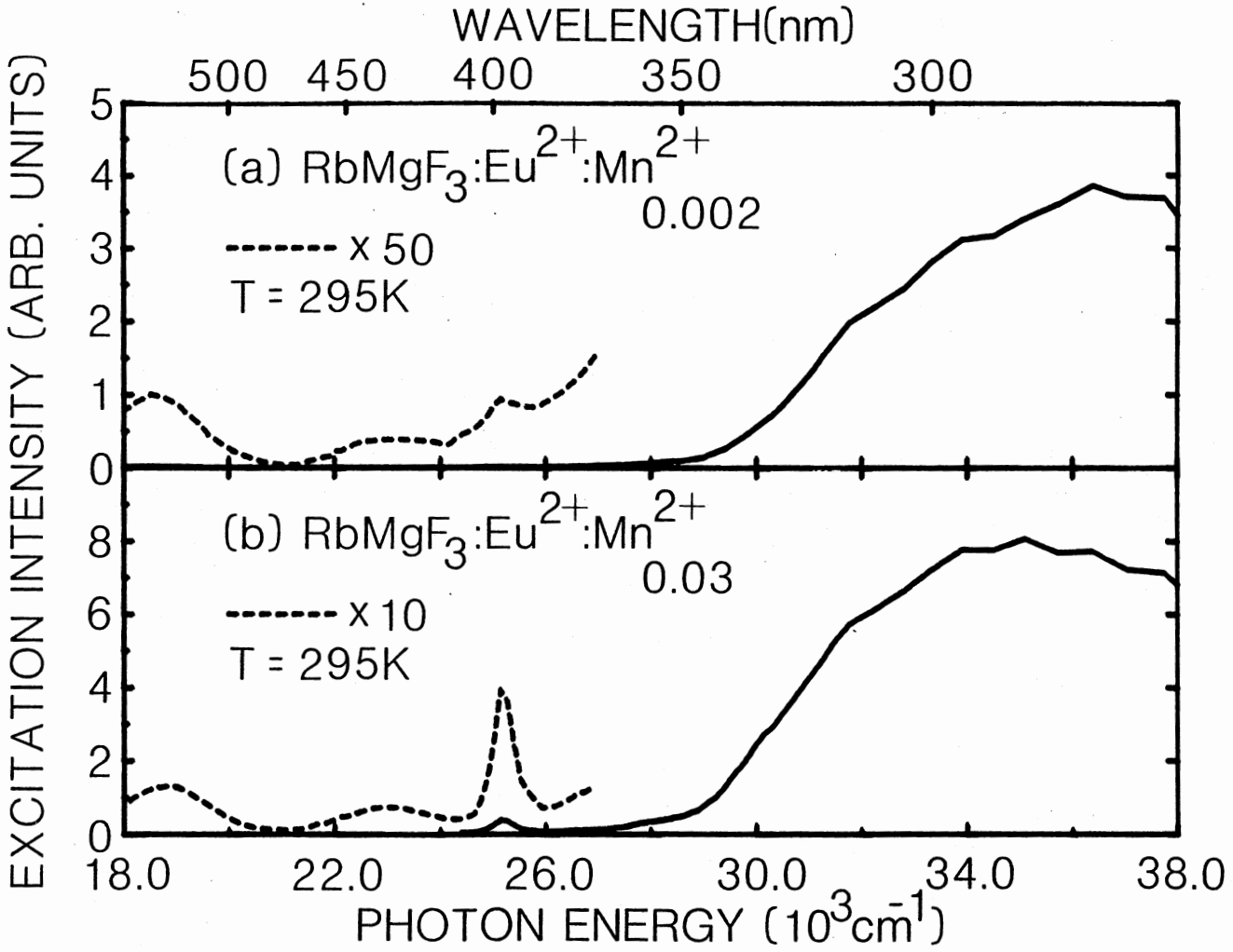

Figure 21. Excitation Spectrum of Mn^{2+} in (a) $RbMgF_3:Eu,Mn_{0.002}$ and (b) $RbMgF_3:Eu,Mn_{0.03}$

Fig. 22. The Mn^{2+} luminescence decay of the $Mn_{0.03}$ samples after excitation of the $^4T_{1g}$ level exhibited single exponential decay. Pulsed excitation of the Eu^{2+} band resulted in a large initial luminescence followed by a rise in intensity with a maximum intensity occurring at a time t_{max} = 780 μs. This value of t_{max} was temperature independent from 14 to 300K. The decay of the luminescence was nonexponential and had the same e^{-1} time as was measured by exciting the Mn^{2+} ions directly.
The decay became more exponential in behavior as the temperature was raised and was single exponential above 200K.

The decay of the Mn^{2+} luminescence in the $Mn_{0.002}$ samples after excitation of the $^4T_{1g}$ level was the sum of two exponentials. The faster decay, denoted by solid circles in Fig. 22, had a temperature independent lifetime of ~25 ms. The slower decay, denoted by open circles, had a lifetime of ~120 ms for temperatures below 200K and decreased to 87 ms at 300K. Pulse excitation of the Eu^{2+} band resulted in no measurable risetime of the Mn^{2+} luminescence. The luminescence decayed in the same way as for direct excitation of the Mn^{2+} ions.

An interesting new effect was found for the $Mn_{0.002}$ samples. After chopper excitation of the Eu^{2+} band, the decay constants were the same as reported for the directly excited Mn^{2+} ions. However, the contribution of the longer lifetime decay to the total intensity of the decay was

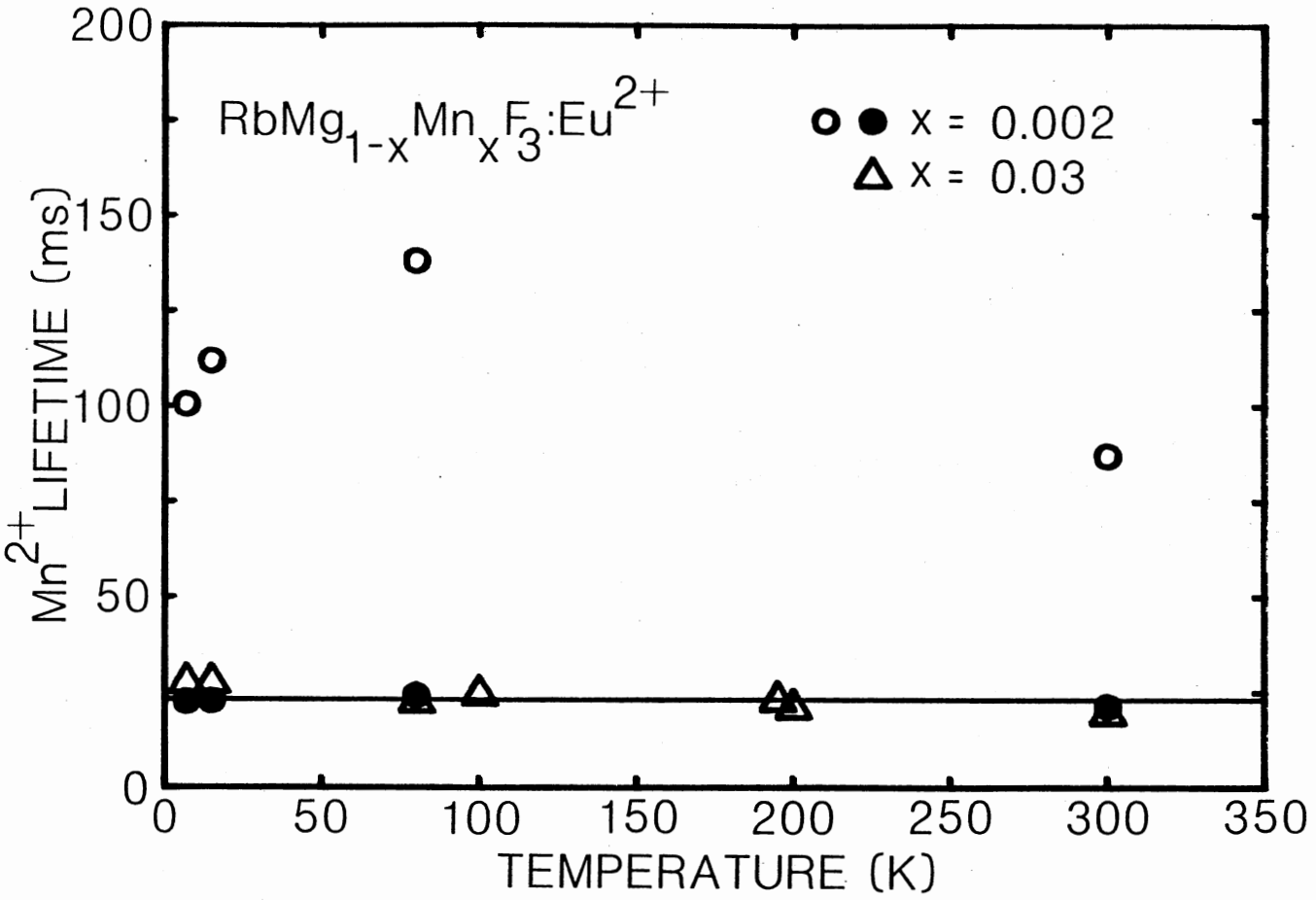

Figure 22. Temperature Dependence of the Mn^{2+} Lifetime in $RbMgF_3:Eu,Mn_{0.002}$ (circles) and $RbMgF_3:Eu,Mn_{0.03}$ (triangles)

much larger for the Mn^{2+} ions following Eu^{2+}-excitation than for the directly-excited Mn^{2+} ions. To investigate this effect the change in the ratio of the initial intensity of the longer lifetime to the total intensity as a function of pulsewidth (accomplished by masking the chopper aperture) was measured at 295K and plotted in Fig. 23. The data indicate that the ratio remains essentially constant below pulsewidths of 5 ms and then increases, becoming constant again for pulsewidths greater than ~200 ms.

ZBLA:Er

The data presented in this section represent the most complete study of the optical properties of a rare earth ion in fluorozirconate glass to date. Having studied the optical properties of rare earth ions in $LiYF_4$ (85) and $RbMgF_3$ (13-15,17), our laboratory had the instumentation and techniques necessary to make a thorough study of this particular ion-host combination. Nevertheless, this study represents a departure from dealing only in crystalline solids for our group. Yet, it allows us to continue working in a fluoride host, even though it is amorphous

Before presenting the data, it is important to emphasize the difference between glasses and crystals, insofar as the optical properties of impurity ions incorporated in them is concerned.

In glass, impurity ions occupy nonequivalent sites

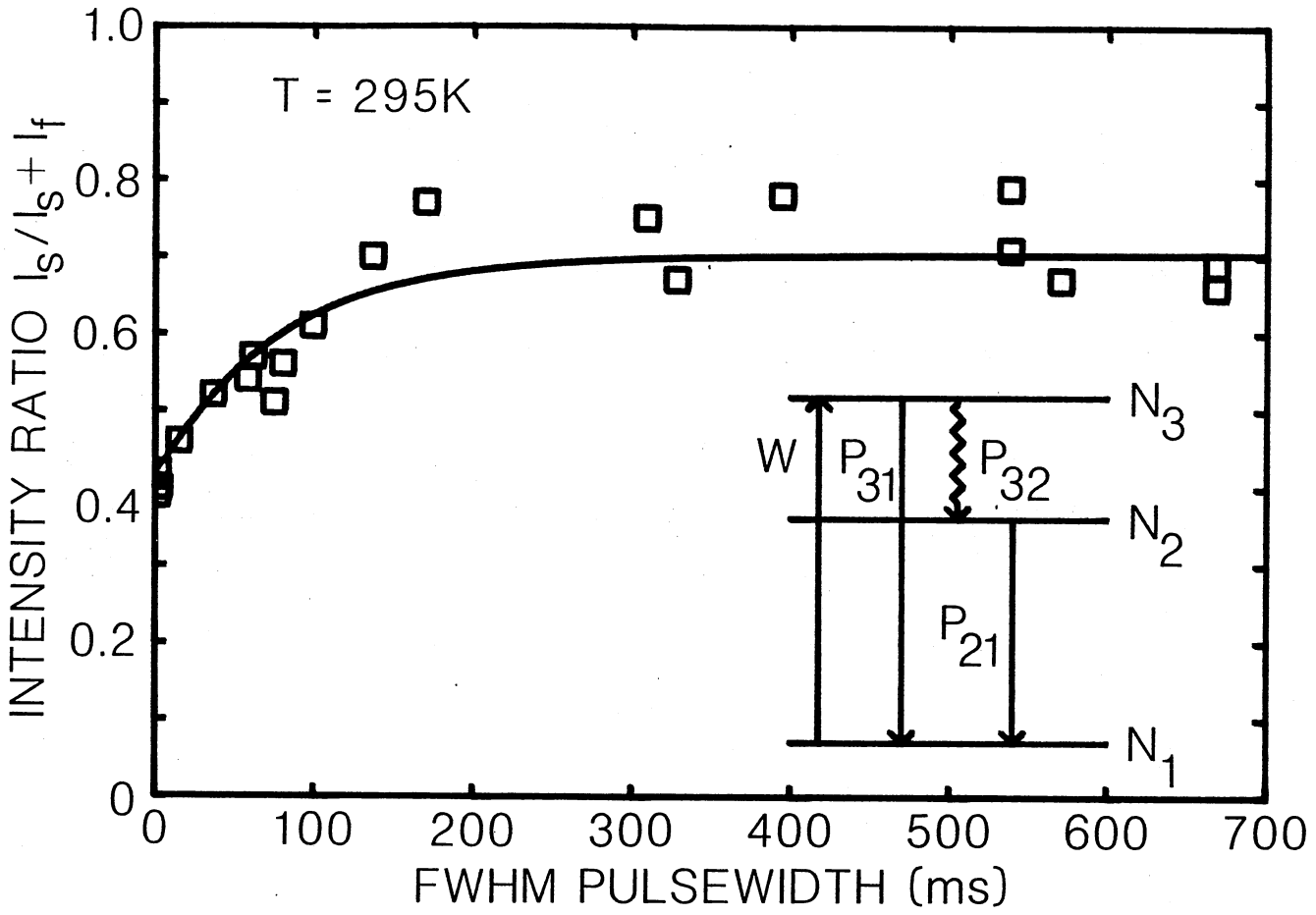

Figure 23. Intensity Ratio of the Long Lifetime Decay to the Total Decay of the Mn^{2+} Emission Immediately After Excitation (λ_{ex}=318 nm) Versus the FWHM Pulsewidth of the Excitation for $RbMgF_3Eu,Mn_{0.002}$

which result from varying crystal-field strengths and symmetries. From the information presented in the Theory section, this site-to-site variation will cause variations in the Stark splitting of the multiplets, resulting in inhomogeneously broadened optical absorption and emission lines. It will also cause variations in the radiative rate, resulting in nonexponential fluorescence decays. Our excitation sources are broadband (resolution limited to 1 nm) which results in optical properties which are the sum of the properties of the individual ions which are in various sites within the glass.

Recall that two samples of ZBLA:Er glass with concentrations of 0.5at.% and 2.0at.% Er^{3+}, were prepared. The absorption spectrum of the 2.0at.% Er^{3+} sample is shown in Fig. 24(a), with the $^4I_{13/2} \rightarrow {}^4I_{15/2}$ excitation spectrum shown in Fig. 24(b) for comparison. Excitation bands of higher energy than those shown were observed, however, their low intensity with respect to the noise made it impossible to accurately correct the intensities. The absorption coefficients of the 0.5at.% Er^{3+} sample were only one-fourth as large as the absorption coefficients of the 2.0at.% Er^{3+} sample, except for the band at 12500 cm^{-1} (800 nm) which was more intense. This sample's absorption spectrum also contained weak bands at 13514 cm^{-1} (740 nm) and 17361 cm^{-1} (576 nm). Comparison with earlier work on Nd^{3+} in ZBL glass (22) shows absorption bands at the same three positions. The

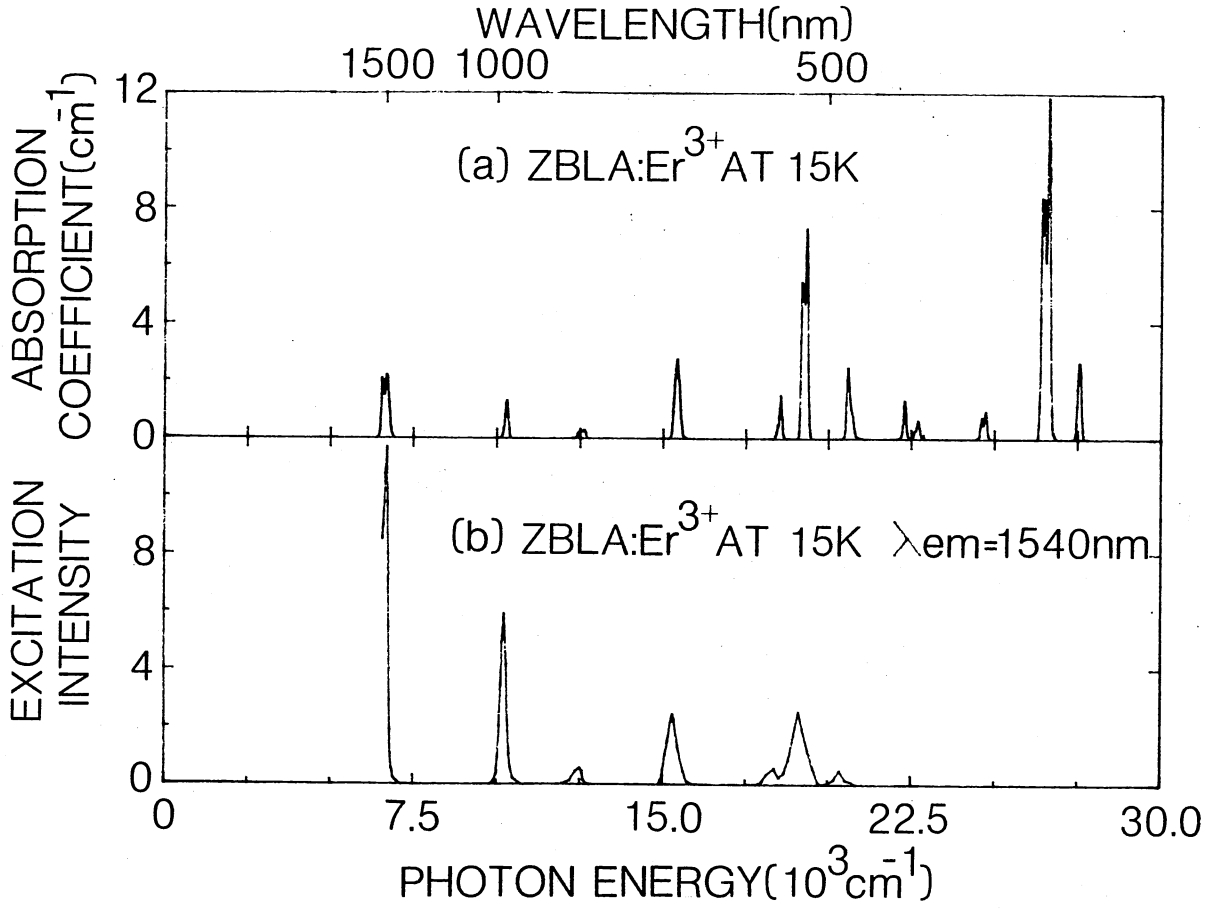

Figure 24. (a) Absorption Spectrum of Er^{3+} in ZBLA.
(b) $^{4}I_{13/2}$ Excitation Spectrum of Er^{3+} in ZBLA

concentration of Nd^{3+} in our sample was determined to be about 0.005at.% (8.2×10^{17} cm^{-3}) by comparing the intensities of the Nd^{3+} bands with those of ZBL:Nd (22). The emission spectra of Er^{3+} at 300 and 14K are shown in Figs. 25(a) and 25(b), respectively. In these figures the line marked with an asterisk is the transition $^4S_{3/2} \rightarrow {}^4I_{13/2}$, the line marked with a plus is the transition $^2H_{11/2} \rightarrow {}^4I_{13/2}$, the line marked with a circle is the transition $^2H_{9/2} \rightarrow {}^4I_{11/2}$, and the line marked with a double asterisk is the transition $^4S_{3/2} \rightarrow {}^4I_{9/2}$. All other transitions are from the excited states to the ground state. An energy-level diagram for ZBLA:Er, using the data presented in Figs. 24 and 25, is shown in Fig. 26. Included are the energy levels of the free ion (35), and the measured lifetimes at 14K.

The high-resolution emission spectrum of the $^4S_{3/2} \rightarrow {}^4I_{15/2}$ transition (solid line), which shows the extent of the ground-state splitting and inhomogeneous broadening, is presented in Fig. 27. Superimposed on this spectrum is the same emission of Er^{3+} from site 1 in $RbMgF_3$ (see Fig. 8). It is apparent that the ground-state splitting of Er^{3+} in this glass is no greater than in $RbMgF_3$ crystals. The data in Fig. 27 suggest that the types of site symmetries in ZBLA are fewer in number than in the oxide glasses, which exhibit broader emissions. This has been previously explained as being due to Er^{3+} substituting only as a network former, unlike the case for some oxide

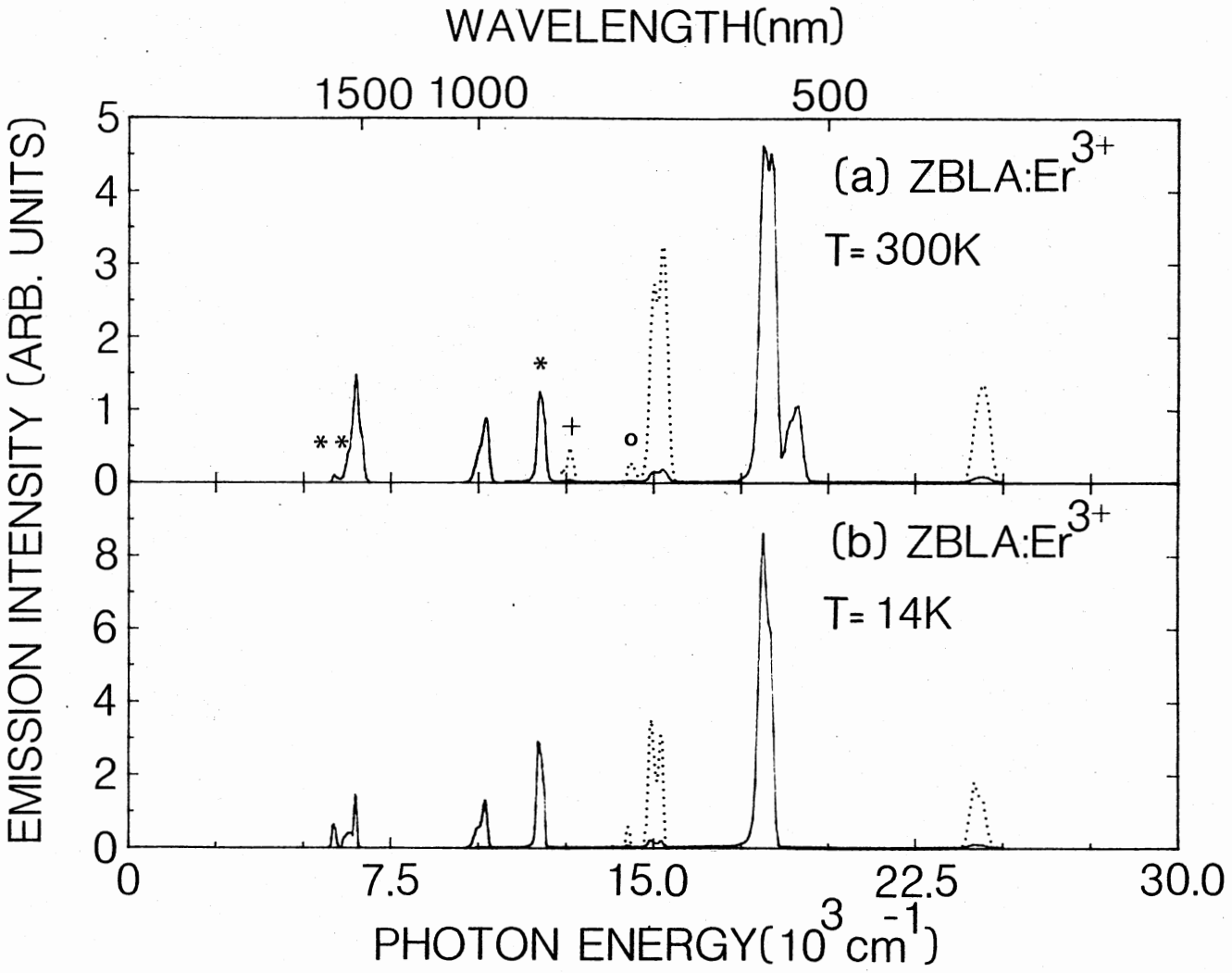

Figure 25. Emission Spectra of Er^{3+} in ZBLA at (a) 300K and (b) 14K

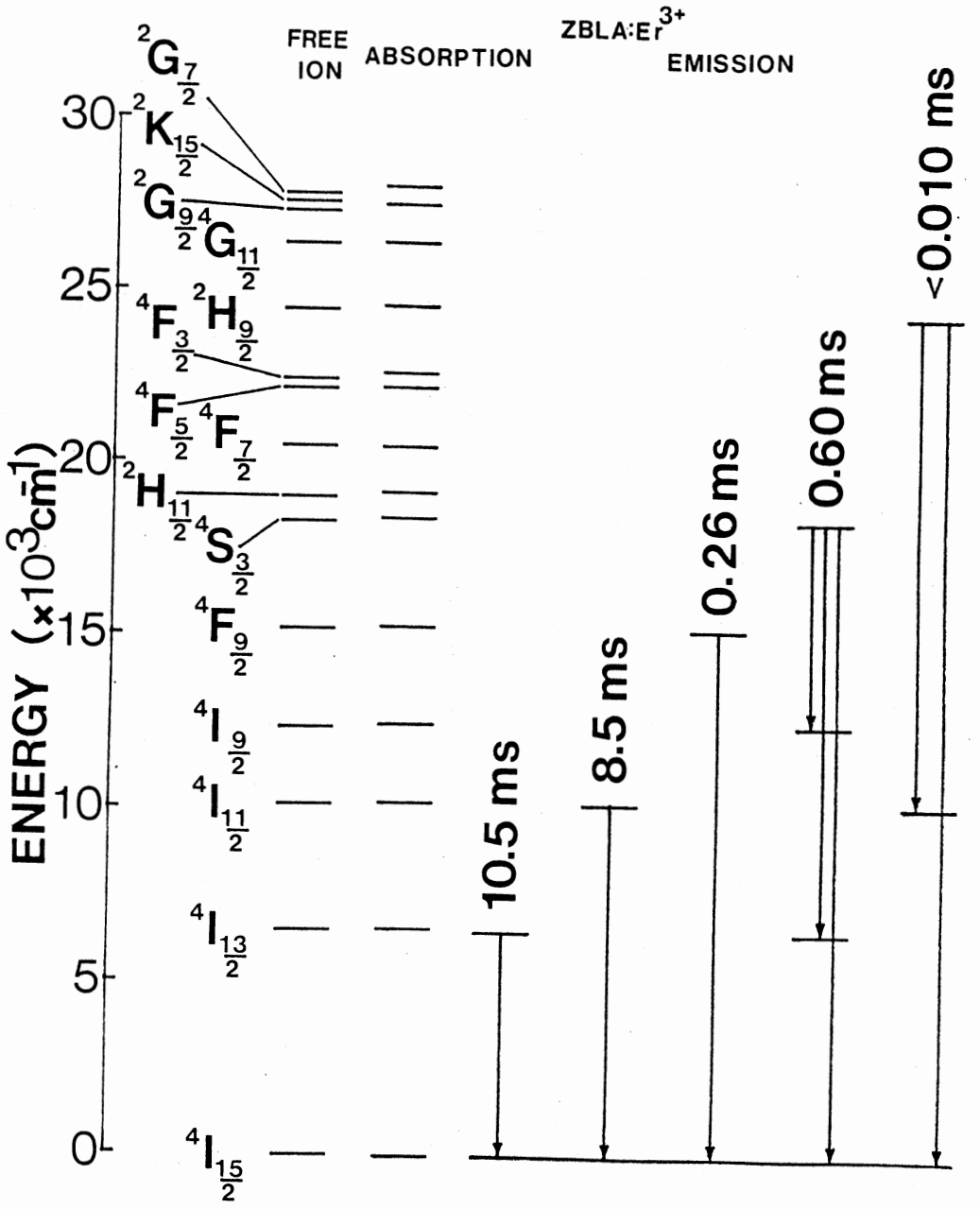

Figure 26. Energy-Level Diagram of Er^{3+} as a Free Ion (Ref. 35), and for the Present Work. Also Shown are the Lifetimes of the Fluorescence at 14k

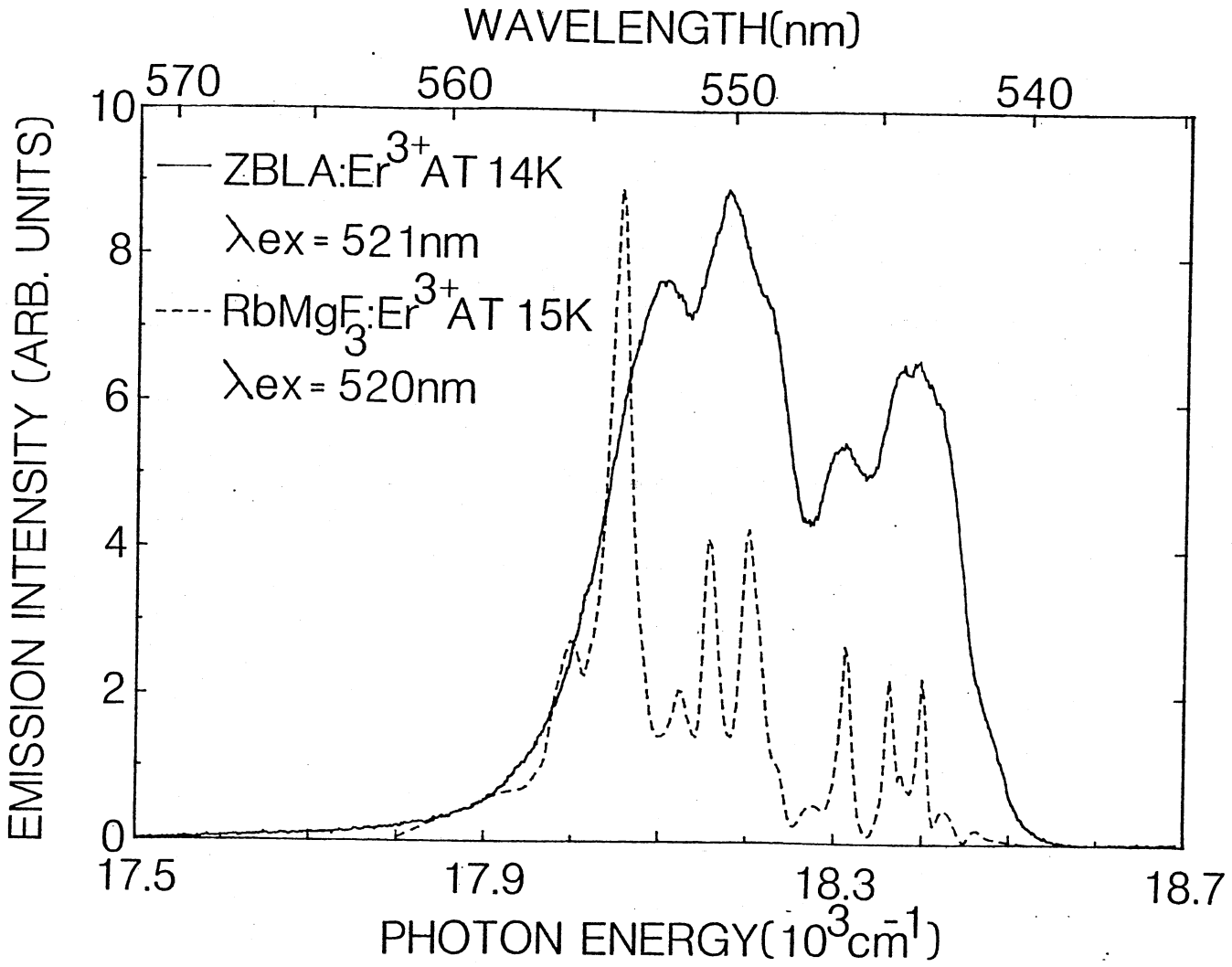

Figure 27. $^4S_{3/2} \rightarrow {}^4I_{15/2}$ Emission Spectrum of Er^{3+} in ZBLA (solid line), and $RbMgF_3$ (dotted line)

glasses, where Er^{3+} may substitute for both network formers and modifiers (22,24).

The oscillator strengths of the absorption transitions were calculated using Eq.(10). All transitions were assumed to be electric dipole in nature, except for the $^4I_{15/2} \rightarrow {}^4I_{13/2}$ transition, which has a substantial magnetic dipole component. The values for both glass samples are presented in Table 6. Values for Er^{3+} in several other hosts are shown for comparison. The value of N, the concentration, was taken to be equal to the concentration of the starting mixture. This has been found to be true for previous rare-earth dopings of fluoride glasses (22). The value of the $^4I_{9/2}$ oscillator strength for the 0.5at.% Er^{3+} sample was estimated by integrating the entire band and subtracting the contribution due to 0.005at.% Nd^{3+}. The index of refraction was measured at two wavelengths and the indices of refraction were calculated using Cauchy's equation $n = A + B/\lambda^2$, with A=1.50583 and B=3478.14 nm^2. The average frequencies of the transitions were taken to be the centers of gravity of the absorption bands. These values were substituted into Eqs.(9) and (14) and the Judd-Ofelt parameters adjusted to give the best least-squares fit to the measured oscillator strengths. For the $^4I_{13/2}$ absorption, the magnetic dipole oscillator strength was calculated and subtracted from the measured oscillator strength to give the electric dipole oscillator strength (25). The Judd-Ofelt parameters are

TABLE VI

MEASURED OSCILLATOR STRENGTHS OF Er^{3+} IN VARIOUS HOSTS ($\times 10^8$)

LEVEL		$YAlO_3$[60] 300K	Y_2O_3[55] 300K	PZGL[24] 300K	ZBLA:0.5% Er 300K	ZBLA:2.0% Er 300K	ZBLA:2.0% Er 15K
$^4I_{13/2}$	m.d.	59	52	201	46	46	46
	e.d.	68	73		125	103	131
$^4I_{11/2}$		31	34	67	49	56	52
$^4I_{9/2}$		25	31	32	25	20	21
$^4F_{9/2}$		115	173	176	180	164	175
$^4S_{3/2}$		41	34	41	33	39	47
$^2H_{11/2}$		243	1103	278	436	394	452
$^4F_{7/2}$		112	113	125	138	141	128
$^4F_{5/2}$		60	40	63	61	71	47
$^4F_{3/2}$				35			32
$^2H_{9/2}$		42	61	56	47	47	54
$^4G_{11/2}$		431	2055	581	778	841	875

$\Omega_2=2.54\times10^{-20}$ cm^2, $\Omega_4=1.39\times10^{-20}$ cm^2, and $\Omega_6=9.65\times10^{-21}$ cm^2. The calculated oscillator strengths are given in Table 7. A measure of the quality of the fit is given by the rms deviation between the measured and calculated oscillator strengths, as calculated from the relationship

$$\text{rms} = \left[\frac{\text{sum of squares of deviations}}{\text{number of transitions-number of parameters}}\right]^{1/2} \quad (41)$$

The rms deviation for the 0.5at.% Er^{3+} sample is 0.14×10^{-6}, which is comparable to the rms deviations found by applying the Judd-Ofelt theory to other systems (22,47,58). The radiative lifetimes of the excited states can be calculated from Eqs.(16) and (17). While forced electric dipole transitions comprise most of the spontaneous emission probabilities of any level, the magnetic dipole emission probabilities were also calculated for the $^4I_{13/2} \rightarrow {}^4I_{15/2}$, $^4I_{11/2} \rightarrow {}^4I_{13/2}$, and $^4I_{9/2} \rightarrow {}^4I_{11/2}$ transitions. The values obtained are shown in Table 8.

The temperature dependences of the lifetimes of both samples are shown in Figs. 28-31. Although fluorescence was detected from the $^2H_{9/2}$ level, the lifetime was faster than could be measured with our system. The errors in

TABLE VII

CALCULATED OSCILLATOR STRENGTHS OF Er^{3+} IN ZBLA GLASS ($\times 10^8$)

LEVEL	WAVELENGTH(nm)	OSCILLATOR STRENGTH	RESIDUAL
$^4I_{13/2}$	1516	97.6	28
$^4I_{11/2}$	976	42.2	7
$^4I_{9/2}$	800	23.9	-1
$^4F_{9/2}$	653	173.7	6
$^4S_{3/2}$	542	37.4	-5
$^2H_{11/2}$	521	432.0	4
$^4F_{7/2}$	487	153.2	-15
$^4F_{5/2}, ^4F_{3/2}$	448	68.4	-7
$^2H_{9/2}$	406	62.2	-15
$^4G_{11/2}$	378	780.4	-2

TABLE VIII

PREDICTED SPONTANEOUS EMISSION PROBABILITIES OF Er^{3+} IN ZBLA GLASS

TRANSITION	AVERAGE FREQUENCY(cm^{-1})	$P_{e.d.}(s^{-1})$	$P_{m.d.}(s^{-1})$	τ_R(ms)
$^4I_{13/2} \rightarrow {}^4I_{15/2}$	6596	73.5	34.7	9.2
$^4I_{11/2} \rightarrow {}^4I_{15/2}$	10246	89.9		9.2
$^4I_{13/2}$	3650	10.9	7.7	
$^4I_{9/2} \rightarrow {}^4I_{15/2}$	12500	90.6		8.3
$^4I_{13/2}$	5904	28.9		
$^4I_{11/2}$	2254		1.1	
$^4F_{9/2} \rightarrow {}^4I_{15/2}$	15314	994.4		0.92
$^4I_{13/2}$	8718	48.6		
$^4I_{11/2}$	5068	40.9		
$^4I_{9/2}$	2814	1.3		
$^4S_{3/2} \rightarrow {}^4I_{15/2}$	18450	782.3		0.86
$^4I_{13/2}$	11854	316.1		
$^4I_{11/2}$	8204	25.4		
$^4I_{9/2}$	5950	41.5		
$^2H_{11/2} \rightarrow {}^4I_{15/2}$	19194	3264.4		0.31
$^2H_{9/2} \rightarrow {}^4I_{15/2}$	24631	937.6		0.44
$^4I_{13/2}$	18034	1010.1		
$^4I_{11/2}$	14385	302.4		
$^4I_{9/2}$	12131	11.9		
$^4F_{9/2}$	9317	23.1		

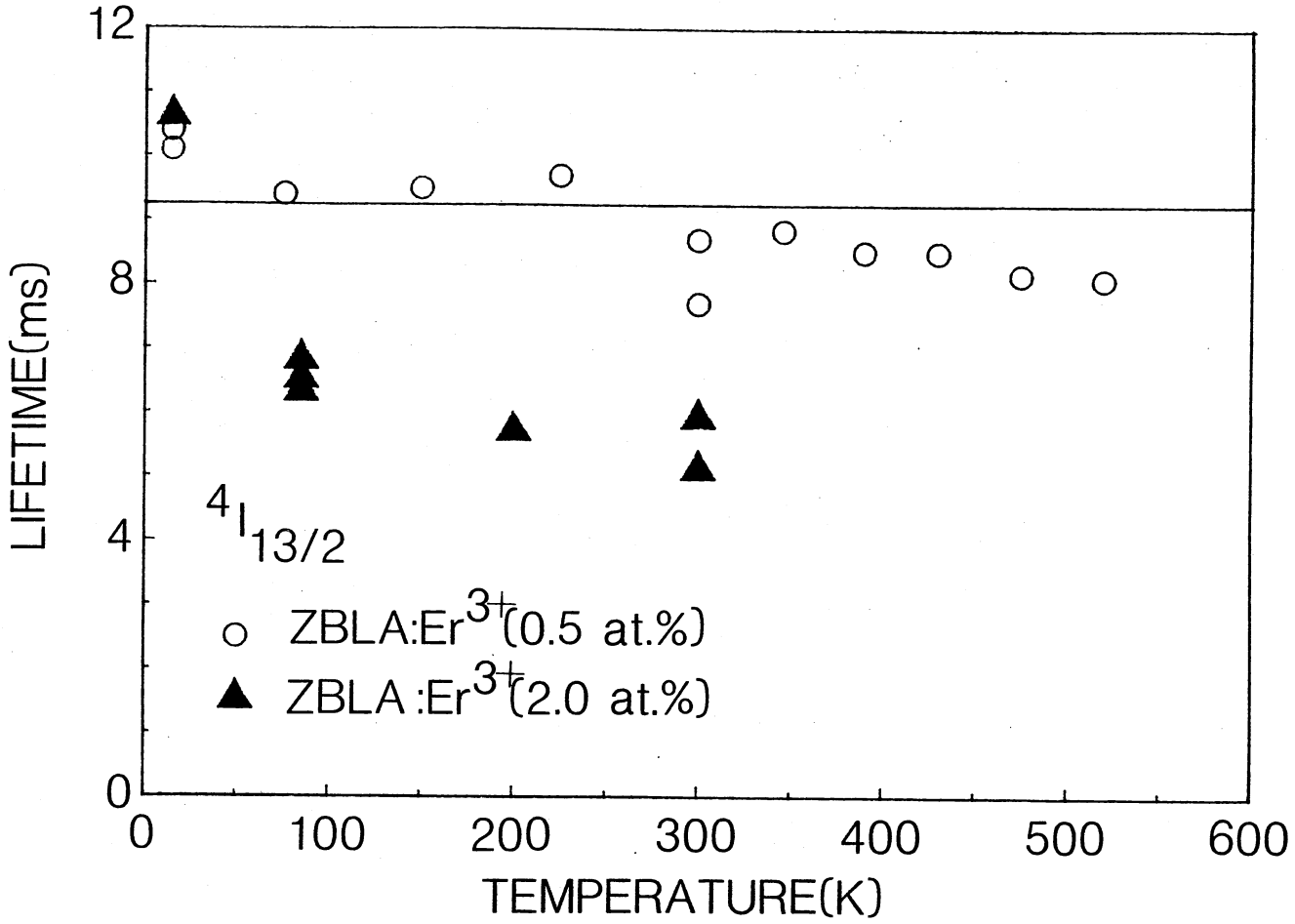

Figure 28. Temperature Dependence of the $^4I_{13/2}$ Emission Lifetimes

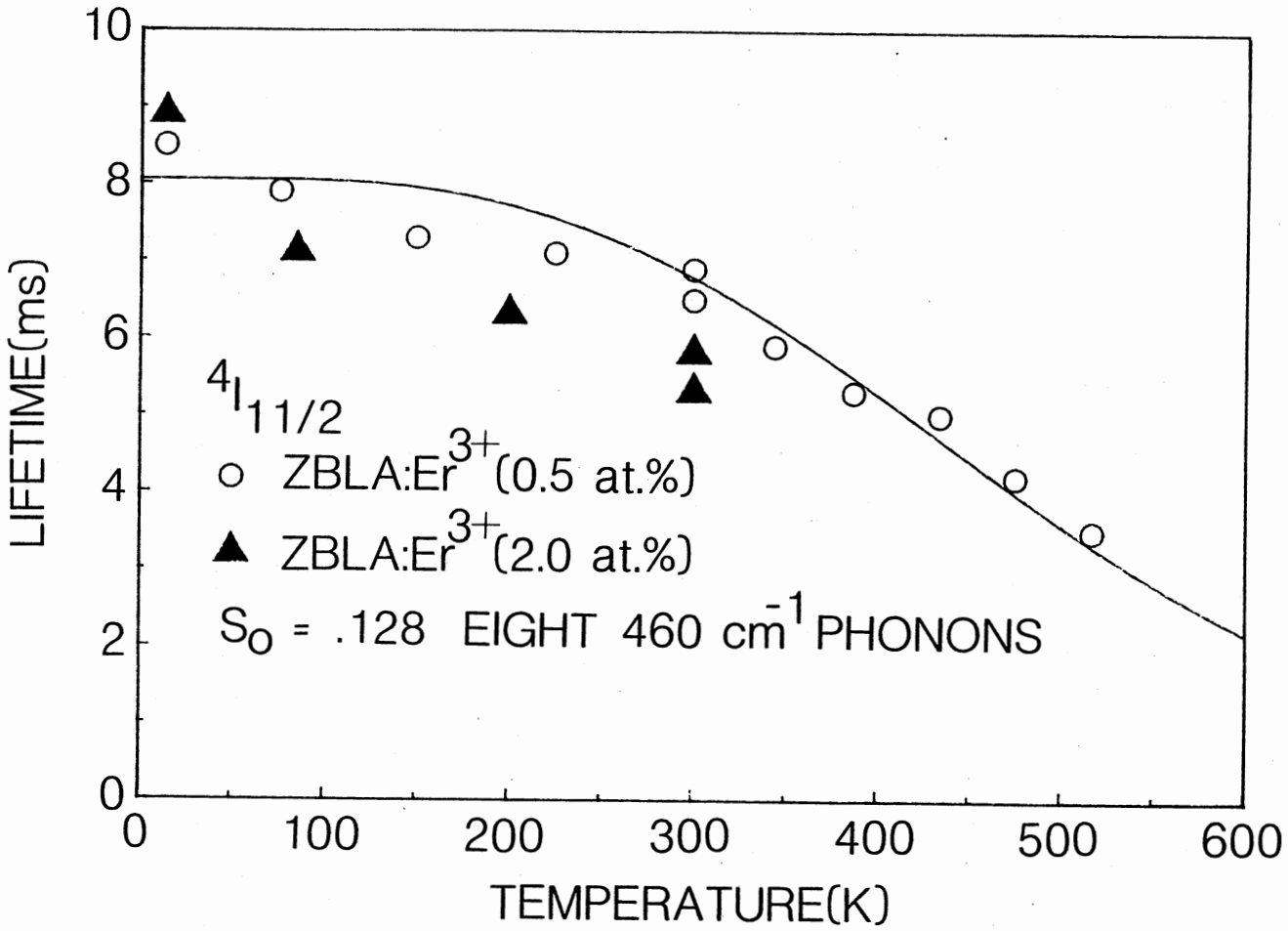

Figure 29. Temperature Dependence of the $^4I_{11/2}$ Emission Lifetimes

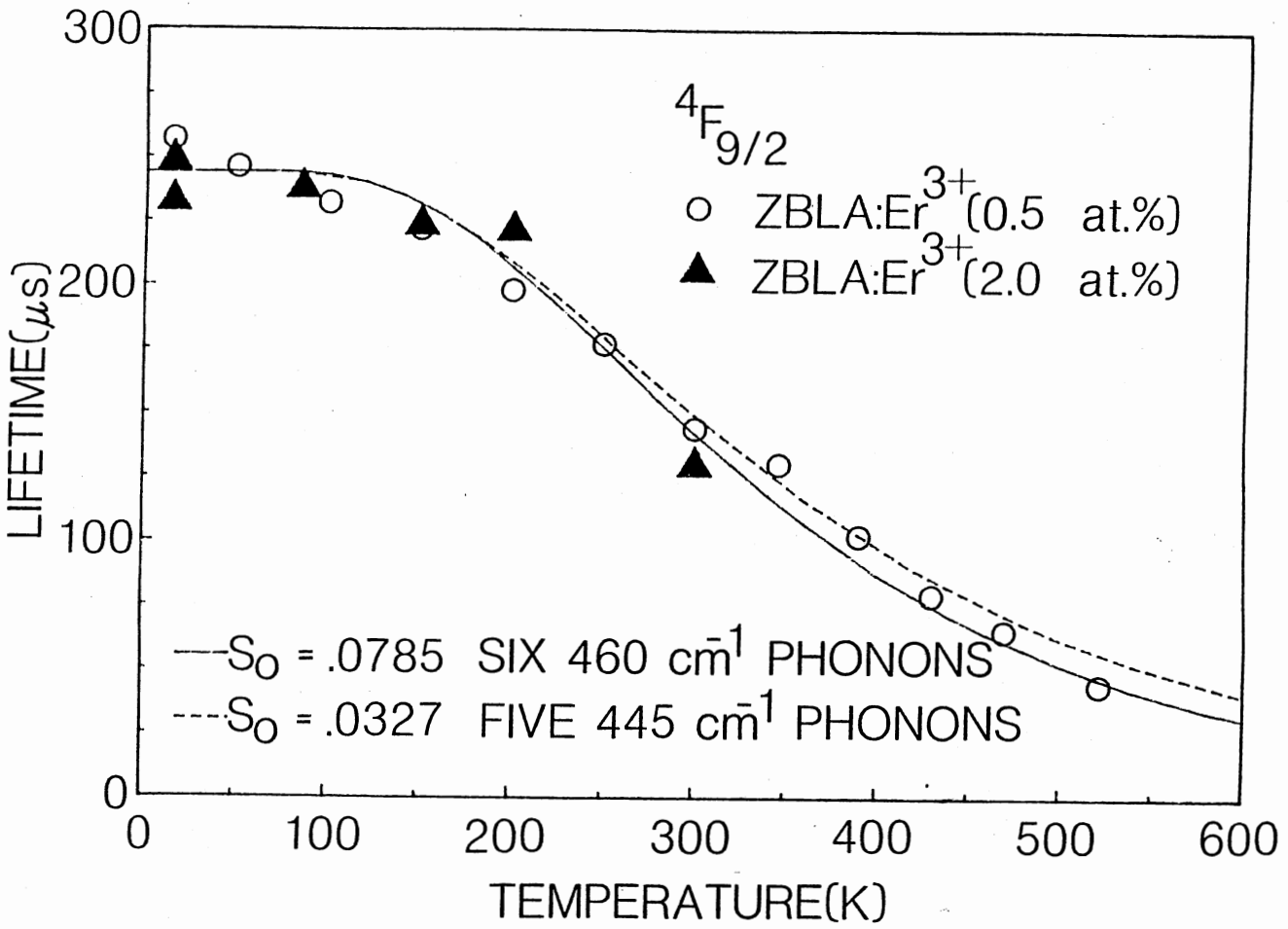

Figure 30. Temperature Dependence of the $^4F_{9/2}$ Emission Lifetimes

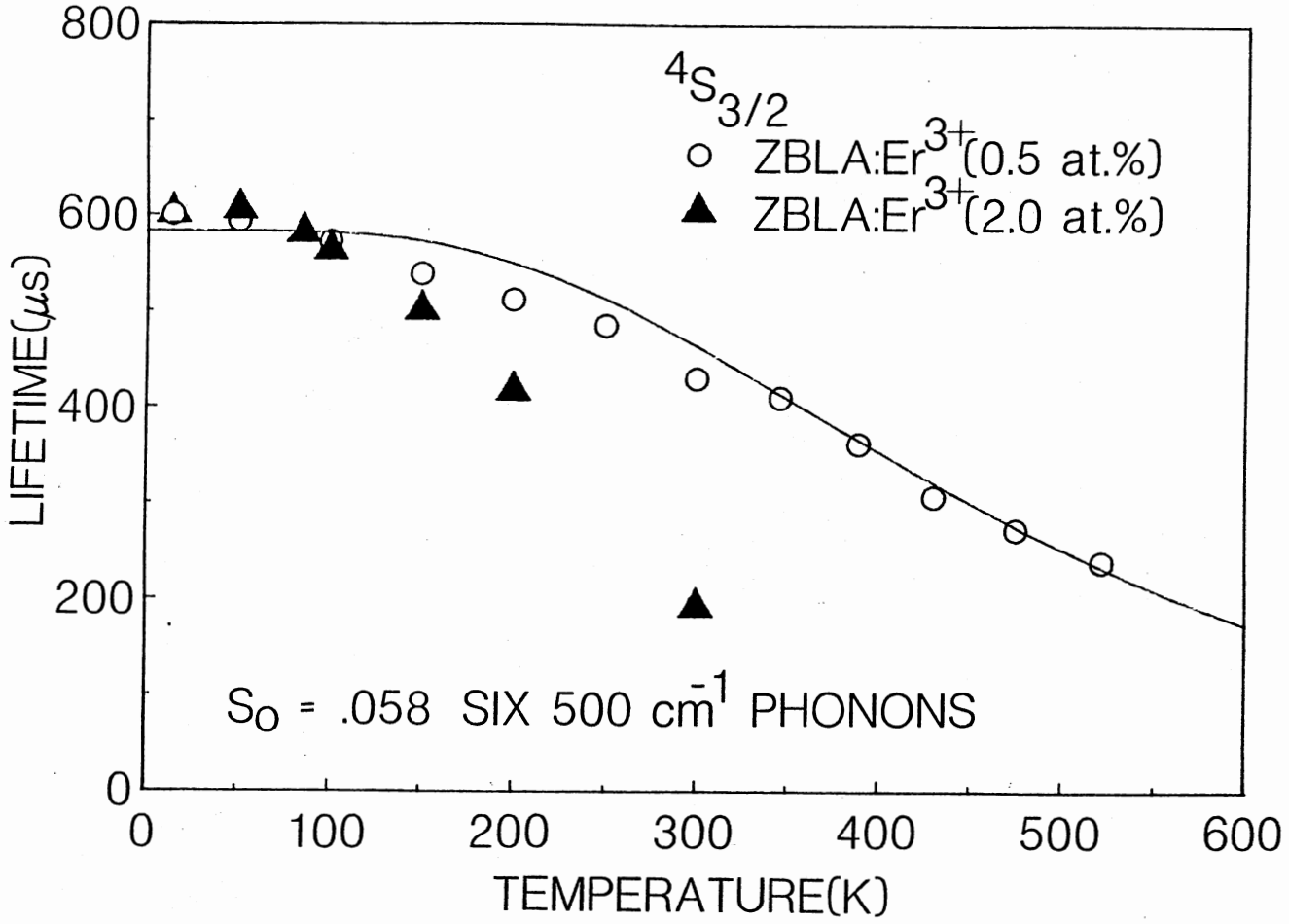

Figure 31. Temperature Dependence of the $^4S_{3/2}$ Emission Lifetimes

these measurements are estimated to be 5%. The decays of the $^4I_{13/2}$ and $^4I_{11/2}$ levels could be fitted to a single exponential, while the $^4S_{3/2}$ and $^4F_{9/2}$ levels were very nearly single exponential, with a ratio between the first and third e-folding times of these two levels of > 85%. For these levels the first e-folding times were used as the values of the lifetimes.

Comparison of Fig. 25(a) with Fig. 25(b) shows that the emission at 19120 cm^{-1} (523 nm) decreases in intensity as the temperature is lowered. The energy of the emission and its excitation spectrum identify this emission as the $^2H_{11/2} \rightarrow {}^4I_{15/2}$ transition which is populated thermally by the $^4S_{3/2}$ level. This behavior has been observed previously (56,102). An analysis based on a simple three-level system comprised of the $^2H_{11/2}$ (level 3), $^4S_{3/2}$ (level 2), and $^4I_{15/2}$ levels predicts that the thermalization can be expressed by the following equation

$$\frac{I_3}{I_2} = \frac{c_3(\nu)p_3^r g_3 h\nu_3}{c_2(\nu)p_2^r g_2 h\nu_2} \exp[\frac{-E_{32}}{kT}] \qquad (42)$$

where g_3, g_2 are the degeneracies (2J+1), and $p_3{}^r$ and $p_2{}^r$ are the total spontaneous emission rates of the $^2H_{11/2}$ and $^4S_{3/2}$ levels, respectively. The response of the detection system in the frequency range of the $^2H_{11/2}$ and $^4S_{3/2}$ levels is given by $c_3(\nu)$ and $c_2(\nu)$, respectively. The phonon energies of the two bands are so similar that they are considered equal. This relation was checked by re-

cording the two emission spectra at various temperatures and plotting the ratio of the intensities versus 1000/T, as shown in Fig. 32. The line is a least-squares fit to the data, and it can be seen that a good fit to Eq.(42) is obtained. The value of the preexponential factor can be estimated from the product of the ratio of the degeneracies (3), the ratio of the radiative rates (~2.8), and the ratios of the detection-system correction factors (~ 1.5) to be about 13; this agrees well with the fitted value of 10.76. The value of the energy gap between the two levels, E_{32}, was found to be ~ 830 cm^{-1}. This is a reasonable value if one considers the transition to occur from the relaxed excited state of the $^4S_{3/2}$ level to the $^2H_{11/2}$ level. Previous investigators (24,102) have neglected the difference in the Stoke's shifts of the two levels (which, to a first approximation, are negligible) and calculated E_{32} from absorption data alone.

It was mentioned earlier that the 0.5at.% Er^{3+} sample also contained 0.005at.% Nd^{3+}. The emission spectrum of the Nd^{3+} ions at 300K is shown in Fig. 33. The emission at 11520 cm^{-1} (868 nm) is the $^4F_{3/2} \rightarrow {}^4I_{9/2}$ transition. The very weak emission at 12470 cm^{-1} (802 nm) is believed to be the $^5F_{5/2}$ or $^2H_{9/2} \rightarrow {}^4I_{9/2}$ emission with the excitation being provided due to thermal population from the $^4F_{3/2}$ level. The identification of this emission is based on several observations: the excitation spectrum is that expected for the $^4F_{5/2}, {}^2H_{9/2}$ levels, the lifetime is the

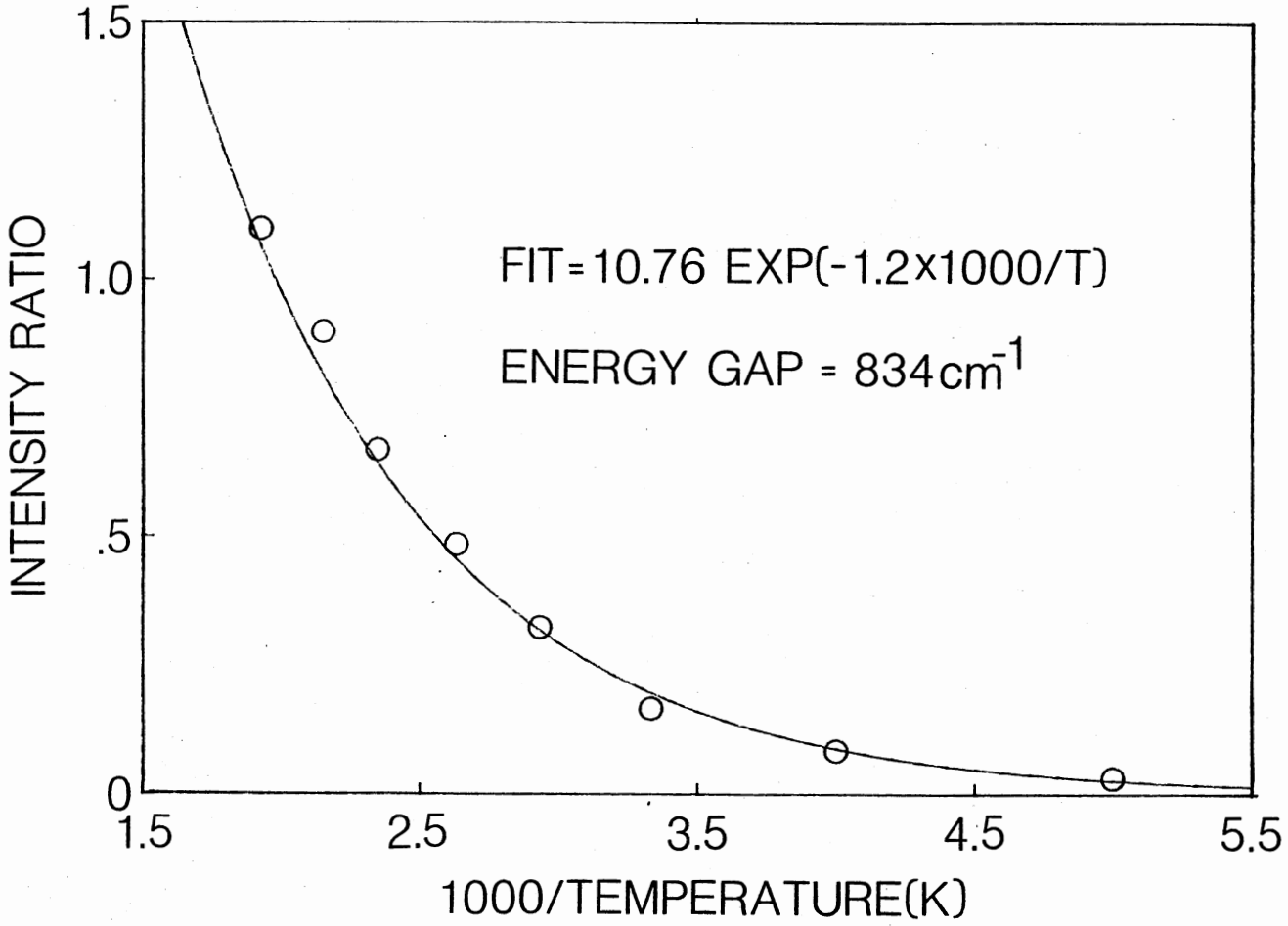

Figure 32. Ratio of the Integrated Intensities of the $^2H_{11/2} \rightarrow {}^4I_{15/2}$ and $^4S_{3/2} \rightarrow {}^4I_{15/2}$ as a Function of 1000/T

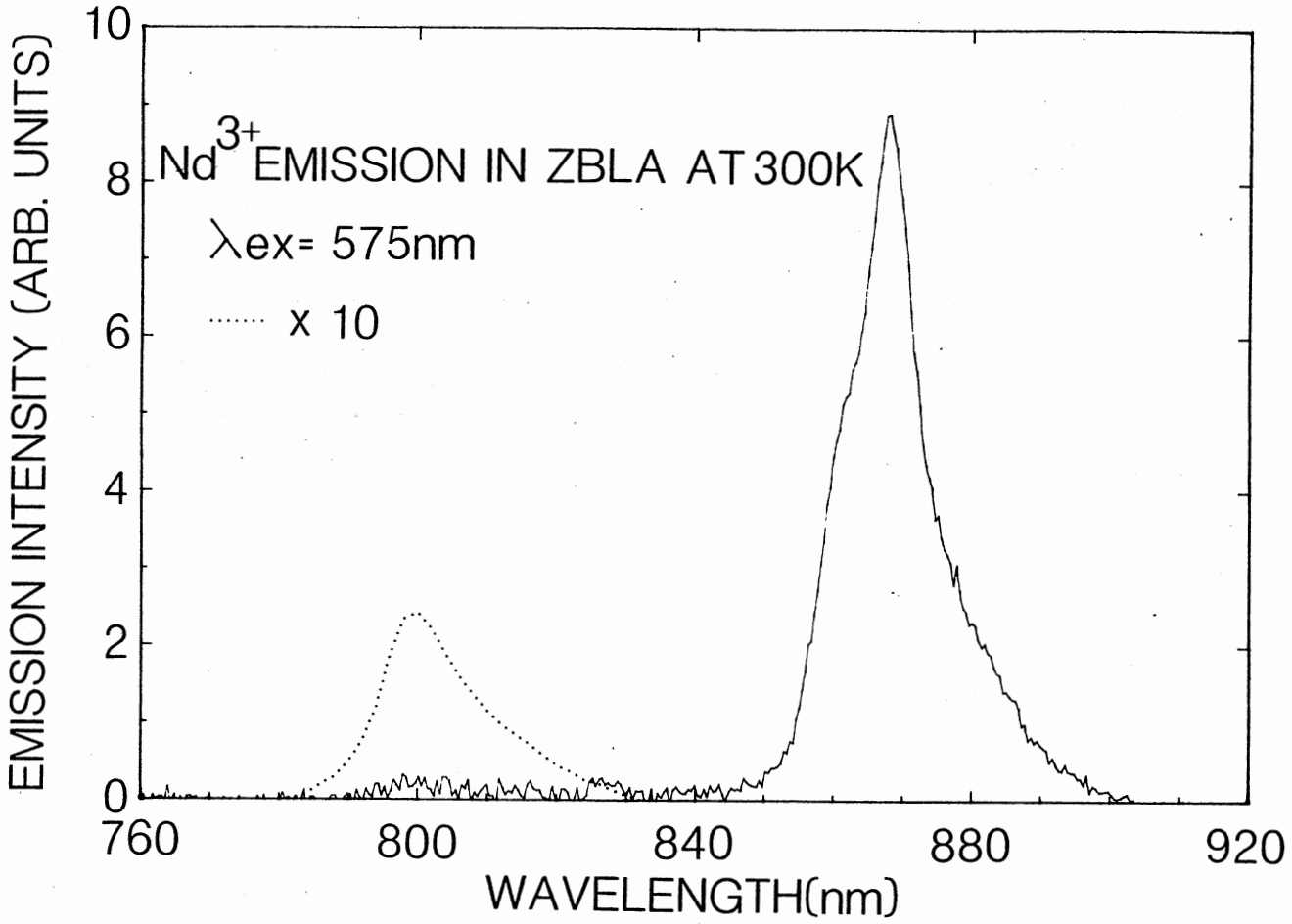

Figure 33. Emission spectrum of Nd^{3+} in ZBLA at 300K

same as the $^4F_{3/2}$ lifetime, and the emission decreases in intensity as the temperature is lowered. The thermalization is extremely weak, as is evidenced by the lack of any effect on the $^4F_{3/2}$ lifetime, which was 444 μs at 15 and 300K. This was the same value found, within experimental error, in ZBL:Nd (22).

Figure 34 shows the Nd^{3+} $^4F_{3/2}$ excitation spectrum (solid line). The $^4F_{3/2}$ emission is in the same spectral range as the Er^{3+} $^4S_{3/2} \rightarrow {}^4I_{13/2}$ emission, which in this sample is about 10 times more intense. Consequently, Er^{3+} excitation bands are present in the Nd^{3+} excitation specrum. To check if these Er^{3+} excitation bands are actually part of the Nd^{3+} excitation spectrum, it is also portrayed in Fig. 34 (dotted line), and is scaled to have the same intensity at the $^4G_{11/2}$ level (378 nm). In Fig. 34 all other Er^{3+} bands have the same peak intensity, except the $^2H_{11/2}$ excitation peak at 521 nm. This discrepancy is due to excitation of Nd^{3+} ions from the $^4G_{7/2}$, $^4G_{9/2}$, and $^2K_{13/2}$ levels, which are at 521 nm in ZBL glass (22). Inspection of Fig. 34 shows that no other bands in the Nd^{3+} excitation spectrum for $\lambda < 550$ nm exist which are not due to Nd^{3+}.

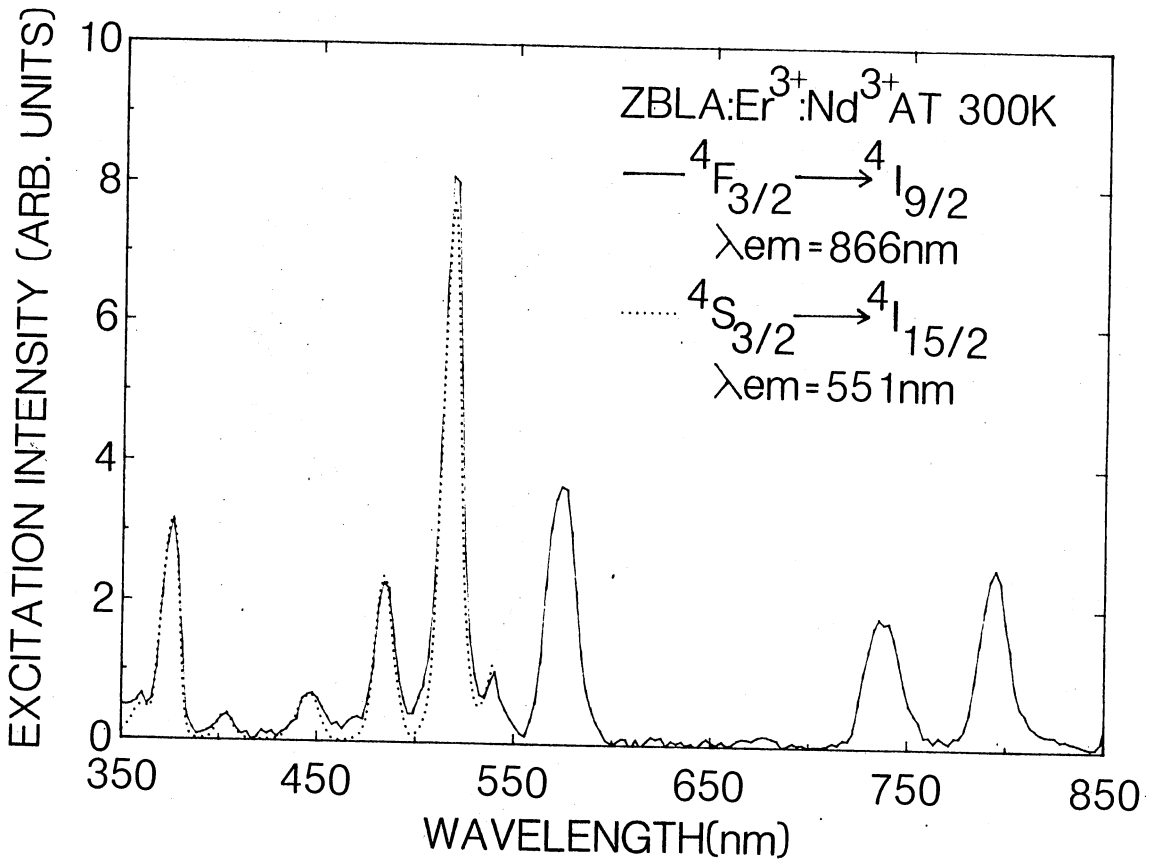

Figure 34. Uncorrected $^4F_{3/2} \rightarrow {}^4I_{9/2}$ Excitation Spectrum of Nd^{3+} (solid line) and the $^4S_{3/2} \rightarrow {}^4I_{13/2}$ Excitation Spectrum of Er^{3+} (dotted line) in ZBLA at 300K

CHAPTER V

DISCUSSION

ZBLA:Er

Previous studies have indicated that nonradiative relaxation of excited states of rare earth ions in solids is through the emission of phonons (54,56,60,65,66,81,89). This assumes that nonradiative effects due to ion-ion cooperation are negligible. In the Theory section it was shown that the rates of multiphonon emission are sensitive to the number of phonons emitted in the transition. Since the energy gaps between levels change negligibly with host for the trivalent lanthanides, the factor influencing the multiphonon emission rate is the energy of the phonons involved in the transition. The phonon density of states can be partially determined from infrared reflectivity and Raman spectroscopy data. Infrared reflectivity measurements of ZBL glass show bands at ~500 and ~270 cm^{-1} (103,104).

The observed multiphonon emission rates for the $^4S_{3/2}$, $^4F_{9/2}$, and $^4I_{11/2}$ levels in the 0.5at.% Er^{3+} sample were calculated from Eq.(24) using the radiative rates predicted by the Judd-Ofelt theory and the measured lifetimes (Table 8 and Figs. 29-31). To apply the Huang-Rhys

theory to these values the phonon energy, the number of phonons required to span the energy gap, and the Huang-Rhys factor S_o are needed. The number of phonons may be calculated readily from Eq.(22). Owing to inhomogeneous broadening, the Huang-Rhys factors and energy gaps are not definitely known experimentally; however, it is possible to establish reasonable limits for these parameters from the absorption and emission spectra. Initial values for these parameters were substituted into Eq.(31) and the values of S_o and $\hbar\omega$ were adjusted to give the best fit to the observed rates. These Huang-Rhys-predicted multiphonon emission rates and the radiative rates were then substituted into Eq.(24) to predict the measured lifetimes.

These predicted lifetimes are shown as solid lines in Figs. 29-31). It should be noted that the radiative rate of the $^4S_{3/2}$ level cannot be assumed to be temperature independent, due to thermalization with the $^2H_{11/2}$ level. The effective radiative-emission probability for the two levels may be calculated from the formula (25)

$$A_{eff} = \frac{12\, A(^2H_{11/2})\exp(-\Delta E/kT) + 4\, A(^4S_{3/2})}{12\exp(-\Delta E/kT) + 4} \qquad (43)$$

using the values of $A(^2H_{11/2})$ and $A(^4S_{3/2})$ given in Table 8 and the value of $\sim E=830\ cm^{-1}$ obtained from the data in Fig. 32. This change in the radiative rate with temperature was taken into account when the observed multiphonon emission rate for the $^4S_{3/2}$ level was calculated. The

Huang-Rhys theory predicts such a low multiphonon emission rate ($<< 10^{-10}$ s^{-1}) at all temperatures for the $^4I_{13/2}$ level that the lifetime should be temperature independent. The line drawn in Fig. 28 is thus the lifetime predicted by the Judd-Ofelt theory. The best fits to the data were found using phonon energies in the range of 460-500 cm^{-1}. This value is consistent with the reflectivity data (103,104). In all cases the calculated energy gaps and the Huang-Rhys theory fairly accurately predicts the temperature dependence of the lifetimes of the $^4I_{11/2}$, $^4F_{9/2}$, and $^4S_{3/2}$ levels. From Fig. 28 it can be seen that, while the Judd-Ofelt theoretical line is always within 10% of the measured values, these values show a slowly decreasing trend with increasing temperature. Several possibilities for explaining this behavior will be presented later.

A semilogarithm graph of the observed low-temperature multiphonon emission rates versus the energy gap to the next lowest level is illustrated in Fig. 35. (Also plotted are the fitted rates and energy gaps.) It can be seen that an exponential dependence of the multiphonon emission rate on the energy gap is obeyed, as shown in the Theory section. A least-squares fit to the observed data to Eq.(27) with $C=1.88\times10^{10}$ s^{-1} and $\alpha=5.77\times10^{-3}$cm is portrayed in Fig. 35. The lower bound for the multiphonon emission rate of the $^2H_{9/2}$ level is also shown.

In the past the multiphonon emission rate has been

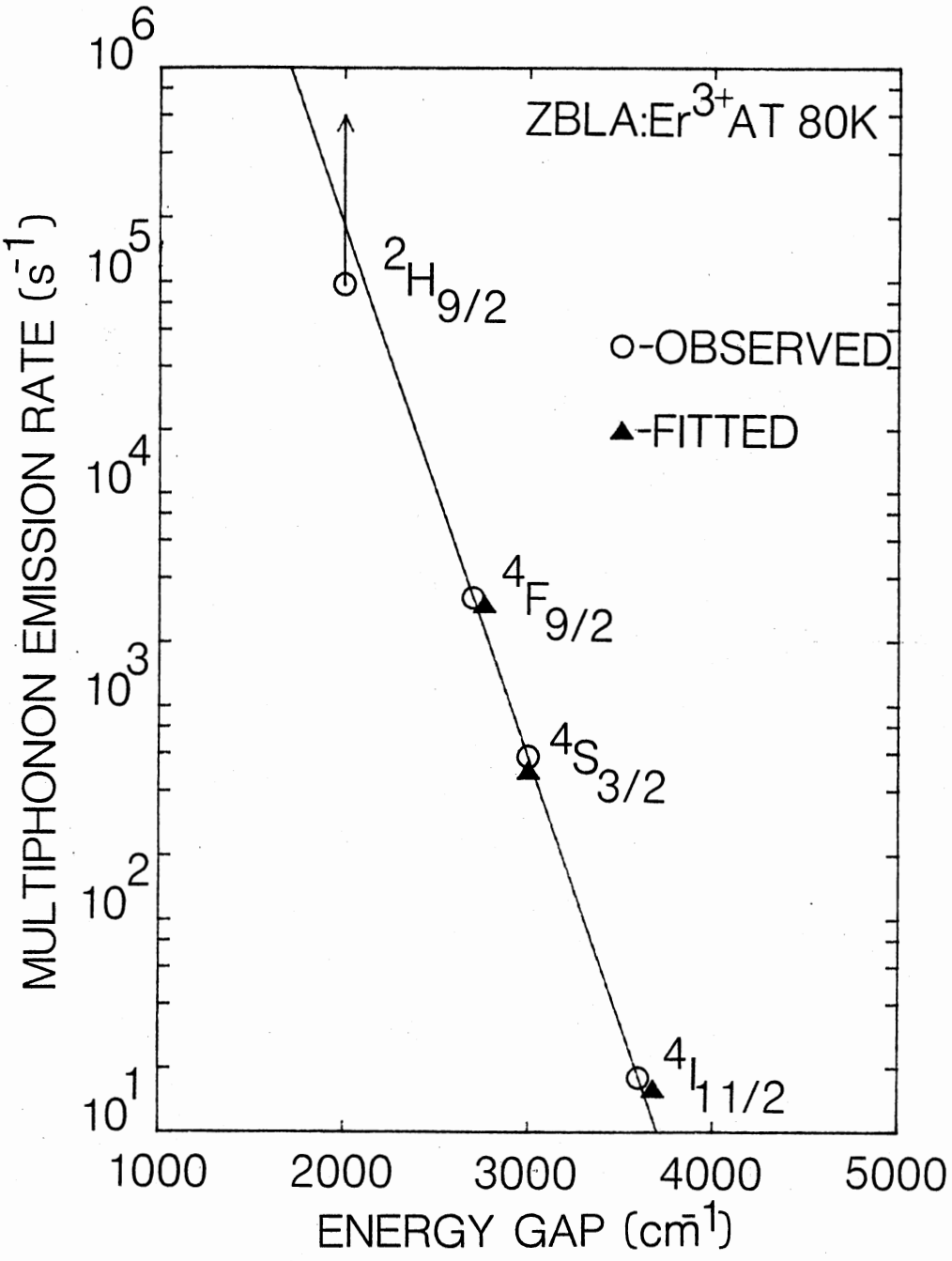

Figure 35. Multiphonon Emission Rates of 0.5at.% Er^{3+} in ZBLA at 80K as a Function of the Energy Gap to the Next-Lowest Level

plotted versus the number of phonons p involved in the transition. Recently Fonger and Struck (70) proposed that the exponential dependence on p be replaced at low temperatures by the equation

$$W_{NR}(0) = N\exp(-S_o)S_o^{p}/p! \qquad (44)$$

which is the first term of Eq.(31) with r=0, valid for $S_o << 1$. They attempted to fit experimental results with Eq.(44) using a fixed value of S_o; however, their predicted dependence of W_{NR} on p, for reasonable values of S_o and N was steeper than exhibited by some ion-host combinations. The data in Fig. 35 show that when S_o is allowed to very slightly, the exponential trend of the data is reproduced.

It should be noted that in using the Huang-Rhys theory to fit the temperature dependences of the $^4S_{3/2}$ and $^4F_{9/2}$ lifetimes, the same number of phonons, six, was used. A Huang-Rhys theoretical fit for the $^4F_{9/2}$ level, using five phonons, is also shown in Fig. 30. The best fit used phonon energies of 445 cm^{-1}, requiring an energy gap smaller than measured. The value of S_o was also smaller than the lower limit inferred from the data. The only major difference in fitting the data in Figs. 29 and 30 was the value of S_o, yet it adequately accounted for the difference in the low-temperature multiphonon emission rates for the two levels. Only recently has the influence

of S_o on W_{NR} been discussed for rare earth ions, while it has long been recognized for transition metal ions (61,70).

It is also possible to use the Kiel model (Eq.(23)) to fit the temperature dependence of the multphonon emission rates. In all cases the Kiel model's values at low temperatures were almost identical to the values predicted by the Huang-Rhys theory, and tended toward higher values for temperatures above ~200K. However, even at the highest temperature (520K) the Kiel model's value is greater by only 6%. It can be shown (105) that for small S_o, the Huang-Rhys equation (Eq.(31)) can be written in the same form as the Kiel model, apart from an additional factor $\exp(-2nS_o)$. For small $S_o(\lesssim 0.1)$, this factor equals ~1 at low temperatures and 0.92 at 600K. While ease of computation and success in predicting the behavior of the multiphonon emission rate make the Kiel model useful, its simplicity is also a liability. The low temperature multiphonon emission rate is found using Eq.(24). There is no way, using this equation alone to know if the value obtained is reasonable. The Huang-Rhys theory provides information to check the plausibility of the values of the multiphonon emission rate, with only slightly more difficulty in performing the calculations.

Thus far all our calculations involving the Huang-Rhys theory have assumed $N=10^{13}$ s^{-1} in Eq.(31). This value is in agreement with earlier values (61,87). Inspection of

Eq.(31) indicates that N can be varied less than an order of magnitude from this value without affecting the value of S_o to such an extent that the fitted values fall outside the experimentally determined limits. Within these limits equally good fits may be obtained, with the S_o values increasing when N is decreased, and vice versa.

Flaherty and DiBartolo have also developed a method for calculating radiative and nonradiative transition rates. This method is based on the temperature dependence of lifetime and intensity measurements, and does not require absolute calibration of the detection system.

If a fluorescent level B is excited entirely through nonradiative transitions from a higher-lying fluorescent level A, the nonradiative rate W_{AB} is given at temperatures T_1 and T_2 by

$$W_{AB}(T_1) = \frac{1}{\tau_A(T_1)} - \frac{1}{\tau_A(T_2)} \left[1 - \frac{\tau_B(T_1)\ I_A(T_1)\ I_B(T_2)}{\tau_B(T_2)\ I_B(T_1)\ I_A(T_2)} \right]^{-1} \qquad (45)$$

$$W_{AB}(T_2) = \frac{1}{\tau_A(T_2)} - \frac{1}{\tau_A(T_1)} \left[1 - \frac{\tau_B(T_2)\ I_A(T_2)\ I_B(T_1)}{\tau_B(T_1)\ I_B(T_2)\ I_A(T_1)} \right]^{-1} \qquad (46)$$

where τ_A and τ_B are the measured lifetimes and I_A and I_B are the measured integrated intensities of levels A and B, respectively. The radiative rate of level A may be found by substituting W_{AB} from Eq.(45) or (46) and the value of τ_A, at the same temperature, in Eq.(24). Since application of this method is relatively straightforward, it was used to calculate the radiative rate of the $^4I_{11/2}$ level. This

level was chosen because the three-level system comprised of the $^4I_{11/2}$, $^4I_{13/2}$, and $^4I_{15/2}$ levels best fits the theoretical system considered by Flaherty and DiBartolo. The 0.5at.% Er^{3+} sample was used for all measurements. The $^4F_{9/2}$ level was used as the excitation level because of its relatively high oscillator strength and the low probability of level bypassing through radiative transitions to the $^4I_{11/2}$ and $^4I_{13/2}$ levels. The change in the integrated intensities of the $^4I_{11/2}$ and $^4I_{13/2}$ levels with temperature is shown in Fig. 36. The low signal-to-noise ratio of the $^4I_{13/2}$ data places large error bars (~10%) on the intensity values shown. The lifetimes of the two levels were taken from the data in Figs. 28 and 29. Substitution of these values into Eqs.(45) and (24) resulted in a mean calculated rate of 92 s^{-1} (10.8 ms) witha standard deviation of 27 s^{-1}. An attempt to fit the temperature dependence of the multiphonon emission rate using this value of the radiative rate required seven 525 cm^{-1} phonons. This phonon energy is too high to provide a good fit to the temperature dependences of the $^4S_{3/2}$ and $^4F_{9/2}$ levels. It should be noted that for two sets of temperatures (300-345 and 300-385K) the calculated multiphonon emission rates were larger than the measured rates and had to be excluded. Closer analysis of the calculated rates showed that they did not lie about the mean but instead were in two groups. The lower-rate group corresponded to anamolous behavior in the $^4I_{13/2}$ intensi-

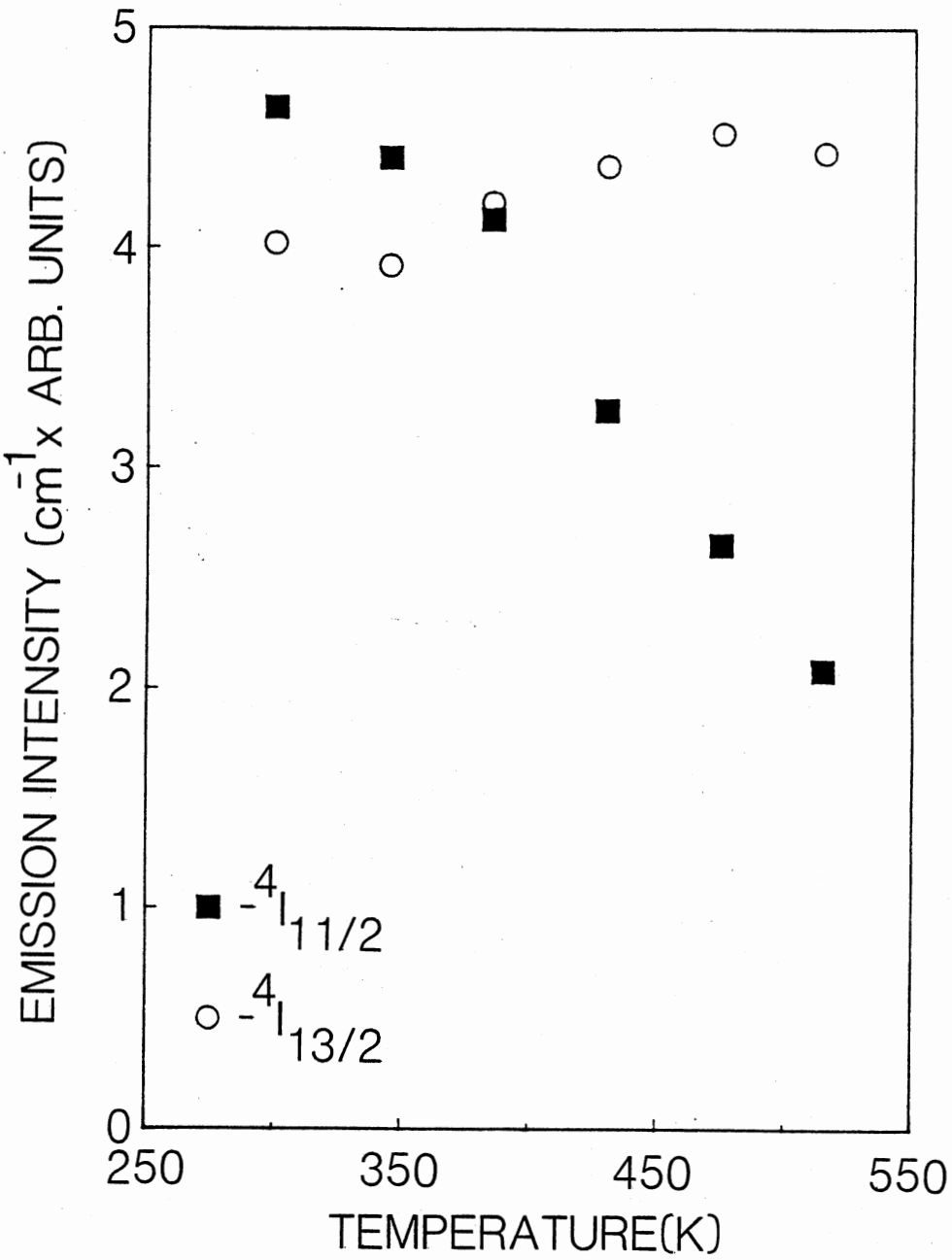

Figure 36. Temperature Dependence of the Integrated Intensities of the $^4I_{11/2} \rightarrow {}^4I_{15/2}$ and $^4I_{13/2} \rightarrow {}^4I_{15/2}$ Emissions

ties, such as the aforementioned results with the 300 and 345K data points. Taking the higher-rate group as more accurate, the calculated radiative rate is 116.5 s^{-1} (8.6 ms) with a standard deviation of 20 s^{-1}, a value quite close to the value of 9.2 ms calculated using the Judd-Ofelt theory. On the basis of these analyses it appears that with accurate intensity and lifetime measrements the Flaherty-DiBartolo method can yield results as accurate as those provided by the Judd-Ofelt theory. However, it is very sensitive to the accuracy of the data used. It can only be applied with confidence to adjacent emitting states. Both conditions limit its applicability.

The Huang-Rhys model and energy-gap law results indicate that the multiphonon emission rate is so low that there should be no temperature dependence for the $^4I_{13/2}$ level. Yet Fig. 28 shows that such a dependence exists. It is well established that with a given J-manifold, differences in oscillator strengths, and hence radiative rates, are different for sublevels within the manifold. It is possible that the temperature dependence of the $^4I_{13/2}$ level in the 0.5at.% Er^{3+} samples is due to thermalization of higher-lying sublevels in the J-manifold with faster radiative rates. The appearance of a band at 6623 cm^{-1} (1510 nm) as the sample is warmed above 15K supports this possibility. This type of thermalization would also explain a trend in the other lifetime data, where the measured lifetimes decrease somewhat faster than the

predicted lifetimes in the temperature range of 100 to 300K.

The preceeding analysis indicates that, for 0.5at.% Er^{3+} in ZBLA glass, current models for determining the radiative and nonradiative rates of rare earth ions in solids work quite well. Compared to Er^{3+} in other fluoride hosts, the oscillator strengths and radiative rates change by no more than an order of magnitude. This is also true for the nonradiative rates (54-56,65,85,102).

The data shown in Figs. 28-31 suggest that Er^{3+} ions in ZBLA glass exhibit energy transfer as the concentration is increased to 2.0 at.%. The lifetimes of the fluorescent levels for both the 0.5 and 2.0 at.% samples are essentially the same at 15K, but the lifetimes of the 2.0 at.% sample decrease markedly in most cases as the temperature increases. Only when the nonradiative rate is dominated by multiphonon emission, as it is for the $^4F_{9/2}$ level, is the effect of energy transfer negligible.

The possibility of energy transfer between Nd^{3+} and Er^{3+} ions in the 0.5 at.% Er^{3+} sample also must be considered since the Er^{3+} $^2H_{11/2}$ level and the Nd^{3+} $^4G_{7/2}$, $^4G_{9/2}$, and $^2K_{13/2}$ levels are in the same spectral range (521 nm). Unfortunately the overlap of the Nd^{3+} $^4F_{3/2}$ $^4I_{9/2}$ emission with the Er^{3+} $^4S_{3/2} \rightarrow {}^4I_{13/2}$ emission, prevents any definite statement for or against energy transfer. Previous work on the effect of Nd^{3+}-Er^{3+} energy transfer on the $^4I_{13/2}$ lifetime indicates that the

inclusion of 0.005 at.% Nd^{3+} should have no effect on this lifetime, i.e., no observable energy transfer (129). Our results suggest that Nd^{3+}-Er^{3+} energy transfer is negligible.

$RbMgF_3$:Er and $RbMgF_3$:Er,Mn

Let us now consider the optical properties of Er^{3+} in $RbMgF_3$. The emission spectra of Er^{3+} in $KMgF_3$ (Figs. 15 and 16) show that Er^{3+} ions are in sites of O_h symmetry. This is achieved only if the Er^{3+} ion substitutes for the Mg^{2+} ion, and the required charge compensation is nonlocal. This is in agreement with the conclusions of Abraham et.al. (88). Note that the Stark splitting of the $^4S_{3/2}$ and $^4I_{15/2}$ J-manifolds of the site 1 Er^{3+} ions are smaller than those for site 2 (Fig. 13). It is reasonable to assume that the less constricted environment of the Mg^{2+} site with the equidistantly spaced F^- ions (site 1 in Fig. 2) will result in a smaller crystal field than the more constricted environment of the other site. On this basis, we assign the Er^{3+} ions responsible for the site 1 and site 2 absorption and emission to the similarly labelled Mg^{2+} sites in Fig. 2.

The value of the $^4S_{3/2}$ lifetime is much shorter than normally observed in fluoride hosts. More importantly, the value of the $^4S_{3/2}$ lifetime, and the emission intensity, both decrease raddidly above 60K and are totally quenched by 150K. Both effects are indicative that some energy

transfer process is occurring. Erbium concentrations in the samples used here are such that if the ions were substituted uniformly throughout the lattice, they would be separated by over 30Å. It is not likely that even energy transfer via the electric dipole-dipole interaction would be so effective over this distance. It is more likely that some aggregation of Er^{3+} ions has occurred. This possibility becomes more reasonable when the observation of Er^{3+}-sensitized Ho^{3+} luminescence (Fig. 5) is considered. The lack of any observable Ho^{3+} absorption, along with an upper bound on the oscillator strengths of the strongest absorptions ($\sim 10^{-5}$) places an upper bound on the concentration of about 100ppm (57,62). Again, efficient energy transfer between Er^{3+} and Ho^{3+} ions over such a distance is not likely. Finally, annealing studies on $RbMgF_3$:Er,Mn support such an aggregation. If $RbMgF_3$:Er,Mn samples are quenched from 700K the emissions from site 2 Er^{3+} ions (Figs. 8-10) disappear and the site 1 emissions become more intense. At the same time the site 1 emission lifetime decreases to 85 μs. Such behavior is hard to explain if the Er^{3+} ions are distributed randomly through the lattice. At the same time, the fast $^4S_{3/2}$ emission decay and low temperature quenching of the emission in $KMgF_3$ are also indicative that similar energy transfer processes are occurring, yet the symmetry is O_h. It may be possible to have aggregates (with regard to the lattice) yet retain locally the original site symmetry.

$RbMgF_3$:Eu,Mn

Although the Eu-impurity was added in trivalent form, it is incorporated into the $RbMgF_3$ lattice as Eu^{2+}. The presence of Eu^{2+} band or line emission depends on parameters such as the type of anion, the charge of the neighboring cations, and the size of the cation the Eu^{2+} ion replaces (106). The presence of Eu^{2+} line emission, shown in Fig. 18, is indicative of a relatively low crystal field at the Eu^{2+} ion site. This is consistent with the Eu^{2+} ion substituting in the relatively open Rb^+ ion sites of the lattice. Zeeman splitting data on $KMgF_3$:Eu, which also has line emissions, indicates that the coordination number of the Eu^{2+} site is twelve, which is the coordination number of the K^+ ion (109). This study also shows that the site symmetry is little changed from the perfect lattice, that is, the charge compensation must be nonlocal. The most likely source of charge compensation is K^+ vacancies. Some Eu^{2+} sites with local compensation were also noted, although their number was much smaller. The results of this investigation are consistent with our observations in $RbMgF_3$:Eu. We conclude that the Eu^{2+} ions are most likely substituting for a Rb^+ ion with charge compensation provided by Rb^+ vacancies. As noted earlier the number of f-f emission lines observed are indicative that many sites exist for the Eu^{2+} ion in this lattice (15). From the lifetime data in Table 5 and the spectra shown in Fig. 19 at least eight sites are present. It was

noted earlier that the $RbMgF_3$ lattice provides two types of Rb^+ sites, one type has C_{3v} symmetry, the other has D_{3h} symmetry. Nonlocal compensation produces one C_{3v} site and one D_{3h} site. Local compensation at one of the six equivalent Rb^+ sites surrounding the C_{3v} Eu^{2+} site gives rise to a third site. The D_{3h} Eu^{2+} site has six Rb^+ neighbors in equivalent positions, and one Rb^+ ion in a nonequivalent position. Local compensation gives rise to two more configurations, for a total of five types of sites. Since there are more sites present, other modifications to the local environment must occur. The increase in the 359.8 nm emission as the Mn^{2+} concentration increases (Fig. 19) suggests that the presence of impurities could be responsible for the other Eu^{2+} sites. Recent time-resolved spectroscopy measurements indicate that energy transfer occurs between the ions responsible for the 360.5 nm and 361.25 nm emissions (107). These ions must be close to one another, causing the shift apparent in the excitation spectra for these ion's emissions.

Evaluations of $RbMgF_3$:Eu (15) and $KMgF_3$:Eu (108) crystals grown at this institution show band emissions unreported in previous investigations (109-111). The only other mention of Eu^{2+} line and band emissions occurring in the same manner as seen for our crystals was by Boulon et.al. (112,113) for KY_3F_{10}:Eu. Their interpretation is that the line emission is due to Eu^{2+} ions substituting for K^+ ions. The broad band emission is due to Eu^{2+} ions

substituting for Y^{3+} ions. While Eu^{2+} could substitute for Mg^{2+} ions in $RbMgF_3$ or $KMgF_3$ without charge compensation it is doubtful that it could do so, since the Mg^{2+} ion is smaller (0.66Å) than the Eu^{2+} ion (1.09Å) (114). The low intensity of the band emissions, which are allowed transitions, implies that their total concentration is low. This suggests that the emissions arise from Eu^{2+} ions at dislocations or near impurities.

The optical properties of the Mn^{2+} ions were different in many respects for the two types of Mn^{2+}-doped samples. In the $Mn_{0.002}$ samples the decay was the sum of two exponentials. This behavior, and the behavior exhibited in Fig. 23, may be explained by assuming that two classes of Mn^{2+} ions are independently excited. The Mn^{2+} ion lower energy levels may be reduced to an equivalent three level system,shown schematically in Fig.23. The population of level 2 during square wave excitation of duration τ is given by the expression (43)

$$N_2(t) = D + E \exp(s_1 t) + F \exp(s_2 t) \quad t \lesssim \tau \tag{47}$$

where D, E, F, s_1, and s_2 represent constants whose values are determined by the pumping rate and the radiative and nonradiative rates of levels 3 and 2 (17,43). For excitation of Eu^{2+} ions and subsequent energy transfer to Mn^{2+} ions it can be shown that this expression reduces to (17)

$$N_2(t) = \frac{wN_o}{p_{21}} [1 - \exp(-p_{21}t)] \tag{48}$$

where N_o is the total number of Mn^{2+} ions of each class, w is the pump rate, defined as the absorption cross section times the incident flux, and p_{21} is the transition rate between level 2 and level 1. The intensity of the emission at frequency ν is related to the number of emitting ions in the following way (43)

$$I(\nu) = N_e p^r h\nu \tag{49}$$

where N_e is the number of emitting ions, p^r is the radiative rate of the transition, and $h\nu$ is the energy of the emitted phonon. Substituting Eq.(48) in Eq.(49), the intensity of the two classes of Mn^{2+} ions immediately following excitation is given by

$$I(\nu) = \frac{wN_o}{p_{21}} [1 - \exp(-p_{21}\tau)]\ p^r h\nu \tag{50}$$

here p_{21} is the measured decay rate of level 2, which may be equal to p^r. The data in Fig. 23 were fitted to the ratio I_s/I_s+I_f, where I is given by Eq.(50) and the subscript s or f denotes the slow- or fast-lifetime class of ions. The data in Fig. 22 may be used to assign values to all parameters in Eq.(50), except the product wN_o, which is of the order $(10^{-4}s^{-1})(10^{19}cm^{-3})=10^{15}s^{-1}cm^{-3}$. The line shown in Fig. 23 is the fit to the data with $h\nu_f=h\nu_s$,

$p_{21s}=p_f{}^r=38.5s^{-1}$, $p_{21s}=11.5s^{-1}$, $p_s{}^r=8.25s^{-1}$, $W_sN_{os}=1.3x10^{15}s^{-1}cm^{-3}$ and $W_fN_{of}=3.8x10^{14}s^{-1}cm^{-3}$. The excellent fit to the data supports the proposed model. It is more difficult to explain why two classes of ions exist; but considering that there are two Mg^{2+} sites in $RbMgF_3$, the oscillator strengths of the Mn^{2+} ions in these sites may be different or changes may occur through exchange interactions with neighboring Eu^{2+} ions, as was reported for Cu^+ and Mn^{2+} ions in $KZnF_3$ (115).

Many studies on sensitized luminescence have used Mn^{2+} ions as activators (116,117). More recently, experiments have been conducted on Eu^{2+}-Mn^{2+} energy transfer (118-122). The presence of the band due to Eu^{2+} ion absorption in the Mn^{2+} excitation specrta (Fig. 21) is confirmation of energy transfer from Eu^{2+} ions. Figure 37 illustrates the excellent overlap between the Eu^{2+} $^6P_{7/2}$ emissions and the Mn^{2+} $^4T_{2g}{}^2$ absorption in $RbMgF_3$. This evidence, and the decrease in the Eu^{2+} lifetimes as the Mn^{2+} concentration is increased (Fig. 20) are indicative that energy transfer occurs from the Eu^{2+} $^6P_{7/2}$ level to the Mn^{2+} ions.

Since sensitized luminescence occurs in $RbMgF_3$:Eu,Mn with the Eu^{2+} ions as sensitizers and the Mn^{2+} ions as activators, it is important to determine the type of energy transfer process (electric dipole-dipole, electric quadrupole-quadrupole, etc.). A prime assumption in energy transfer theories is the random arrangement of sensitizers

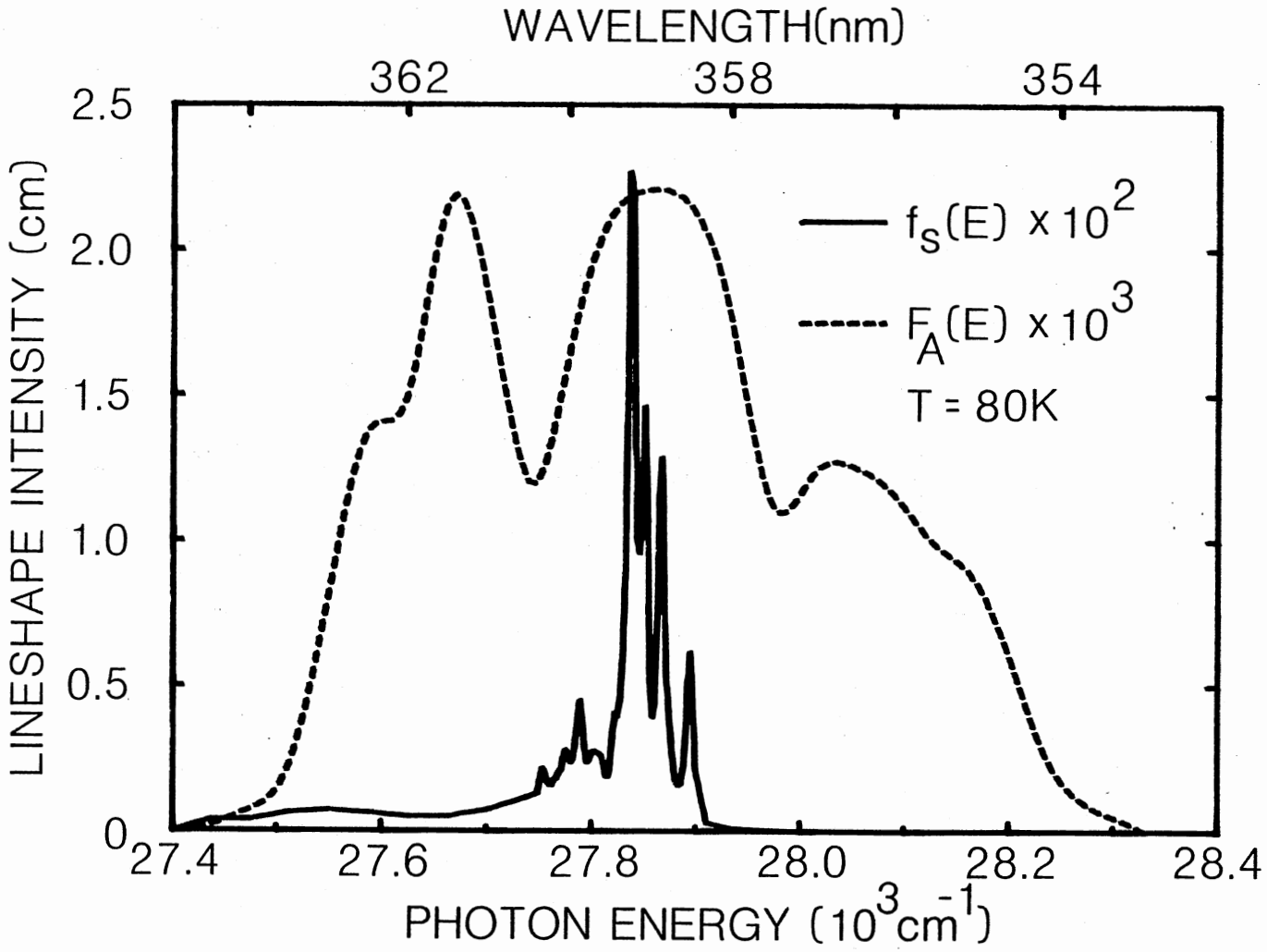

Figure 37. Normalized Lineshape of the Eu^{2+} $^6P_{7/2}$ Emission (solid line) and Mn^{2+} $^4T_{2g}$ ^{2} Absorption (dotted line)

and activators throughout the lattice (75-82). From Fig.38 it is apparent that considerable sensitization of Mn^{2+} ions occurs even at concentrations of 0.2at.%. This rules out the idea that this sensitization could result from random pairing, since this situation constrains the pair concentration to be 100-1000 times less than the total impurity concentration. Also, if the arrangement of Eu^{2+} ions is truly random then the energy transfer would have to occur between ions separated, on the average, by over 20Å. The energy transfer would have to be extremely efficient over this range, since the risetime of the Mn^{2+} luminescence in the $Mn_{0.002}$ samples is faster than 50ns (123). If a preferential pairing or precipitation of the sensitizer and activator occurred, considerable sensitization would result, even at low concentrations of both types of ions. Such an aggregation could occur to reduce the strain in the lattice induced by the presence of the sensitizer or activator alone (116). Previous studies on $RbMgF_3$:Mn (9) and $RbMgF_3$:Er,Mn (14) have shown that Mn^{2+} ions are randomly distributed in the lattice. The same techniques, applied to the Mn^{2+}-doped samples used here also show that the Mn^{2+} ions are randomly distributed. This precludes the possibility of precipitates.

The following model would be consistent with the data: At the low concentrations of Eu^{2+} and Mn^{2+} in the $Mn_{0.002}$ sample, pairing of the two ion types occurs at adjacent Rb^{+} and Mg^{2+} sites. At this distance (~3.5Å), energy

transfer proceeds at a rapid rate which quenches the sensitizer luminescence completely. Unpaired sensitizers are, on the average, at a distance from the activator such that no energy transfer occurs, leaving the lifetime of the sensitizers unchanged. The data in Fig. 22 show that, within experimental error, the Eu^{2+} lifetimes of $RbMgF_3$:Eu and the $Mn_{0.002}$ samples are the same. At higher activator concentrations the number of Eu^{2+}-Mn^{2+} pairs increase. Also, the distance between the unpaired sensitizers and activators is sufficiently reduced for energy transfer to occur. This is the case for the $Mn_{0.03}$ samples which show fast energy transfer (the large initial fluorescence) as well as slower energy transfer (the fluorescence rise) from Eu^{2+} to Mn^{2+} ions after pulsed excitation.

To test this model we consider the simplified case where both the sensitizer and activator have only two levels, the ground and excited states. Actually, for both ion types the absorption is to a different level than emission, but nonradiative processes efficiently transfer all excitation to the lowest excited state. The intensity of an emission at frequency ν is given by Eq.(49). if nonradiative processes can also depopulate the ions emitting state, Eq.(49) must be modified using the expression

$$N_e = N\tau_f p^r \qquad (51)$$

where N is the number of excited ions and τ_f is the fluorescent lifetime (Eq.(24)). From Eq.(49)

$$I_{Mn} = N_{Eu-Mn} p_{Mn}^{r} h\nu_{Mn} \tag{52}$$

$$I_{Eu} = N_{Eu} p_{Eu}^{r} h\nu_{Eu} \tag{53}$$

Since I_{Eu} arises from unpaired Eu^{2+} ions then N in Eq.(51) is replaced by

$$N = N_{Eu} - N_{Eu-Mn} \tag{54}$$

At room temperature, $\tau_f p^r = 0.65$ where p^r is assumed equal to the inverse of the low temperature lifetime (~2ms). When the emission curves in Fig. 18(a) were integrated it was found that $I_{Mn} = 0.3 I_{Eu}$. Using this information and the above relations

$$N_{Eu-Mn} p_{Mn}^{r} h\nu_{Mn} = (0.3)(0.65)(N_{Eu} - N_{Eu-Mn}) p_{Eu}^{r} h\nu_{Eu} \tag{55}$$

The peak intensity energies, $h\nu_{Mn}$ and $h\nu_{Eu}$, are at about 16670 cm^{-1} and 27780 cm^{-1}, respectively. As shown earlier, the Mn^{2+} luminescence decay for the $Mn_{0.002}$ samples is composed of two exponentials. If we assume the faster, temperature independent lifetime class of ions to be more numerous, then the radiative rate p_{Mn}^{r} is essentially the inverse of the lifetime. Substituting the above values of these constants into Eq.(55), and solving

for the ratio N_{Eu-Mn}/N_{Eu} it was found that

$$N_{Eu-Mn}/N_{Eu} = 0.8 \tag{56}$$

This result suggests that 80% of the Eu^{2+} ions are paired with Mn^{2+} ions so the intensity of the Eu^{2+} emissions in the $Mn_{0.002}$ samples should be ~20% of what it is for a $RbMgF_3$:Eu crystal with no Mn^{2+}. If the longer lifetime class of ions is considered to be the dominant class of fluorescent ions then the number of paired ions would be an even greater percentage of the total number of Eu^{2+} ions. The data in Fig. 38 show the intensity of the Eu^{2+} emission in the $Mn_{0.002}$ samples to be 70% of the intensity of $RbMgF_3$:Eu. It is to be admitted that numerous uncertainties exist in measurements of different crystals, nevertheless the data in Fig. 38 suggest a lower limit on the number of Eu^{2+}-Mn^{2+} pairs of 30%. Thus it is reasonable to state that 30-80% of the Eu^{2+} ions in the $Mn_{0.002}$ crystals are paired. Calculation of the number of Eu^{2+}-Mn^{2+} pairs for the $Mn_{0.03}$ sample is complicated by the effect of energy transfer on the Eu^{2+} lifetimes. If the approximation is made that the radiative rates of the Eu^{2+} and Mn^{2+} ions do not change significantly then the ratio $N_{Eu-Mn}/N_{Eu} = 0.95$ is in good agreement with the data in Fig. 38.

Further support for Eu^{2+}-Mn^{2+} pairs in $RbMgF_3$ comes from the application of the Förster-Dexter model to the

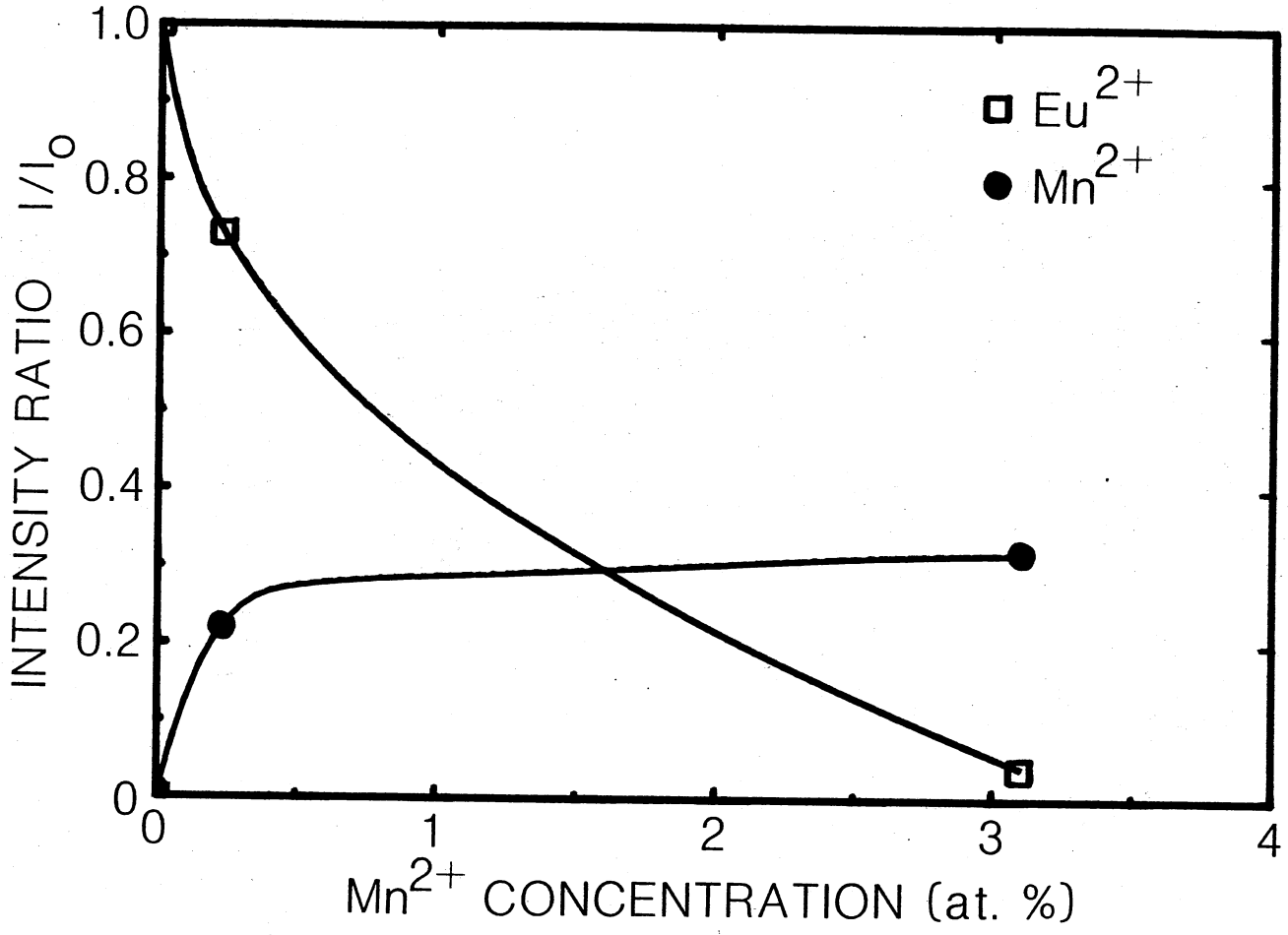

Figure 38. Intensities of the Eu^{2+} and Mn^{2+} Emissions as a Function Of Mn^{2+} Concentration. The Intensities are Normalized to the Intensity I_o of $RbMgF_3$:Eu

experimental data (75-78). The expression for the electric dipole-dipole transfer probability P_{dd} is given by Eq.(32). The emission spectrum of $RbMgF_3$:Eu at 80K, shown in Fig. 37 was used to calculate $f_s(E)$. The absorption spectrum of the $^4T_{2g}{}^2$ level in a $Mn_{0.03}$ sample was used to calculate $F_A(E)$. This should introduce no error since Q_A will be concentration independent at the low activator concentrations used. Since the value of E in the denominator of the integral is almost constant over the range of integration it is usually given the value at the center of the overlap region and taken outside the integral. When these values were determined, it was found that $Q_A=1.05\times10^{-19}(cm^{-1})^{-1}$ and $\int f_s(E)F_A(E)dE=1.87\times10^{-3}(cm^{-1})^{-1}$. For $RbMgF_3$, n=1.48 and E=27855.2 cm^{-1}. Thus Eq.(32) can be written as

$$P_{dd} = \frac{1}{\tau_s}\left(\frac{4.7\text{Å}}{R_{sa}}\right)^6 \qquad (57)$$

when R_{sa} is expressed in angstroms. From Eq.(57) we see that r_o=4.7Å. For distances greater than R_o, the effect of electric dipole-dipole energy transfer is small. The simplest case for estimating the energy transfer rate between sensitizers and activators is when two energy levels are taken to characterize these ions. If the energy transfer rate P_{sa} is time independent then the number of excited activators following pulsed excitation is given by (80)

$$N_a(t)=P_{sa}N_s(0)/(p_A^r-p_s^r-P_{sa})[\exp(-[p_s^r+P_{sa}]t)-\exp(-p_A^r t)] \quad (58)$$

where $N_s(0)$ is the initial population of the sensitizer's excited state immediately after the pulse, and $p_s{}^r$ and $p_A{}^r$ are the radiative rates of the sensitizer and activator, respectively. The time t_{max} at which the activator intensity is a maximum may be found by taking the time derivative of Eq.(58) and setting it to zero

$$t_{max} = \frac{1}{p_A^r - p_s^r - P_{sa}} \ln\left(\frac{p_A^r}{p_s^r + p_A^r}\right) \quad (59)$$

It was stated earlier that for the $Mn_{0.002}$ sample $t_{max}<50ns$. Since the data indicate that $p_s{}^r=500s^{-1}$ and $p_A{}^r=40s^{-1}$ then P_{sa} must be $3x10^8s^{-1}$. Inspection of Eq.(58) indicates that this fast transfer rate cannot be achieved through an electric dipole-dipole interaction.

The long lifetime of the Mn^{2+} ions is indicative of the forbiddenness of the transition. It is reasonable to assume that the energy transfer process may proceed via an electric dipole-quadrupole interaction (78,121). The transfer rate for the electric dipole-quadrupole interaction is related to the transfer rate for the electric dipole-dipole interaction through Eq.(36). The dipole transition has an oscillator strength of about 10^{-7} and the quadrupole transition has an oscillator strength estimated at 10^{-10} (43,121). Since the transition occurs at about 360 nm, substitution of these values into Eq.(36)

yields

$$P_{dq} = \frac{1 \times 10^{-3}}{s} \left(\frac{24.6\text{Å}}{R_{sa}} \right)^{8} \qquad (60)$$

For τ_s=2ms and R_{sa}=3.5Å, $P_{dq}=3\times10^{6}s^{-1}$, which is much closer to the P_{sa} value predicted from the risetime experiments. Better agreement may be obtained assuming the interaction is electric quadrupole-quadrupole or exchange in nature (43,78,80,121). When Eq.(58) is applied to the value of t_{max}=780μs for the $Mn_{0.03}$ samples a value of $6080s^{-1}$ for P_{sa} was obtained. This value, substituted into Eq.(36) yields R_{sa}=7.6Å, in good agreement with the predicted value of 7Å for unpaired sensitizers and activators when a uniform distribution is assumed. Thus, the calculations based on the Förster-Dexter model of energy transfer indicate the observed risetimes of the Mn^{2+} samples can only be explained if a short-range interaction such as electric dipole-quadrupole or exchange is active. This is in agreement with the close pair model.

It should be emphasized that the pairing appears to be preferential and not random. For a random distribution, the statistical number of Eu^{2+}-Mn^{2+} pairs would be given by

$$N_{Eu-Mn} = 6N_{Eu}N_{Mn}/N_{Mg} \qquad (61)$$

since each Rb^{+} site is surrounded by six Mg^{2+} ions. If the

Eu^{2+}-Mn^{2+} pairs were present in a random distribution, then for a constant Eu^{2+} concentration of 2000ppm there would be $3x10^{17}$ pairs/cm^3 in the $Mn_{0.002}$ sample and $4.5x10^{18}$ pairs/cm^3 in the $Mn_{0.03}$ crystal. This would result in a 15-fold increase in Mn^{2+} emission, which is not consistent with the data in Fig. 38.

It was mentioned earlier that the aggregation of impurity ions with the appropriate radii would reduce elastic distortion of the lattice. The Eu^{2+} ion (1.09Å) is smaller than the Rb^{+} ion (1.47Å) it replaces, while the Mn^{2+} ion (0.80Å) is larger than the Mg^{2+} (0.66Å) (114). Earlier investigations have suggested pairing between sensitizers and Mn^{2+} ions in other hosts (120,121,124,125). Investigations on Eu^{2+}-doped alkali halides have shown that Eu^{2+} precipitates form at room temperature (126). Other studies have also shown that the precipitates could be dissolved through thermal annealing (127). When samples of both types of Mn^{2+}-doped crystals were quenched from 800K no changes in the absorption or emission spectrum were noted. This is probably because the hexagonal $RbMgF_3$ structure inhibits mobility of the Eu^{2+}-cation vacancy, which is necessary to form aggregates.

CHAPTER VI

SUMMARY AND PROBLEMS FOR FURTHER STUDY

The optical properties of Er^{3+} in ZBLA glass have been studied. It was found that Er^{3+}, which is readily incorporated into the glass, has optical properties which differ in many respects from rare earth-doped oxide glasses. The emission lifetimes are more single exponential, and the degree of inhomogeneous broadening is less, even under broadband excitation, than for Er^{3+}-doped oxide glasses. This suggests that the site-to-site variation of the Stark field at the Er^{3+} ion site is less in the fluoride glass than in oxide glasses.

Measured oscillator strengths of the transitions between J manifolds at 15 and 300K are compared with calculated electric and magnetic dipole oscillator strengths. The electric dipole oscillator strengths were calculated through the use of the Judd-Ofelt theory. The radiative rates for the five luminescing states were calculated. The nonradiative rates from these excited states were determined by calculating the difference between the measured rates and the calculated rates. The low-temperature nonradiative rates are in agreement with the phenomenological energy-gap law followed by rare earth

ions in a number of crystals and glasses. The temperature dependence of the lifetimes was analyzed using the Huang-Rhys theory of multiphonon emission. Values for the $^4I_{11/2}$ radiative and nonradiative rates obtained by the above methods were compared with those obtained applying the method Flaherty and DiBartolo used to study MnF_2:Er. The multiphonon emission rates in fluorozirconate glass are much lower than the rates for the same levels of Er^{3+} in oxide glasses.

In $RbMgF_3$ crystals, Eu^{2+} and Er^{3+} ions substituting for Rb^+ and Mg^{2+} ions, respectively, require charge compensation. Previous studies on these ions in $KMgF_3$ strongly suggest that this compensation is by Rb^+ vacancies. As a result of this need for compensation, and the zoning effects of the crystal growth process, the amount of dopant which actually is incorporated into the lattice is up to two orders of magnitude less than the premelt impurity concentration.

Energy transfer from Eu^{2+} to Mn^{2+} ions is shown to occur in $RbMgF_3$:Eu,Mn. Emission and excitation spectra indicate that the energy transfer is a resonant process between the Eu^{2+} $^6P_{7/2} \rightarrow {}^8S_{7/2}$ emission and the Mn^{2+} $^6A_{1g} \rightarrow {}^4T_{2g}{}^2$ absorption, with subsequent luminescence from the $^4T_{1g}$ level. Integrated intensity and lifetime measurements as well as energy transfer rates calculated using the Förster-Dexter model suggest that Eu^{2+} ions pair with Mn^{2+} ions. The number of pairs formed is much greater

than that expected for a statistical distribution. This pairing most likely occurs to reduce the strain in the $RbMgF_3$ lattice which results from the introduction of either impurity alone, and occurs as the crystal is grown. As the Mn^{2+} concentration is increased energy transfer between unpaired Eu^{2+} and Mn^{2+} ions occurs as well. No evidence was found for aggregate formation after crystal growth. These observations indicate that impurity ions of the appropriate radii "prefer" to be paired.

The optical properties of Er^{3+}-doped $RbMgF_3$ and $RbMgF_3$:Mn have been investigated. A preliminary study of $KMgF_3$:Er was also made. The $KMgF_3$:Er data indicate that Er^{3+} substitutes for Mg^{2+} in these crystals and the charge compensation is nonlocal, leaving the site symmetry unchanged.

The absorption data for $RbMgF_3$:Er and $RbMgF_3$:Er,Mn indicate that Er^{3+} ions are in two noncubic sites. Based on this information, it appears that these two sites are the two nonequivalent C_{3v} Mg^{2+} sites.

The emission data for the two types of samples differed. In the $RbMgF_3$:Er crystals Er^{3+} in one site fluoresced. In the $RbMgF_3$:Er,Mn samples, Er^{3+} in both sites fluoresced. Lifetimes for the $^4S_{3/2}$ level at 15K are much faster than normally observed. The visible emissions are quenched above 150 K, which is also unusual. This behavior is indicative of energy transfer among the Er^{3+} ions. At this time the reason for this energy

transfer has not been established.

Several areas of further study come out of the work presented here:

1) ZBLA glass, and other fluoride glasses should be tested as laser hosts.
2) If these tests indicate that the fluoride glasses are good laser hosts, the thermal conductivity in the room temperature region should be determined. If it is high enough, fluoride glasses may be good alternatives to the oxide glasses currently used as laser fusion drivers.
3) The ability of ZBLA glass to accept rare earth and transition metal ions makes this material a promising upconversion host. Various "conventional" upconversion ions like Er-Yb should be tried to determine if upconversion is more efficient in this glass than in crystalline materials. Doping these glasses with Yb^{3+} and Mn^{2+}, or other transition metal ions, may result in upconversion.
4) It has been shown that Ni^{2+} and V^{2+} ions in fluoride materials can be made to lase. These ions, like Mn^{2+}, have larger ionic radii than the ionic radius of Mg^{2+}, and they absorb in the 360 nm region. Crystals of $RbMg_{1-x}Ni_xF_3$:Eu and $RbMg_{1-x}V_xF_3$:Eu should be grown to see if the same sensitization is observed.

5) More research on the optical properties of Er^{3+} in $RbMgF_3$ would resolve questions concerning the mechanism responsible for the observed energy transfer. Crystals which contain less than lppm Mn^{2+} should be grown, to eliminate any possible effects its presence might have. The effect of heat treatment on the absorption and emission spectra of these crystals, and $RbMgF_3$:Er,Mn should be further investigated. The application of techniques such as EPR and time-resolved spectroscopy to this material would also be useful.

REFERENCES

1. Emmett, J. L., W. F. Krupke, and J. B. Trenholme, Physics of Laser Fusion, Vol 4. (National Technical Information Service, US Department of Commerce, Springfield, 1982).

2. Remy, H. and W. Seeman, Rec. trav. chem. 59, 516 (1940).

3. Dergunov, E. P. and A. G. Bergman, J. Phys. Chem. (USSR) 22, 625 (1948).

4. Ludekens, W. L. W. and A. J. E. Welsh, Acta. Cryst. 5, 841 (1952).

5. Klasens, H. A., P. Zalm, and F. O. Huysman, Philips Res. Repts. 8, 441 (1953).

6. Shafer, M. W., and T. R. McGuire, J. Phys. Chem Solids 30, 1989 (1969).

7. Holt, E. M., (private communication).

8. Koumvakalis, N., and W. A. Sibley, Phys. Rev. B 13, 4509 (1976).

9. Sibley, W. A., and N. Koumvakalis, Phys. Rev. B 14, 35 (1976).

10. Koumvakalis, N., W. A. Sibley, and G. E. Venikouas, J. Lumin. 15, 283 (1977).

11. Sibley, W. A., and N. Koumvakalis, J. Phys. C 10, 4909 (1977).

12. Podinsh, A., and W. A. Sibley, Phys. Rev. B 18, 5921 (1978).

13. Shinn, M. D., J. C. Windscheif, D. K. Sardar, and W. A. Sibley, Phys. Rev. B 26, 2371 (1982).

14. Sardar, D. K., M. D. Shinn, and W. A. Sibley, Phys. Rev. B 26, 2382 (1982).

15. Alcala', R., D. K. Sardar, and W. A. Sibley, J. Lumin. 27, 273 (1982).

16. Sardar, D. K., W. A. Sibley, and R. Alcala', J. Lumin. 27, 401 (1982).

17. Shinn, M. D., and W. A. Sibley, (to be published by Phys. Rev. B).

18. Poulain, M., Second International Symposium on Halide Glasses (1983).

19. Poulain, M., M. Poulain, J. Lucas, and P. Brun, Mater. Res. Bull. 10, 243 (1975).

20. Poulain, M., M. Chanthanasinh, and J. Lucas. Mater. Res. Bull. 12, 151 (1977).

21. Drexhage, M. G., C. T. Moynihan, M. Saleh Boulos, and K. P. Quinlan, Proceedings of the Physics of Fiber Optics, B. Bendow and S. S. Mitra (Eds.), (American Ceramic Society, Columbus, Ohio, 1981).

22. Lucas, J., M. Chanthanasinh, M. Poulain, M. Poulain, P. Brun, and M. J. Weber, J. Non-Cryst. Solids 27, 273 (1978).

23. Reisfeld, R., E. Greenberg, R. N. Brown, M. G. Drexhage and C. K. Jorgensen, Chem Phys. Lett. 95, 91 (1983).

24. Reisfeld, R., G. Katz, N. Spector, C. K. Jorgensen, C. Jacoboni, and R. De Pape, J. Solid State Chem. 41, 253 (1982).

25. Shinn, M. D., W. A. Sibley, M. G. Drexhage, and R. N. Brown, Phys. Rev. B 27, 6635 (1983).

26. Slater, J. C., Phys. Rev. 34, 1293 (1929).

27. Condon, E. U. and G. H. Shortley, The Theory of Atomic Spectra, 2nd ed., (Cambridge university Press, New York, 1953).

28. Slater, J. C., Quantum Theory of Atomic Spectra, Vols. 1,2 (McGraw-Hill, New York, 1960).

29. Bethe, H. A., Ann. Physik 3, 133 (1929).

30. Van Vleck, J. H., The Theory of Electric and Magnetic Susceptibilities, (Oxford, 1932).

31. Finklestein, R. and J. H. Van Vleck, J. Chem. Phys. 8, 790 (1940).

32. Penney, W. G. and R. Schlapp, Phys. Rev. 41, 194 (1932).

33. Schlapp, R. and W. G. Penney, Phys. Rev. 42, 666 (1932).

34. Ferguson, J., Progress in Inorganic Chemistry, Vol. 12 p. 159,J. J. Lippard (Ed.), (Interscience, New York, 1970).

35. Dieke, G. H., Spectra and Energy Levels of Rare Earths in Crystals, (Interscience, New York, 1968).

36. Imbush, G. F. and R. Kopelman, Laser Spectroscopy of Solids, Vol. , W. M. Yen and P. M. Selzer (Eds.), (Springer, New York, 1981).

37. Watson, R. E., Technical Report No. 12, June 15, 1959 Solid State and Molecular Theory Group, (MIT, Cambridge).

38. Watson, R. E., Phys. Rev. 118, 1036 (1960).

39. Watson, R. E., Phys. Rev. 119, 1934 (1960).

40. Christensen H. P., Phys. Rev. B 19, 6564 (1979).

41. Koumvakalis N., Ph.D. Dissertation, (Oklahoma State University, 1976).

42. Tanabe, Y. and S. Sugano, J. Phys. Soc. Jpn. 9, 753,766 (1954).

43. DiBartolo, B., Optical Interactions in Solids, (Wiley, New York, 1968).

44. Schiff, L. I., Quantum Mechanics, 3rd ed. (McGraw-Hill, New York, 1968).

45. Cotton, F. A., Chemical Applications of Group Theory, (Interscience, New York, 1971).

46. Van Vleck, J. H., J. Chem. Phys. 41, 67 (1937).

47. Judd, B. R., Phys. Rev. 127, 750 (1962).

48. Ofelt, G. S., J. Chem. Phys. 37, 511 (1962).

49. Racah, G., Phys. Rev. 61, 186 (1942).

50. Racah, G., Phys. Rev. 62, 438 (1942).

51. Racah, G., Phys. Rev. 63, 367 (1942).

52. Racah, G., Phys. Rev. 76, 1352 (1952).

53. Nielson, C. W. and G. F. Koster, Spectroscopic Coefficients for the p^n, d^n, and f^n Configurations, (The MIT Press, Cambridge, 1964).

54. Riseberg, L. A. and M. J. Weber, Progress in Optics, Vol. 14, p. 89, E. Wolf (Ed.), (Elsevier, New York, 1976).

55. Krupke, W. F., Phys. Rev. 145, 325 (1966).

56. Weber, M. J., Phys. Rev. 157, 262 (1967).

57. Weber, M. J., B. H. Matsinger, V. L. Donlan, and G. T. Surratt, J. Chem. Phys. 57, 562 (1972).

58. Weber, M. J., T. E. Varitimos, and B. H. Matsinger, Phys. Rev. B 8, 47 (1973).

59. Krupke, W. F., IEEE J. Quantum Electron. 10, 450 (1974).

60. Weber, M. J., Phys. Rev. B 8, 54 (1973).

61. Struck, C. W. and W. H. Fonger, Phys. Rev. B 4, 22 (1971).

62. Tanimura, K., M. D. Shinn, W. A. Sibley, M. G. Drexhage, and R. N. Brown, (submitted to Phys. Rev. B).

63. Kiel, A., Quantum Electronics, Vol. 1, p. 765, P. Grivet and N. Bloembergen (Eds.), (Columbia University Press, New York, 1964).

64. German, K. R. and A. Kiel, Phys. Rev. B 8, 1846 (1973).

65. Riseberg, L. A. and H. W. Moos, Phys. Rev. 174, 429 (1968).

66. Layne, C. B., W. H. Lowdermilk, and M. J. Weber, Phys. Rev. B 16, 10 (1977).

67. Huang, K. and A. Rhys, Proc. R. Soc. London, Ser. A 204, 406 (1950).

68. Lax, M., J. Chem. Phys. 20, 1752 (1952).

69. Klick, C. C. and J. H. Schulman, J. Opt. Soc. Am. 42, 910 (1952).

70. Fonger, W. H. and C. W. Struck, J. Lumin. 17, 241 (1978).

71. Iverson, M. V., J. C. Windscheif, and W. A. Sibley, Appl. Phys. Lett. 36, 183 (1980).

72. Feuerhelm, L. N. and W. A. Sibley, J. Phys. C 16, 799 (1983).

73. Keil, T. H., Phys. Rev. A140, 601 (1965).

74. Sturge, M., Phys. Rev. B 8, 6 (1973).

75. Forster, T., Ann. Physik 2, 55 (1948).

76. Forster, T., Z. Naturforsch. 4a, 321 (1949).

77. Forster, T., Discuss Faraday Soc. 27, 7 (1959).

78. Dexter, D. L., J. Chem. Phys. 21, 836 (1953).

79. Reisfeld, R., Structure and Bonding, Vol. 30, p.65 (Springer, Berlin, 1975).

80. Powell, R. C. and G. Blasse, Structure and Bonding, Vol. 42, p. 43 (Springer, Berlin, 1980).

81. Wright, J. C., Topics in Applied Physics Vol. 15 p. 239 F. K. Fong (Ed.), (Springer, Berlin, 1976).

82. Inokuti, M. and F. Hirayama, J. Chem. Phys. 43, 1978 (1965).

83. Moore, D. S. and J. C. Wright, J. Chem. Phys. 74, 1626 (1981).

84. Hirano, M. and S. Shionoya, J. Phys. Soc. Jpn. 28, 926 (1970).

85. Renfro, G. M., J. C. Windscheif, W. A. Sibley, and R. F. Belt, J. Lumin. 22, 51 (1980).

86. Ensign, J. C. and N. E. Byer, Phys. Rev. B 6, 3227 (1972).

87. Iverson, M. V. and W. A. Sibley, Phys. Rev. B 21, 2522 (1980).

88. Abraham, M. M., C. B. Finch, J. L. Kolopus, and J. T. Lewis, Phys. Rev. B 3, 2855 (1971).

89. Flaherty, J. M. and B. DiBartolo, J. Lumin. 8, 51 (1973).

90. Wilson, B. A., W. M. Yen, J. Hagerty, and G. F. Imbush, Phys. Rev. B 19, 4238 (1979).

91. Hernandez, J., W. K. Cory, and J. Rubio, Jpn. J. Appl. Phys. 18, 533 (1979).

92. Freiser, M. J., S. Methfessel, and F. Holtzberg, J. Appl. Phys. 39, 900 (1968).

93. Sibley, W. A., S. I. Yun, and W. E. Vehse, J. Phys. C 6, 1105 (1973).

94. Hush, N. S. and R. J. M. Hobbs, Progress in Inorganic Chemistry Vol. 10, p. 259 F. A. Cotton (Ed.), (Interscience, New York, 1968).

95. Sibley, W. A. and D. Pooley, Treatise on Material Science and Technology, Vol. 5, p. 45, H. Herman (Ed.), (Academic Press, New York, 1968).

96. Sibley, W. A., Semiconductors and Insulators 5, 281 (1983).

97. Hewes, R. A. and M. V. Hoffman, J. Lumin. 3, 261 (1971).

98. Al'tshuler, N. S., L. D. Livanov, and A. L. Stolov, Opt. Spect. 36, 72 (1974).

99. Bodrug, S. N., E. C. Valyashko, V. N. Mednikova, D. T. Sviridov, and R. K. Sviridov, Opt. Spect. 34, 176 (1973).

100. Munoz, E., J. L. Boldu', and G. Aquilar, J. Chem. Phys. 63, 4222 (1975).

101. Prather, J. L., Atomic Energy Levels in Crystals, NBS Monograph 19, (U.S. Dept. of Commerce, 1961).

102. Reisfeld, R. and Y. Eckstein, J. Non-Cryst. Solids 15, 125 (1974).

103. Bendow, B., P. K. Banarjee, M. G. Drexhage, J. Goltmann, S. S. Mitra, and C. T. Moynihan, Comm Amer. Ceram. Soc. 65, C8 (1982).

104. Almeida, R. M. and J. D. Mackenzie, J. Chem. Phys. 74, 5954 (1981).

105. Tanimura, K., (private communication).

106. Blasse, G., Phys. Stat. Sol.(b) 55, K131 (1973).

107. Venikouas, G. E., A. M. Ghazzawi, and R. C. Powell, Bull. Amer. Phys. Soc. 28, 536 (1983).

108. Sardar, D. K., (private communication).

109. Al'tshuler, N. S., E.'Kh. Ivoilova, and A. L. Stolov, Sov. Phys. Solid State 15, 1602 (1974).

110. Sommerdijk, J. L. and A. Bril, J. Lumin. 11, 363 (1976).

111. Sommerdijk, J. L., A. Bril, and F. M. J. H. Hoex-strik, J. Lumin. 15, 115 (1977).

112. Boulon, G., J. C. Gacon, D. Trotter, and A. Vedrine, Phys. Stat. Sol.(b) 93, 775 (1979).

113. Joubert, M. F., G. Boulon, and F. Gaume, Chem. Phys. Lett. 80, 367 (1981).

114. Handbook of Chemistry and Physics, 63rd. ed. p. F-179, R. C. Weast (Ed.), (CRC Press, Bacon Raton, Florida, 1982).

115. Ferguson, J., H. J. Guggenheim, and E. R. Kraus, J. Phys. C 4, 1866 (1971).

116. Botden, Th. P. J., Philips Res. Rep. 7, 197 (1952).

117. Klick, C. C. and J. H. Schulman, Solid State Physics, Vol. 5, p. 119 F. Seitz and D. Turnball (Eds.), (Academic Press, New York, 1951).

118. Barry, T. L., J. Electrochem. Soc. 115, 733 (1968).

119. Barry, T. L., J. Electrochem. Soc. 117, 381 (1970).

120. Tamatani, M., Jpn. J. Appl. Phys. 13, 950 (1974).

121. Stevels, A. L. N. and J. M. P. J. Verstegen, Philips Res. Rep. 37, 221 (1977).

122. Sommerdijk, J. L. and A. L. N. Stevels, Philips Res. Rep. 37, 221 (1977).

123. Venikouas, G. E., (private communication).

124. Leach, R., J. Electrochem. Soc. 105, 27 (1958).

125. Danielson, B. L., Phys. Rev. 142, 228 (1966).

126. Lopez, F. J., H. Murrieta, J. Hernandez, and J. Rubio, Phys. Rev. B 22, 6428 (1980).

127. Jaque, F., C. Zaldo, F. Cusso', and F. Agullo'-Lopez, Solid State Comm. 43, 123 (1982).

VITA

Michael David Shinn

Candidate for the Degree of

Doctor of Philosophy

Thesis: OPTICAL PROPERTIES OF IMPURITY IONS IN FLUORIDE MATERIALS

Major Field: Physics

Biographical:

Personal Data: Born in Stillwater, Oklahoma, September 6, 1956, the son of Oliver F. and Marilyn J. Shinn.

Education: Graduated from College High School, Bartlesville, Oklahoma, in May, 1974. Attended Oklahoma State University, majoring in Physics, and received the Bachelor of Science degree, July, 1978. Received Master of Science degree in Physics at Oklahoma State University in July, 1980. Completed requirements for Doctor of Philosophy in Physics in December, 1983.

Professional Experience: Graduate Research Assistant from May, 1978 to present. Worked as Assistant to the Radiation Safety Officer from May, 1978 to August, 1983. Member of Sigma Xi and the American Physical Society.